The composition and redox state of bridgmanite in the lower mantle as a function of oxygen fugacity

Rong Huang[a,*], Tiziana Boffa Ballaran[a], Catherine McCammon[a], Nobuyoshi Miyajima[a], David Dolejš[b], Daniel J. Frost[a]

[a] Bayerisches Geoinstitut, Universität Bayreuth, D-95440 Bayreuth, Germany

[b] Institut für Geo- und Umweltnaturwissenschaften, Universität Freiburg, D-79104 Freiburg i.Br., Germany

* corresponding author (Rong.Huang@uni-bayreuth.de)

Tel: (+49) 921 55 3735; Fax: (+49) 921 55 3769

(Submitted for publication in Geochimica et Cosmochimica Acta 2021)

Abstract

The chemistry of bridgmanite (Brg), especially the oxidation state of iron, is important for understanding the physical and chemical properties, as well as putting constraints on the redox state, of the Earth's lower mantle. To investigate the controls on the chemistry of Brg, the Fe^{3+} content of Brg was investigated experimentally as a function of composition and oxygen fugacity (fO_2) at 25 GPa. The $Fe^{3+}/\Sigma Fe$ ratio of Brg increases with Brg Al content and fO_2 and decreases with increasing total Fe content and with temperature. The dependence of the $Fe^{3+}/\Sigma Fe$ ratio on fO_2 becomes less steep with increasing Al content. Thermodynamic models were calibrated to describe Brg and ferropericlase (Fp) compositions as well as the inter-site partitioning of trivalent cations in Brg in the Al-Mg-Si-O, Fe-Mg-Si-O and Fe-Al-Mg-Si-O systems. These models are based on equilibria involving Brg components where the equilibrium thermodynamic properties are the main adjustable parameters that are fit to the experimental data. The models reproduce the experimental data over wide ranges of fO_2 with a relatively small number of adjustable terms. Mineral compositions for plausible mantle bulk compositions can be calculated from the models as a function of fO_2 and can be extrapolated to higher pressures using data on the partial molar volumes of the Brg components. The results show that the exchange of Mg and total Fe (i.e., ferric and ferrous) between Brg and Fp is strongly fO_2 dependent, which allows the results of previous studies to be reinterpreted. For a pyrolite bulk composition with an upper mantle bulk oxygen content, the fO_2 at the top of the lower mantle is -0.86 log units below the iron-wüstite buffer (IW) with a Brg $Fe^{3+}/\Sigma Fe$ ratio of 0.5 and a bulk rock ratio of 0.28. This requires the formation of 0.7 wt. % Fe-Ni alloy to balance the raised Brg ferric iron content. With increasing pressure, the model predicts a gradual increase in the $Fe^{3+}/\Sigma Fe$ ratio in Brg in contrast to several previous studies, which levels off by 50 GPa. Oxygen vacancies in Brg decrease to practically zero by 40 GPa, likely influencing elasticity, diffusivity and viscosity in the top portion of the lower mantle. The models are also used to explore the fO_2 recorded by inclusions in diamonds, which likely crystallized as Brg in the lower mantle, revealing oxygen fugacities which likely preclude the formation of some diamonds directly from carbonates, at least at the top of the lower mantle.

Key words: bridgmanite; Fe content; ferric iron; oxygen fugacity; lower mantle

1. Introduction

The ability to determine the chemical compositions of lower mantle minerals is important not only for understanding transport properties (Holzapfel et al., 2005; Keppler et al., 2008; Manthilake et al., 2011; Okuda et al., 2019; Xu et al., 1998) but also for placing constraints on the redox state and the speciation of volatile elements in the lower mantle and exploring the origin of mineral inclusions in diamonds proposed to originate there (Kaminsky et al., 2015; McCammon et al., 1997, 2004c; Walter et al., 2011). Furthermore, in order to interpret seismic observations of the lower mantle to potentially obtain constraints on its composition and temperature, we need to understand how this composition may be distributed between mineral phases as a function of depth (Bina and Helffrich, 2014; Mao, 1997; Mattern et al., 2005). The Earth's lower mantle likely consists dominantly of bridgmanite (Brg) with lesser amounts of ferropericlase (Fp) and $CaSiO_3$ perovskite but the compositions of Brg and Fp can change as a function of depth due to interphase Fe^{2+}-Mg partitioning (Auzende et al., 2008; Irifune et al., 2010; Kobayashi et al., 2005; Lin et al., 2013; Sakai et al., 2009; Sinmyo and Hirose, 2013; Sinmyo et al., 2008) and changes in mineral $Fe^{3+}/\Sigma Fe$ ratios (Andrault et al., 2018; Piet et al., 2016; Prescher et al., 2014; Shim et al., 2017). In addition, the specific mechanism through which trivalent cations such as Fe^{3+} and Al are accommodated in the Brg structure, may also have implications for mineral, and therefore lower mantle, properties.

There are two cation sites in Brg: the larger A site occupied by Mg and the smaller octahedral B site occupied by Si. While ferrous iron, Fe^{2+} substitutes for Mg on the A site, trivalent cations M^{3+} (M^{3+} = Fe^{3+} or Al^{3+}) can enter both sites through at least two mechanisms (Andrault et al., 1998; Lauterbach et al., 2000; McCammon et al., 1992). A charge-coupled substitution (CC) can occur, that forms compositions along the $MgSiO_3$-M_2O_3 join and is described, using Kröger–Vink notation (Kröger and Vink, 1956), by

$$\mathrm{Mg}_{\mathrm{Mg}}^{\mathrm{X}} + \mathrm{Si}_{\mathrm{Si}}^{\mathrm{X}} \rightarrow \mathrm{M}_{\mathrm{Mg}}^{\cdot} + \mathrm{M}_{\mathrm{Si}}^{\prime} \quad (1)$$

and also an oxygen vacancy (OV) forming mechanism, that results in compositions along the $MgSiO_3$-$MgMO_{2.5}$ join, i.e.,

$$2\mathrm{Si}_{\mathrm{Si}}^{\mathrm{X}} \rightarrow 2\mathrm{M}_{\mathrm{Si}}^{\prime} + \mathrm{V}_{\mathrm{O}}^{\cdot\cdot} \quad (2)$$

The latter mechanism will also depend on the nature of coexisting phases that buffer the silica activity, such as Fp. The oxidation state of Fe in Brg, in addition to its site occupancy along with Al, will have strong effects on properties such as elasticity (Andrault et al., 2001, 2007; Glazyrin et al., 2014; Mao et al., 2017;

Saikia et al., 2009; Walter et al., 2004), rheology (Holzapfel et al., 2005), and electrical (Xu et al., 1998) and thermal conductivity (Goncharov et al., 2009, 2010) as well determining whether iron spin transitions occur in Brg under lower mantle conditions (Catalli et al., 2010, 2011; Hsu et al., 2011; Lin et al., 2012, 2016) and whether charge disproportionation of Fe^{2+} may lead to the formation of iron-rich alloy in the lower mantle (Frost et al., 2004). Understanding the controls on the chemistry of Brg is, therefore, an important first step in ultimately modelling the mineral physics, redox state and seismic properties of the lower mantle.

In spite of its importance the $Fe^{3+}/\Sigma Fe$ ratio in Brg at lower mantle conditions is poorly understood. The Brg $Fe^{3+}/\Sigma Fe$ ratio and Fe-Mg partitioning between Brg and Fp as a function of pressure obtained in different diamond anvil cell (DAC) studies are generally in poor agreement (Piet et al., 2016; Prescher et al., 2014; Shim et al., 2017; Sinmyo et al., 2011). Even in multi-anvil studies at uppermost lower mantle conditions, reported Brg $Fe^{3+}/\Sigma Fe$ ratios vary significantly (Frost and Langenhorst, 2002; Frost et al., 2004; Irifune et al., 2010; Lauterbach et al., 2000; McCammon, 1997; McCammon et al., 2004b; Stagno et al., 2011) and while it is qualitatively apparent that these variations are dependent on Brg Al content (Frost et al., 2004; McCammon et al., 2004b), and to some extent on oxygen fugacity (fo_2) (McCammon et al., 2004b; Nakajima et al., 2012), there is currently no framework through which to understand or predict these variations. This makes it also very hard to understand the differences observed between higher pressure DAC studies where further complications potentially arise from the occurrence of iron spin cross over transitions involving Fe^{2+} and Fe^{3+} (see Lin et al., 2013 for a review). Experiments on Brg at deep lower mantle conditions are extremely challenging and involve inherently large uncertainties in temperature and composition. It is, therefore, essential to have a thermodynamic model based on a rigorous set of experiments performed at well constrained experimental conditions that can be used to assess and interpolate between high-pressure data sets.

By varying the fo_2 over wide ranges, tight constraints can be placed on the thermodynamic properties of Fe^{3+}-bearing Brg components. In this study, this has been achieved using a variety of different oxygen buffering assemblages and the effects of varying Al and bulk Fe contents have also been examined. By first deriving thermodynamic equations based on equilibria involving Brg components in simple Fe-free and Al-free systems it was possible to derive a thermodynamic model to describe the composition and site speciation in Fe and Al-bearing Brg as a function of composition and fo_2 at 25 GPa and 1973 K. Based on this model, the compositions of phases at the top of the lower mantle and the amount of metal formed

through Fe^{2+} charge disproportionation can be calculated for various bulk compositions. Moreover, using the volumes and equations of state of different Brg components from previous studies, an understanding of how the composition of Brg may change at higher pressures in the lower mantle can be obtained. This can then be used to evaluate the results of DAC studies performed at higher pressure conditions.

2. Experiments

Five pyroxene compositions (A)-(E) with different Fe and Al contents as shown in Table 1 were prepared from dried oxide mixtures of reagent grade MgO, SiO_2, Al_2O_3 and Fe_2O_3. To ensure chemical homogeneity, the oxides were first made into glass by grinding the weighed oxide powders together under ethanol, then, after drying, fusing them at 1650 °C followed by rapidly quenching into cold water. The obtained glass (Table 1) was then powdered and cold pressed into pellets and fired in a CO_2-CO gas-mixing furnace at 1250 ˚C at an oxygen fugacity of 2 log units below the fayalite-magnetite-quartz (FMQ) buffer for 48 hours. To make sure that the Fe^{3+} of the whole sample was reduced homogeneously, the rapidly quenched pellets were re-ground and re-fired at identical conditions. The recovered samples consisted of pyroxene containing only Fe^{2+}, as confirmed by means of Mössbauer spectroscopy. Glass (E) was not reduced and thus contains only a minor amount of Fe^{2+} as a result of the glass making process in air. Each of these pyroxenes (A-D) and glass (E) were then mixed with different oxygen buffering assemblages. Depending on the redox conditions needed, either Fe metal, ReO_2, Fe_2O_3, Ru-RuO_2, or PtO_2 were added (Table 2). In some experiments, buffers were not used and iridium metal (5 wt. %) was added to act as a sliding redox sensor, which alloys with Fe drawn from Brg and Fp during the experiments. The Fe content of the Ir-Fe alloy depends on the fo_2 at the experimental conditions, from which the fo_2 can be determined using chemical analyses performed after the experiment is recovered. In addition, reduced $(Mg_{0.9}Fe_{0.1})O$ Fp was added to all experiments to ensure an MgO-saturated bulk composition as in the lower mantle (Table 2). In most experiments, the starting compositions were loaded into folded Au foil capsules that were enclosed in welded Pt tubes to avoid the loss of Fe through the formation of Pt-Fe alloy. In experiments where the Ru-RuO_2 buffer was added, the mixtures were directly sealed into platinum capsules in order to avoid the possible reaction of Ru with the Au capsule. In experiments where PtO_2 was added, a Pt capsule was used to buffer the oxygen fugacity of the experiment through the Pt-PtO_2 buffer. For experiments where ReO_2 was added or for which a high temperature of ~ 2100 °C was employed, folded Re foil capsules were

adopted (Table 2). The capsules were 1 mm in diameter and 1.5 mm in length. In experiments S6950, S7132, and S7138, two capsules with 1 mm length were placed in the same assemblage on either side of the thermocouple.

High-pressure experiments were performed at 25 GPa and 1700-2100 °C in a 1200-tonne Kawai-type multi-anvil press at the Bayerisches Geoinstitut (Table 2). Long run durations of 12-24 h were employed for most experiments to facilitate chemical homogeneity of the run products (Table 2). Standard 7 mm edge-length Cr_2O_3-doped MgO octahedral pressure media with $LaCrO_3$ furnaces combined with 3 mm edge-length truncated tungsten carbide cubes (referred to as 7/3 assembly) were used. Temperature was monitored with a W97Re3-W75Re25 (D type) thermocouple inserted longitudinally through the wall of the furnace, with the hot junction at the midpoint of the heater (Fig. A.1).

The recovered samples were mounted in epoxy resin, sectioned and polished for analysis. Textural observations, preliminary phase identification and semi-quantitative chemical analyses of the recovered run products were performed using a scanning electron microscope (SEM) (ZEISS Gemini 1530) equipped with a field emission gun and energy-dispersive X-ray spectrometer (EDXS). Phase identification was made using a micro-focused X-ray diffractometer (Bruker, D8 DISCOVER) equipped with a two-dimensional solid-state detector (VÅNTEC500) and micro-focus Co-*Kα* radiation source (IμS) operated at 40 kV and 500 μA. For the characterization of some minor phases, the crystal structure was examined by selected area electron diffraction (SAED) in a transmission electron microscope (TEM, FEI Titan G2 80-200 S/TEM) operating at 200 kV. Thin foils for TEM analysis were prepared using a focused ion beam (FIB) instrument (FEI, Scios DualBeam). The chemical compositions of the mineral phases were obtained using a JEOL JXA-8200 electron probe microanalyzer (EPMA) operating at an acceleration voltage of 15 kV and a beam current of 5 nA. Counting times per element were 10 s on the peak and 5 s on the background with a defocused beam of 3 μm for Brg grains larger than 5 μm and focused beam for smaller Brg grains and other mineral phases. A low beam current, short counting times and defocused beam were used to minimize the amorphization and damage of Brg. Standards were enstatite for Mg and Si, Fe metal for Fe, corundum for Al, Ir metal for Ir, Pt metal for Pt, Re metal for Re and Ru metal for Ru. The composition of pure $MgSiO_3$ akimotoite single crystals, synthesized at 22 GPa and 1873 K, was also determined using the same settings as a secondary standard before each measurement to ensure that an accurate Mg/Si ratio was measured for these high-pressure phases. The Phi-rho-Z correction routine was applied for all analyses of this work.

Mössbauer measurements were performed on thin sections of recovered samples with a thickness of 30-500 µm at room temperature (298 K) in transmission mode on a constant acceleration Mössbauer spectrometer with a nominal 370 MBq ^{57}Co point source in a 12 µm Rh matrix. The dimensionless effective thickness of each sample was calculated from sample geometry, ^{57}Fe enrichment (Table 1) and chemical composition to give an effective thickness of roughly 5 mg Fe/cm^2 to avoid saturation effects. A piece of Ta foil drilled with a 500 µm diameter hole was used to select the area to be measured. Velocity scales were calibrated relative to 25 µm α-Fe foil. Spectra were collected using a velocity range of -5 to +5 mm/s for normal samples and -7 to +7 mm/s for samples containing magnetically ordered Fe metal phases over 1 to 7 days. Spectra were then folded and fitted to multiple doublets and sextets with pseudo-Voigt line shape using the MossA program and the full transmission integral was used (Prescher et al., 2012).

3. Results

3.1 Phase assemblages and compositions

Recovered phase assemblages are listed in Table 2 and full chemical analyses of Brg and coexisting phases are given in Table 3. Typical back-scattered electron (BSE) images of run products are shown in Fig. 1. In all experiments, coexisting Brg and Fp were successfully recovered together with the buffering phases which were dispersed throughout the charge. In the synthesis experiments performed with Re + ReO_2 or Ru + RuO_2 oxygen buffers, both phases were present (Fig. 1c, d). For experiments in which 20 wt. % Fe_2O_3 was added as the buffer material, however, no hematite was observed in the run products and a $(Mg,Fe)_2Fe_2O_5$ phase belonging to the $Mg_2Fe_2O_5$-Fe_4O_5 join was present instead (Fig. 1b). Trace amounts of two carbon phases were observed in a few experimental charges, indicating the presence of carbon in the starting material (Table 2, Fig. 1b). The carbon may have come from the absorption of atmospheric CO_2 by the oxygen buffering materials or possibly organic remnants from ethanol in which the sample powders were ground. Carbon appeared as the carbide Fe_3C in metal-saturated experiments and as carbonate at higher oxygen fugacities, in good agreement with the experiments of Stagno et al. (2011) (see supplementary information section A.1). In the low-Al and high-Fe bearing experiments where the Ru + RuO_2 buffer was added (S7113, S7138-1, S7138-2, S7046), an extra phase, $(Mg,Fe)(Fe,Ru,Si)_2O_4$, was present which had the $CaMn_2O_4$ or $CaTi_2O_4$ structure (from the SAED patterns in TEM). A minor amount of majorite garnet with the composition $Mg_{2.8}Fe_{0.5}Al_{1.4}Si_{3.3}O_{12}$ (H4746) and $Mg_{2.7}Fe_{0.8}Al_{1.4}Si_{3.1}O_{12}$ (S6920) was

observed in experiments at reduced conditions when employing starting materials with Al_2O_3 contents higher than 5.9 wt. %. The Al content of the majorite phase was more than three times that of coexisting Brg (Table 3). Note that garnet was not present in experiments with similar starting compositions run at higher oxygen fugacities, implying that the formation of ferric iron expanded the Brg stability field. In experiment S7214, which had a starting composition containing 12.3 wt. % Al_2O_3, an Al-rich phase $Mg_{1.37}Si_{0.42}Fe_{0.09}Al_{1.05}Ru_{0.07}O_4$ with the $CaFe_2O_4$ structure was found to coexist with Brg and Fp. In most experiments, the Al and Fe content of Brg are similar to the starting materials, except S7113 and S7138-1 where the Fe in Brg reduced to 0.06 atoms per formula unit (pfu) due to Fe entering the Ru-rich $(Mg,Fe)(Fe,Ru,Si)_2O_4$ phase and S6921, S6950-1 and S6950-2 where Fe in Brg increased to 0.21-0.24 atoms pfu due to the Fe partitioning between Brg and the Fe-rich $(Mg,Fe)_2Fe_2O_5$ phase. The mineral phases are chemically quite homogeneous, as can be assessed from the standard deviations on at least 20 microprobe analyses on each phase. Under the reducing conditions of Fe metal saturation, however, Fp shows greater compositional variations (S7122 and S7132-2, Table 3), which will be discussed in more detail in section 3.4.3.

3.2 Determination of oxygen fugacity

Oxygen fugacities in the experiments were either imposed by buffering assemblages or were measured using sliding redox sensors (Woodland and O'Neill, 1997). For experiments conducted at Fe metal saturation, the oxygen fugacity was measured with the equilibrium,

$$\underset{\text{alloy}}{2\,\mathrm{Fe}} + \mathrm{O_2} = \underset{\text{Fp}}{2\,\mathrm{FeO}} \qquad (3)$$

using the expression,

$$\log\left(f_{\mathrm{O_2}}\right) = \frac{\Delta G^0_{P,T\,(3)}}{\ln(10)\mathrm{R}T} + 2\log\left(a^{\mathrm{Fp}}_{\mathrm{FeO}}\right) - 2\log\left(a^{\mathrm{alloy}}_{\mathrm{Fe}}\right) \qquad (4)$$

where $\Delta G^0_{P,T\,(3)}$ is the standard Gibbs energy of equilibrium (3), determined using the thermodynamic and equation of state data in Table B.1, and a_i^j is the activity of component *i* in phase *j* and is equal to $x_i^j \times \gamma_i^j$, where x_i^j and γ_i^j are the mole fraction and activity coefficient of component *i* in phase *j*, respectively. The activity coefficient of FeO in Fp $(\gamma^{\mathrm{Fp}}_{\mathrm{FeO}})$ was determined from,

$$\mathrm{R}T\ln\gamma^{\mathrm{Fp}}_{\mathrm{FeO}} = W^{\mathrm{Fp}}_{\mathrm{MgFe}}\left(1 - x^{\mathrm{Fp}}_{\mathrm{FeO}}\right)^2 \qquad (5)$$

using the Margules interaction parameter $W^{\mathrm{Fp}}_{\mathrm{MgFe}} = 11 + 0.11P$ kJ/mol taken from Frost (2003) where *P* is pressure in GPa. In experiments where pure Fe was employed $a^{\mathrm{alloy}}_{\mathrm{Fe}} = 1$. In experiments where Ir metal was added the activity coefficient of Fe in the resulting Fe-Ir alloy ($\gamma^{\mathrm{alloy}}_{\mathrm{Fe}}$) was determined from,

$$\mathrm{R}T\ln\gamma^{\mathrm{alloy}}_{\mathrm{Fe}} = \left(-51814 + 736P - 21964x^{\mathrm{alloy}}_{\mathrm{Fe}}\right) \times \left(1 - x^{\mathrm{alloy}}_{\mathrm{Fe}}\right)^2 \quad (6)$$

where *P* is pressure in GPa (Stagno and Frost, 2010). In one experiment (S7120) the oxygen fugacity was determined from a Pt-Fe alloy using the Margules expression for $\gamma^{\mathrm{alloy}}_{\mathrm{Fe}}$ from Kessel et al. (2001):

$$\mathrm{R}T\ln\gamma^{\mathrm{alloy}}_{\mathrm{Fe}} = (-138000 + 94400x^{\mathrm{alloy}}_{\mathrm{Fe}}) \times (1 - x^{\mathrm{alloy}}_{\mathrm{Fe}})^2 \quad (7)$$

In experiments where hematite was added to the starting material and a $(Mg,Fe)_2Fe_2^{3+}O_5$ phase was formed in the resulting assemblage, the fo_2 was estimated using the equilibrium,

$$8\ \mathrm{FeO} + \mathrm{O_2} = 2\ \mathrm{Fe_4O_5} \quad (8)$$

Fp oxides

and the relation,

$$\log\left(f_{\mathrm{O_2}}\right) = \frac{\Delta G^0_{P,T\,(8)}}{\ln(10)\mathrm{R}T} + 2\log\left(a^{\mathrm{oxides}}_{\mathrm{Fe_4O_5}}\right) - 8\log\left(a^{\mathrm{Fp}}_{\mathrm{FeO}}\right) \quad (9)$$

Ideal mixing of Fe^{2+} and Mg was assumed such that $a^{\mathrm{oxides}}_{\mathrm{Fe_4O_5}} = (x^{\mathrm{oxides}}_{\mathrm{Fe^{2+}}})^2$, where $x^{\mathrm{oxides}}_{\mathrm{Fe^{2+}}} = \mathrm{Fe^{2+}}/(\mathrm{Fe^{2+}} + \mathrm{Mg})$. $\Delta G^0_{P,T\,(8)}$ was calculated using the data of Myhill et al. (2016) given in Table B.1.

Oxygen fugacities for the equilibria:

$$\mathrm{Ru} + \mathrm{O_2} = \mathrm{RuO_2} \quad (10)$$

were calculated from,

$$\log\left(f_{\mathrm{O_2}}\right) = \frac{\Delta G^0_{P,T\,(10)}}{\ln(10)\mathrm{R}T} \quad (11)$$

using the expression of Armstrong et al. (2020) for $\Delta G^0_{P,T\,(10)}$, and for the Re-ReO_2 equilibrium:

$$\mathrm{Re} + \mathrm{O_2} = \mathrm{ReO_2} \quad (12)$$

the oxygen fugacity was calculated according to:

$$\log\left(f_{\mathrm{O_2}}\right) = \frac{-451020 + 297.595T - 14.6585T\ln T - 34.96P^2 + [0.23(T - 293) + 9943.73]P}{\ln(10)\mathrm{R}T} \quad (13)$$

where *T* is temperature in kelvin and *P* is pressure in GPa (Campbell et al., 2006; Pownceby and O'Neill,

1994). The calculated oxygen fugacities for each experiment are listed in Table 2 and uncertainties were propagated from the chemical analyses of the various oxide and metal phases involved in the determinations.

3.3 Mössbauer spectroscopy $Fe^{3+}/\sum Fe$ ratio determinations

Selected Mössbauer spectra collected at room temperature are shown in Fig. 2. Because the bulk assemblages were measured, peaks from all iron-containing phases are present. Mössbauer spectra were deconvoluted using the minimum number of components (quadrupole doublets and magnetic sextets) required to achieve statistically acceptable fits to the data. The full transmission integral was used and conventional constraints for quadrupole doublets (i.e., components constrained to equal width and area) were applied. In many cases, three doublets were used to fit the spectra: one corresponding to Fe^{3+} in Brg and two to Fe^{2+} in Brg and Fp respectively (Fig. 2). In a few spectra, some hyperfine parameters had to be constrained due to peak overlap or weak peak intensities (Table B.2). The derived hyperfine parameters for Fe^{2+} (center shift, CS = ~ 1.1 mm/s, quadrupole splitting, QS = 1.60-2.30 mm/s) and Fe^{3+} (CS = 0.33-0.51 mm/s, QS = 0.29-0.96 mm/s) in Brg are listed in Table B.2 and compared with data in the literature in Fig. 2d, showing good agreement with previous studies (McCammon et al., 2013). While the hyperfine parameters allow Fe^{2+} to be assigned unambiguously to the A site (8-12 coordinated), the location of Fe^{3+} in the perovskite-type structure is difficult to resolve from QS values alone because high-spin Fe^{3+} in both the A and B sites have low values of QS (Lin et al., 2012; McCammon, 1998). The $Fe^{3+}/\Sigma Fe$ ratios in Brg determined from the relative areas of Fe^{2+} and Fe^{3+} Brg components are reported in Table 2. Uncertainties were estimated based on the fit statistics and from the uncertainties in the fitting model itself. Electron transfer between Fe^{2+} and Fe^{3+} of Brg was observed in some Mössbauer spectra of previous studies collected at ambient conditions in which case an additional doublet was assigned to Fe^{n+} (Fei et al., 1994; Lauterbach et al., 2000; McCammon, 1998; McCammon et al., 2004b). CS and QS values of Fe^{n+} lie between those observed for Fe^{2+} and Fe^{3+} (Fig. 2d), however, due to its peak overlapping with Fp, it was not able to be resolved in any of our spectra which always have Fp coexisting with Brg. Nevertheless, the Fe^{n+} component is smaller than 10 % with an Fe content smaller than 0.10 atoms pfu in Brg (Lauterbach et al., 2000) and is a combination of both Fe^{2+} and Fe^{3+} component, therefore, would only have a minor influence on the determined $Fe^{3+}/\Sigma Fe$ ratio of Brg in our study, which should be within the uncertainties of the

Mössbauer measurements.

No peaks from carbonate were observed in the spectra, most likely because the Fe contents measured for the carbonates in the experiments were always less than 2 mol. % (Table 3). Samples saturated with Fe metal show additional peaks indicating magnetically ordered phases (Fig. 2a, b), which were fitted to one or two magnetic sextets. The phase with the larger hyperfine magnetic field of H = ~ 33 T could be assigned to Fe metal and the other phase with a smaller hyperfine magnetic field of H = ~ 20 T could be assigned to Fe^0 in iron carbide. Some samples contain the additional Fe-bearing phases $(Mg,Fe)(Fe,Ru,Si)_2O_4$ (S7113, S7138-1) and $(Mg,Fe)_2(Fe,Al,Si)_2O_5$ (S6921, S6950-1, S6950-2). Although present in quite small proportions, these phases are Fe-rich but their hyperfine parameters are not suitably distinct for them to be separated from Brg and Fp. These phases are, therefore, not considered in the fitting process and for this reason we do not use these samples in fitting the thermodynamic models.

3.4 Site occupancies and substitution mechanisms in Brg

3.4.1 Al-bearing bridgmanite

In order to develop a model for the concentration and distribution of Brg cations in the Fe and Al-bearing system it was necessary to first understand the speciation in the individual Al- or Fe-bearing sub-systems. For the Al-Mg-Si-O system this is possible using previously published data (Kojitani et al., 2007; Liu et al., 2017, 2019a, b ; Navrotsky et al., 2003). In Fig. 3a, the Si content of Fe-free Al-bearing Brg is plotted against the Al content. Two solid lines indicate the expected trends for the CC substitution mechanism along the $MgSiO_3$-$AlAlO_3$ join and the OV substitution mechanism along the $MgSiO_3$-$MgAlO_{2.5}$ join. Experimental samples where bulk compositions having Mg ≤ Si (green circles) produced Brg samples that follow the CC trend but compositions with Mg > Si generally crystallized additional periclase and the Brg compositions fall initially at lower Al contents between the CC and OV trend lines (orange circles). The variation in the two substitution mechanisms for Brg from Mg > Si starting compositions can be seen more clearly in Fig. 3b, where the proportions of the two components are determined from the equation $Mg_xAl_zSi_yO_{x+1.5z+2y} = y\ MgSiO_3 + (x\text{-}y)\ MgAlO_{2.5} + 0.5\ (z\text{-}x\text{+}y)\ AlAlO_3$ (x+y+z = 2, Liu et al., 2017). The CC $AlAlO_3$ component increases monotonically with increasing Al content while the OV $MgAlO_{2.5}$ component initially increases to a maximum at Al = ~ 0.1 atoms pfu and then decreases upon a further increase in Al (Fig. 3b).

3.4.2 Fe-bearing bridgmanite

The cation distributions between A and B sites and the corresponding substitution mechanisms in Fe-bearing and Fe, Al-bearing Brg can be determined using the combined results of EPMA and Mössbauer spectroscopy analyses. For Fe-bearing Brg, the distribution of Fe^{3+} on the A and B sites is determined from $\mathrm{Fe}_{\mathrm{A}}^{3+} = 1 - \mathrm{Mg} - \mathrm{Fe}^{2+}$ and $\mathrm{Fe}_{\mathrm{B}}^{3+} = 1 - \mathrm{Si}$ after total cations have been normalized to 2 (Table 4). Experiments performed in the Fe-Mg-Si-O system coexisting with Fp are plotted in Fig. 4a, with the trends expected for the OV (Mg,Fe)$FeO_{2.5}$ and the CC $FeFeO_3$ substitutions indicated. As for the periclase-saturated Al-Mg-Si-O system, the data fall close to the OV trend when Fe^{3+} is less than 0.03 atoms pfu but at higher Brg bulk Fe^{3+} concentrations, i.e., higher oxygen fugacity, the data move closer to the CC substitution. The change between these two substitution mechanisms, as for the Al-bearing system, appears to occur rapidly over within a narrow Fe^{3+} range of ~ 0.02 atoms pfu. Data from Frost and Langenhorst (2002), Fei et al. (2020) and McCammon et al. (2004b) in the presence of Fp and Lauterbach et al. (2000) and Hummer and Fei (2012) where Fp is absent, are also shown for comparison. Compared with the Al-Mg-Si-O system, the role of Fp is much less obvious in determining the substitution mechanism (Fig. 4a). This is mainly because the concentrations of Fe^{3+} are very low and susceptible to greater uncertainties than for the Al-Mg-Si-O system due to the need to also combine Mössbauer measurements. Many of the previous studies used relatively high EPMA beam currents that may have also led to damage of the Brg samples that can influence the Mg/Si ratio of the analyses. In Fig. 4b, the mole fractions of the $FeFeO_3$ and (Mg,Fe)$FeO_{2.5}$ components are plotted as a function of the fo_2 (thus total Fe^{3+} content). As for Al in the Al-Mg-Si-O system, the CC component increases with increasing ferric Fe content while the OV component first increases and then decreases. The OV component reaches a maximum at much lower trivalent cation concentration (~ 0.03 atoms pfu Fe^{3+}) compared with OV component in the Al-Mg-Si-O system (~ 0.1 atoms pfu Al) and the proportion of the OV component is also smaller, being at most 2 mol. % in the Fe-bearing system compared to ~ 5 mol. % in the Al-bearing system (Liu et al., 2017).

3.4.3 Fe and Al-bearing bridgmanite

For Fe and Al-bearing Brg complexity arises because both Fe^{3+} and Al can in principle occupy both A and B sites, as they do in Fe-free and Al-free systems. Although Mössbauer spectroscopy results are inconclusive in determining the Fe^{3+} site assignment (Lin et al., 2013; McCammon, 1998), there is some

evidence from site occupancies and polyhedral volumes determined using single crystal X-ray diffraction (Huang, 2020), that when both cations are present in sub equal concentrations, at least at 25 GPa, then there is a strong preference of Fe^{3+} and Al for the A and B sites respectively, in accordance with the expectations based on cation radii. However, obviously when either trivalent cation is in excess it must occupy the other site to maintain charge balance and configurational entropy considerations alone imply that complete ordering is unlikely even when both cations have the same concentration. This latter issue will be revisited in the section on thermodynamic modelling. Initially, however, site occupancies are simply assigned by assuming the B site is first filled with the Al cations and the A site with Fe^{3+} and cations of either type that remain after the site occupancies reach unity are placed on the other site. If charge balance is not attained, then OV are assumed to occur. The resulting cation distribution between A and B sites are reported in Table 4. As indicated in Fig. 5a, this procedure, for which data from previous studies is also included, never results in an excess of trivalent cations on the A site, which would require an A site cation vacancy to achieve charge balance. At Fp saturated conditions the behavior mirrors that for Fe-free and Al-free Brg where both OV and CC substitution mechanisms are important at low M^{3+} ($M^{3+} = Al^{3+} + Fe^{3+}$) concentrations, whereas the CC mechanism becomes a more favorable substitution mechanism at higher M^{3+} concentrations. Sources of uncertainty are the same as those discussed in the previous section. Based on the ordering assumption, B site Fe^{3+} is zero when $Fe^{3+} \leq$ Al. However, when $Fe^{3+} >$ Al, i.e., $\Delta(Fe^{3+}\text{-Al}) > 0$, Fe^{3+} also occupies the B site and in Fig. 5b, the comparison with the OV and CC trend lines seems to bear out the general picture of an initial small OV fraction being over taken by CC domination at higher M^{3+} concentration. The uncertainties are again relatively large due to the use of Mössbauer data and it becomes very difficult to proportion the two mechanisms, particularly when just the Fe^{3+} is considered. In general, it appears that OV become less favorable in Fe-bearing systems compared to the Al-Mg-Si-O system.

3.5 $Fe^{3+}/\sum Fe$ dependence on fo_2, composition and temperature in bridgmanite

Four sets of experiments were performed at 1973 K and 25 GPa and at oxygen fugacities ranging between - 1 and + 9 log units relative to the iron-wüstite buffer (Table 4). In the first three sets the total iron content of the starting material was kept constant at 0.11 atoms pfu but for each set the Al concentration was either 0, 0.07 or 0.11 atoms pfu. In the recovered Brg samples some variation occurred from these nominal starting compositions due to interphase partitioning and interaction with oxygen-

buffering phases such as Fe metal. A time study showed that oxidation of Fe^{3+} in Brg from initially reduced starting compositions occurred rapidly, resulting in similar $Fe^{3+}/\sum Fe$ ratios of Brg in 4 h (S7113) and 12 h (S7138-1) experiments at 1973 K, therefore we consider redox equilibrium was reached during our experiments. It is also unlikely that the observed trends in Brg ferric iron content with fO_2 would develop if redox equilibrium could not be approached on the experimental timescales.

Previous studies have implied that the $Fe^{3+}/\Sigma Fe$ ratio of Fe and Al-bearing Brg, is governed mainly by the Al content with no apparent fO_2 dependence (Frost et al., 2004; McCammon et al., 2004b; Nakajima et al., 2012), but this was mainly based on the similarity in Brg Fe^{3+} contents between experiments performed in both Fe and Re capsules. As shown in Fig. 6 the $Fe^{3+}/\Sigma Fe$ ratio and Fe^{3+} cation content of both Al-free and Fe and Al-bearing Brg are clearly dependent on fO_2. The nature of this relationship, however, changes with increasing Al content, which results in raised $Fe^{3+}/\Sigma Fe$ ratios for the same fO_2 but also causes the relationship between fO_2 and $Fe^{3+}/\Sigma Fe$ ratio to become less steep. This change in the relationship also means that the effect of the Al content on the $Fe^{3+}/\Sigma Fe$ ratio practically disappears at high fO_2, as shown in Fig. 7a. Previous arguments for the Al content having a much stronger effect than fO_2 on the $Fe^{3+}/\Sigma Fe$ ratio of Brg (Frost et al., 2004; McCammon et al., 2004b) are supported by the results, particularly at lower oxygen fugacities. At an fO_2 of approximately IW - 1, for example, an increase in the Brg Al content from zero to 0.07 atoms pfu raises the $Fe^{3+}/\Sigma Fe$ ratio from ~ 0.1 to ~ 0.55, whereas an increase in fO_2 by ~ 4 log units raises the $Fe^{3+}/\Sigma Fe$ ratio by only ~ 0.2. Fig. 6a also demonstrates this weak fO_2 trend for Al-bearing Brg. The fO_2 effect on the proportion of Fe^{3+} cations is also relatively small for Al-bearing samples. The lack of any fO_2 dependence found for Al-bearing Brg in previous studies likely arises because the range of fO_2 studied was relatively small and different oxygen fugacities were inferred from the use of different capsule materials, without distributing the buffering material itself throughout the sample, as in this study. Using different capsule materials alone, in the absence of a fluid or melt phase, may not be sufficient for redox equilibrium throughout the sample to be obtained.

Higher Brg total Fe contents are coupled to a weak decrease in the $Fe^{3+}/\Sigma Fe$ ratio as shown in Fig. 7b. One experiment (S7209, Table 2), shown in Fig. 6a was performed at a temperature 400 K higher and with Brg of 0.12 Al and 0.12 Fe atoms pfu. Compared to the experiments at 1973 K and the same fO_2 the Brg $Fe^{3+}/\Sigma Fe$ ratio is lower. A decrease in the Brg $Fe^{3+}/\Sigma Fe$ ratio with temperature is also consistent with results from previous studies shown in Fig. 7b. This relative complexity in factors that influence the Brg $Fe^{3+}/\Sigma Fe$

ratio, i.e., Al, Fe, *T* and fO_2, is probably another reason why the fO_2 dependence was not previously observed because it requires all other dependences to be held constant in order for the fO_2 dependence to be observed.

4 Discussion

4.1 Thermodynamic models to describe the composition and site occupancy of bridgmanite as a function of fO_2 and composition

4.1.1 The Al-Mg-Si-O system

A thermodynamic model that aims to reproduce the trivalent cation concentration in Brg needs to take both the CC and OV substitution mechanisms into account. The OV mechanism cannot be overlooked because it appears to be still important in Fe-bearing systems, particularly at low oxygen fugacities, which are likely most typical for the lower mantle. The concentration of OVs is the highest and the most well constrained in the Al-Mg-Si-O system, as determined in recent studies (Fig. 3b), which is, therefore, a good starting point for developing a model for this component. The $MgAlO_{2.5}$ Brg concentration goes through a maximum at approximately 0.07 Al atoms pfu, which can in principle be described using the equilibrium,

$$\underset{\text{Brg}}{2\ \mathrm{MgAlO_{2.5}}} = \underset{\text{Brg}}{\mathrm{AlAlO_3}} + \underset{\text{Per}}{2\ \mathrm{MgO}} \quad (14)$$

In order to reproduce the $MgAlO_{2.5}$ maximum using these components it becomes necessary to introduce very large non-ideal interaction parameters, in excess of 100 kJ/mol. However, by using an OV component endmember which is closer to the maximum concentration of OVs, much smaller and seemingly more reasonable interaction parameters are required. Since the maximum amount of the OV component that has been experimentally reported is 0.064 (9) pfu, at 27 GPa and 2400 K (Liu et al., 2019a), and experiments show this to decrease with increasing pressure and decreasing temperature (Liu et al., 2017), the $\mathrm{MgSi_{7/8}Al_{1/8}O_{15/16}O_2}$ component was chosen arbitrarily to be sufficiently close in composition to this maximum level. The change in concentration can be described with the equilibrium:

$$\underset{\text{Brg}}{\mathrm{MgSi_{7/8}Al_{1/8}O_{15/16}O_2}} = \underset{\text{Brg}}{1/16\ \mathrm{AlAlO_3}} + \underset{\text{Brg}}{7/8\ \mathrm{MgSiO_3}} + \underset{\text{Per}}{1/8\ \mathrm{MgO}} \quad (15)$$

At equilibrium, the standard reaction Gibbs energy can be expressed by:

$$\Delta G^{0}_{(15)} = -\mathrm{R}T\ln \frac{\left(a^{\mathrm{Brg}}_{\mathrm{AlAlO_3}}\right)^{1/16}\left(a^{\mathrm{Brg}}_{\mathrm{MgSiO_3}}\right)^{7/8}\left(a^{\mathrm{Per}}_{\mathrm{MgO}}\right)^{1/8}}{a^{\mathrm{Brg}}_{\mathrm{MgSi_{7/8}Al_{1/8}O_{15/16}O_2}}} \quad (16)$$

taking the standard state to be the pure endmembers at 25 GPa and 1973 K. $a^{\mathrm{Per}}_{\mathrm{MgO}}$, the activity of the MgO component in periclase is unity and $a^{\mathrm{Brg}}_{\mathrm{AlAlO_3}}$, $a^{\mathrm{Brg}}_{\mathrm{MgSiO_3}}$ and $a^{\mathrm{Brg}}_{\mathrm{MgSi_{7/8}Al_{1/8}O_{15/16}O_2}}$ are defined as:

$$a^{\mathrm{Brg}}_{\mathrm{AlAlO_3}} = x^{\mathrm{Brg}}_{\mathrm{AlAlO_3}} \times \gamma^{\mathrm{Brg}}_{\mathrm{AlAlO_3}} \quad (17a)$$

$$a^{\mathrm{Brg}}_{\mathrm{MgSiO_3}} = x^{\mathrm{Brg}}_{\mathrm{MgSiO_3}} \times \gamma^{\mathrm{Brg}}_{\mathrm{MgSiO_3}} \quad (17b)$$

$$a^{\mathrm{Brg}}_{\mathrm{MgSi_{7/8}Al_{1/8}O_{15/16}O_2}} = x^{\mathrm{Brg}}_{\mathrm{MgSi_{7/8}Al_{1/8}O_{15/16}O_2}} \times \gamma^{\mathrm{Brg}}_{\mathrm{MgSi_{7/8}Al_{1/8}O_{15/16}O_2}} \quad (17c)$$

where x^{A}_{i} is the ideal mixing activity of component *i* in phase A and *γ* is the activity coefficient. $MgSiO_3$ Brg has two oxygen sites, O1 with a multiplicity of 1 and O2 with a site multiplicity of 2. If we consider that oxygen vacancies occur on one half of the available O1 sites then,

$$x^{\mathrm{Brg}}_{\mathrm{MgSi_{7/8}Al_{1/8}O_{15/16}O_2}} = 1.841\, x_{\mathrm{Mg,A}}\left(x_{\mathrm{Al,B}}\right)^{1/8}\left(x_{\mathrm{Si,B}}\right)^{7/8}\left(x_{\mathrm{V,O1}}\right)^{1/16}\left(x_{\mathrm{O,O1}}\right)^{15/16} \quad (18a)$$

where $x_{\mathrm{Mg,A}}$, $x_{\mathrm{Al,B}}$, and $x_{\mathrm{Si,B}}$ are the mole fractions of Mg on the A site, Al and Si on the B site respectively, and $x_{\mathrm{V,O1}}$ and $x_{\mathrm{O,O1}}$ are the mole fractions of vacancies and oxygen on the O1 site where $x_{\mathrm{V,O1}} = 0.5\,(x_{\mathrm{Al,B}} - x_{\mathrm{Al,A}})$. The coefficient 1.841 in equation (18a) is required such that the activity of the endmember $\mathrm{MgSi_{7/8}Al_{1/8}O_{15/16}O_2}$ is equal to unity. For the CC substitution of Al, it is assumed that charge balance results in local ordering of Al on each site, such that the ideal mixing activity of the $AlAlO_3$ component is:

$$x^{\mathrm{Brg}}_{\mathrm{AlAlO_3}} = x_{\mathrm{Al,A}} \times x_{\mathrm{O,O1}} \quad (18b)$$

The mole fraction of $MgSiO_3$ component in Brg is,

$$x^{\mathrm{Brg}}_{\mathrm{MgSiO_3}} = x_{\mathrm{Mg,A}} \times x_{\mathrm{Si,B}} \times x_{\mathrm{O,O1}} \quad (18c)$$

Binary symmetric models were employed to describe the non-ideality of mixing. For the OV component the activity coefficient is, for example,

$$\mathrm{R}T\ln\gamma^{\mathrm{Brg}}_{\mathrm{MgSi_{7/8}Al_{1/8}V_{1/16}O_{15/16}O_2}} = W^{\mathrm{Brg}}_{\mathrm{MgAl,A}}\left(1 - x_{\mathrm{Mg,A}}\right)^2 + W^{\mathrm{Brg}}_{\mathrm{AlSi,B}}\left(1 - x_{\mathrm{Al,B}}\right)^2 + W^{\mathrm{Brg}}_{\mathrm{OV,O1}}\left(1 - x_{\mathrm{V,O1}}\right)^2 \quad (19)$$

where *W* is a Margules parameter that describes the interaction between Mg-Al on the A site, Si-Al on the

B site and O-V on the O1 site. Similar equations for the activity coefficients of the $MgSiO_3$ and $AlAlO_3$ components are given in the supplementary information A.2 in addition to the combined expression for equation (16). By substituting the experimentally determined Brg compositions shown in Fig. 3b into equation (16) the data can be fitted using a non-linear least-squares algorithm to determine the three interaction parameters and $\Delta G^0_{(15)}$. However, values for the three interaction parameters are highly correlated, and a range of values will provide a satisfactory fit. A reasonable solution is obtained by considering only the interaction between Al and Si on the B site with $W^{\mathrm{Brg}}_{\mathrm{AlSi,B}} = -30\ \mathrm{kJ/mol}$ and $\Delta G^0_{(15)} = -19.5\ \mathrm{kJ/mol}$ at 27 GPa and 2000 K. This is not to imply that the other interaction terms are zero, but simply that there is insufficient chemical variation through which to refine all three terms and the simplest satisfactory fit is obtained by refining only the term $W^{\mathrm{Brg}}_{\mathrm{AlSi,B}}$. The resulting model can be seen in Fig. 3b and fits the experimental data very well. Two further fits with slightly different parameters are also shown for comparison. A list of the interaction parameters used in this study was summarized in Table 5.

4.1.2 The Fe-Mg-Si-O system

The same approach as described in the previous section is used for the Fe-Mg-Si-O system, with the distribution of Fe^{3+} between Brg cation sites described by the equilibrium,

$$\underset{\text{Brg}}{\mathrm{MgSi_{7/8}Fe_{1/8}O_{15/16}O_2}} = 1/16\ \underset{\text{Brg}}{\mathrm{FeFeO_3}} + 7/8\ \underset{\text{Brg}}{\mathrm{MgSiO_3}} + 1/8\ \underset{\text{Fp}}{\mathrm{MgO}} \tag{20}$$

The standard Gibbs energy of reaction is then:

$$\Delta G^0_{(20)} = -\mathrm{R}T\ln \frac{\left(a^{\mathrm{Brg}}_{\mathrm{FeFeO_3}}\right)^{1/16}\left(a^{\mathrm{Brg}}_{\mathrm{MgSiO_3}}\right)^{7/8}\left(a^{\mathrm{Fp}}_{\mathrm{MgO}}\right)^{1/8}}{a^{\mathrm{Brg}}_{\mathrm{MgSi_{7/8}Fe_{1/8}O_{15/16}O_2}}} \tag{21}$$

The activities of the Brg components are,

$$a^{\mathrm{Brg}}_{\mathrm{FeFeO_3}} = x^{\mathrm{Brg}}_{\mathrm{FeFeO_3}} \times \gamma^{\mathrm{Brg}}_{\mathrm{FeFeO_3}} \tag{22a}$$

$$a^{\mathrm{Brg}}_{\mathrm{MgSiO_3}} = x^{\mathrm{Brg}}_{\mathrm{MgSiO_3}} \times \gamma^{\mathrm{Brg}}_{\mathrm{MgSiO_3}} \tag{22b}$$

$$a^{\mathrm{Brg}}_{\mathrm{MgSi_{7/8}Fe_{1/8}O_{15/16}O_2}} = x^{\mathrm{Brg}}_{\mathrm{MgSi_{7/8}Fe_{1/8}O_{15/16}O_2}} \times \gamma^{\mathrm{Brg}}_{\mathrm{MgSi_{7/8}Fe_{1/8}O_{15/16}O_2}} \tag{22c}$$

and for MgO in Fp,

$$a_{\mathrm{MgO}}^{\mathrm{Fp}} = x_{\mathrm{MgO}}^{\mathrm{Fp}} \times \gamma_{\mathrm{MgO}}^{\mathrm{Fp}} \tag{22d}$$

As for the Fe-free model, the ideal mixing activities are,

$$x_{\mathrm{MgSi_{7/8}Fe_{1/8}O_{15/16}O_2}}^{\mathrm{Brg}} = 1.841\, x_{\mathrm{Mg,A}} \left(x_{\mathrm{Fe,B}}\right)^{1/8} \left(x_{\mathrm{Si,B}}\right)^{7/8} \left(x_{\mathrm{V,O1}}\right)^{1/16} \left(x_{\mathrm{O,O1}}\right)^{15/16} \tag{23a}$$

$$x_{\mathrm{FeFeO_3}}^{\mathrm{Brg}} = x_{\mathrm{Fe,A}} \times x_{\mathrm{O,O1}} \tag{23b}$$

$$x_{\mathrm{MgSiO_3}}^{\mathrm{Brg}} = x_{\mathrm{Mg,A}} \times x_{\mathrm{Si,B}} \times x_{\mathrm{O,O1}} \tag{23c}$$

Symmetric models given in the supplementary information A.3 are used to describe the activity coefficients of the three components, where by this time a ternary model is required to describe Fe^{2+}-Mg-Fe^{3+} mixing on the A site. Because the proportions of Fe^{3+} and Fe^{2+} in Brg depend also on the fo_2 a further equilibrium is required to define their concentration, i.e.,

$$\underset{\text{Fp}}{2\ \mathrm{FeO} + 1/2\ \mathrm{O_2}} = \underset{\text{Brg}}{\mathrm{FeFeO_3}} \tag{24}$$

for which the condition of equilibrium is,

$$\Delta G_{(24)}^{0} = -\mathrm{R}T\ln \frac{a_{\mathrm{FeFeO_3}}^{\mathrm{Brg}}}{\left(a_{\mathrm{FeO}}^{\mathrm{Fp}}\right)^2 \left(f_{O_2}\right)^{1/2}} \tag{25}$$

The activities of $FeFeO_3$ in Brg and FeO in Fp are defined as in equations (22a) and (22d) and calculated using the same activity composition data. For each experimental data point obtained in this study standard state Gibbs free energy terms are calculated from equations (21) and (25). Two constant values of $\Delta G_{(20)}^{0}$ and $\Delta G_{(24)}^{0}$ should then be obtained for all data. Brg site assignments based on EPMA and Mössbauer data have large uncertainties, however, relative to the small concentrations of Fe^{3+} involved. To overcome this the experimental data are fitted by making no a priori assumptions on the site assignments and allowing the site occupancies of Fe^{3+} on the A and B Brg sites to vary during the refinement under the constraint of mass balance. In a least-squares refinement the Fe^{3+} site occupancies are found where the set of experiments can be fitted with the two constant ΔG^{0} terms. In fact, this method leads to a range of solutions with the best result judged by the agreement with the experimental fo_2–Fe^{3+} relationship, shown in Fig. 6b, and with the proportions of the two components, shown in Fig. 4b. This result is achieved with $W_{\mathrm{MgFe^{3+},A}}^{\mathrm{Brg}} = W_{\mathrm{Fe^{2+}Fe^{3+},A}}^{\mathrm{Brg}} = 11\ \mathrm{kJ/mol}$ and $W_{\mathrm{Fe^{3+}Si,B}}^{\mathrm{Brg}} = -28\ \mathrm{kJ/mol}$, which gives $\Delta G_{(20)}^{0} = -21\ \mathrm{kJ/mol}$ and $\Delta G_{(24)}^{0} = 133\ \mathrm{kJ/mol}$ (Table 5). $W_{\mathrm{OV,O1}}^{\mathrm{Brg}}$ was assumed to be zero and $W_{\mathrm{MgFe^{2+}}}^{\mathrm{Brg}} = 4.9\ \mathrm{kJ/mol}$ was

taken from Nakajima et al. (2012). Note that in Fig. 6b the data that appear to be in poor agreement with the model at IW + 7.7 have a Brg bulk Fe content of 0.05 atoms pfu, whereas the other data points as well as the model have Fe ~ 0.1 atoms pfu. The agreement between the experimental data and the model is reasonable but the curvature in the fO_2-$Fe^{3+}/\Sigma Fe$ relationship is not perfectly reproduced (Fig. 6a). It was not possible to find a solution that fitted both the total Fe^{3+} content and the Fe^{3+} speciation perfectly, slightly better solutions could be found that assumed very little of the CC component, but this was deemed to be in poor agreement with the experimentally determined site occupancies. Finding more complex models that provide a better fit are probably not justified by the current data coverage and uncertainties.

4.1.3 The Fe-Al-Mg-Si-O system

In order to build a thermodynamic model that describes the effects of Al, total Fe content and fO_2 on the Brg Fe^{3+} content three Brg components need to be considered. By including a mass balance constraint for the bulk Al content three equilibria are then required to describe the site occupancies, i.e.,

$$\underset{\text{Brg}}{\mathrm{MgSi_{7/8}Al_{1/8}O_{15/16}O_2}} = 1/16\ \underset{\text{Brg}}{\mathrm{AlAlO_3}} + 7/8\ \underset{\text{Brg}}{\mathrm{MgSiO_3}} + 1/8\ \underset{\text{Fp}}{\mathrm{MgO}} \quad (26)$$

$$\underset{\text{Brg}}{\mathrm{MgSi_{7/8}Fe_{1/8}O_{15/16}O_2}} = 1/16\ \underset{\text{Brg}}{\mathrm{FeFeO_3}} + 7/8\ \underset{\text{Brg}}{\mathrm{MgSiO_3}} + 1/8\ \underset{\text{Fp}}{\mathrm{MgO}} \quad (27)$$

$$2\ \underset{\text{Fp}}{\mathrm{FeO}} + \underset{\text{Brg}}{\mathrm{AlAlO_3}} + 1/2\ \mathrm{O_2} = 2\ \underset{\text{Brg}}{\mathrm{FeAlO_3}} \quad (28)$$

Expressions for the standard Gibbs energies for equilibria (26) and (27) are given in equations (16) and (21) and for equilibrium (28),

$$\Delta G^0_{(28)} = -\mathrm{R}T\ln\frac{\left(a^{\mathrm{Brg}}_{\mathrm{FeAlO_3}}\right)^2}{(a^{\mathrm{Fp}}_{\mathrm{FeO}})^2\, a^{\mathrm{Brg}}_{\mathrm{AlAlO_3}} \left(f_{O_2}\right)^{1/2}} \quad (29)$$

For simplicity, ideal mixing was assumed for Brg trivalent cations. In comparison to the previous models, short range ordering is not assumed due to the possibility that either Fe^{3+} or Al^{3+} could provide charge balance on the other site, therefore the activity expressions,

$$a^{\mathrm{Brg}}_{\mathrm{AlAlO_3}} = x_{\mathrm{Al,A}} \times x_{\mathrm{Al,B}} \quad (30a)$$

$$a^{\mathrm{Brg}}_{\mathrm{FeFeO_3}} = x_{\mathrm{Fe^{3+},A}} \times x_{\mathrm{Fe^{3+},B}} \quad (30b)$$

$$a^{\mathrm{Brg}}_{\mathrm{FeAlO_3}} = x_{\mathrm{Fe^{3+},A}} \times x_{\mathrm{Al,B}} \quad (30c)$$

are used, whereas expressions for the other components remain the same as the ideal mixing activities given in the previous sections. Values for $\Delta G^0_{(26)}$, $\Delta G^0_{(27)}$ and $\Delta G^0_{(28)}$ are calculated for each experimental data point by allowing the site occupancies of Fe^{3+} on the A and B sites and Al on the A site to vary in a minimisation routine that finds sets of occupancies where ΔG^0 values for each of the three equilibria are identical across all data points. The Al content on the B site and the Fe^{2+} content on the A site are determined from a mass balance using the bulk Al and Fe contents of the experimental samples. The experimental fo_2 is employed and the Mg and Si sites are constrained by summing site occupancies to unity. The Fe content in Fp was also refined based on a Mg-Fe^{2+} partitioning model between Brg and Fp (Nakajima et al., 2012) as described in section 4.2. The experimental Fp compositions were not used because Fe-Mg exchange between Brg and Fp is slow at lower mantle conditions (Holzapfel et al., 2005) and equilibrium in some experiments is hard to achieve within feasible experimental durations. This is especially the case at low oxygen fugacities. As can be seen from Fig. 8, however, the majority of the experimental data agree very well with the Fe-Mg exchange model, suggesting achievement of chemical equilibrium. Cases where the experimental Fp Fe^{2+} content is higher were all in equilibrium with iron metal, where iron oxidation drives the Fe content of Fp initially up but equilibrium with Brg is in some cases not achieved. The good agreement with the majority of the data indicates that Al and Fe^{3+} incorporation in Brg has no significant influence on Fe^{2+}-Mg exchange with Fp.

A range of successful sets of constant ΔG^0 values can be found for the experimental parameters with the overall optimisation then judged by how accurately the total Fe^{3+} content of each experiment is matched. The best fit values of ΔG^0 for the three equilibria (26-28) are reported in Table 6. ΔG^0 values for the same equilibria in the Fe-Mg-Si-O and Al-Mg-Si-O systems deviate due to the slightly different ideal mixing activity expressions and the use of activity coefficients. Models that were totally consistent throughout the three systems i.e., employed the same values of ΔG^0 for equilibria (15) and (26) and considered non-ideal mixing on the B site with the terms determined in each sub-system, were not only much more complicated, but also provided slightly poorer agreement with the experimental data. In order to check the consistency of the model, ΔG^0 values for three other dependent equilibria:

$$\underset{\text{Brg}}{\mathrm{AlAlO_3}} + \underset{\text{Brg}}{\mathrm{FeFeO_3}} = 2\ \underset{\text{Brg}}{\mathrm{FeAlO_3}} \quad (31)$$

$$2\ \mathrm{MgAlO_{2.5}} = \mathrm{AlAlO_3} + 2\ \mathrm{MgO} \quad (32)$$
Brg Brg Fp

$$2\ \mathrm{MgFeO_{2.5}} = \mathrm{FeFeO_3} + 2\ \mathrm{MgO} \quad (33)$$
Brg Brg Fp

were also calculated for each experiment and found to have near identical values across the entire data set used, as summarized in Table 6.

The agreement between the resulting model and the experimental data can be evaluated in Fig. 6 where the Al-free data and model are also shown. One data point in Fig. 6b deviates from the model at 0.07 Al and 0.07 Fe atoms pfu at ~ Δ IW = 2 because it has a lower total Fe content than the other data points and the model calculation, as indicated. The agreement with the experimental data in both total Fe^{3+} and $Fe^{3+}/\Sigma Fe$ is very good, particularly considering that the model has only three adjustable parameters. In Al-Mg-Si-O and Fe-Mg-Si-O systems, large interaction parameters (Table 5) were required to produce the large OV substitution bumps in a small composition range (Fig. 3b, 4b). Similar activity coefficient models were also tested for the Fe-Al-Mg-Si-O system but no significant improvement in the data fitting was achieved, at least not in proportion to the level of complexity that was then introduced. This does not mean that the site mixing is ideal or the large interaction parameters between Al or Fe^{3+} and Si at the B site (Table 5) disappear in the Fe-Al-Mg-Si-O system, but rather that activity coefficient relations do not change sufficiently over the compositional range examined to have a significant effect and their influence, which remains relatively constant is, therefore, incorporated in the determined ΔG^0 values.

It would of course be more satisfying for the Fe-Al-Mg-Si-O model to also describe the results in the Al-free and Fe-free sub-systems. However, as described above, including B-site interaction terms and using values of ΔG^0derived from the sub-systems resulted in a poorer overall fit to the experimental data. This can be partly explained by the fact that the significant maximum in OV proportion seen in the Al-Mg-Si-O system becomes much weaker and not sufficiently defined in the Fe-Al-Mg-Si-O system to allow the B site interaction parameter to be meaningfully refined. Deriving a model that collapses down to describe the Fe-free system was also not considered a priority as Fe-free Brg is unlikely to exist in the mantle. Fig. 7 also shows the model calculations as a function of Brg Al and Fe content. The model does not extrapolate to match the results of the Al-free data, again probably due to the assumption of Brg B-site ideal mixing. While this is unfortunate, it has to be recognised that the Fe-Mg-Si-O model does not provide an optimal fit to the experimental data, and particularly the OV concentrations, even in that sub-system, so it does not seem

546 to be worthwhile to force the Fe-Al-Mg-Si-O parameters to agree with this model at the expense of model
547 simplicity and accuracy. Until this situation is improved by either more data or a better insight into the
548 behaviour of the OV component in the Fe-Mg-Si-O system, the use of the Fe-Al-Mg-Si-O model will remain
549 limited to Al contents > 0.02 atoms pfu.

550 The Fe^{3+} content and its distribution over A and B sites in Brg at 25 GPa and 1973 K as well as the
551 composition of coexisting Fp can be obtained at any given fo_2 and Brg bulk Fe and Al content. In Fig. 9 model
552 curves are shown calculated for different Brg compositions as a function of fo_2 and compared with the
553 experimental data points. Both the Al and Fe^{3+} site occupancies and the OV proportion are in good
554 agreement. As the Fe^{3+} content increases Al is pushed out of the A site and into the B site, which is more
555 evident when Fe^{3+} > Al. At the same time the amount of trivalent cations charge balanced in the B site
556 through OV decreases. At high fo_2 the trivalent cation proportions can be described almost completely with
557 a charge-coupled $Fe^{3+}AlO_3$ component when $Fe^{3+} \approx$ Al, however, at lower oxygen fugacities both the $AlAlO_3$
558 and $(Mg,Fe)AlO_{2.5}$ components are present, although the latter is also near negligible in proportion.
559 Constraining the concentration of OV at oxygen fugacities that are more realistic for the bulk of the lower
560 mantle, however, is likely to be important for Brg transport properties (Grüninger et al., 2019). Fig. 9c
561 shows the results of one experiment (S7214) with an Al content of 0.22 atoms pfu, which was not used in
562 the model calibration but is reproduced by the calculation very well. Surprisingly the data point has a quite
563 high OV content, which is also matched very well by this relatively simple model.

564 **4.2 Composition of bridgmanite and ferropericlase as a function of oxygen fugacity for a pyrolite**
565 **assemblage**

566 Using the model described above it is possible to calculate the compositions for coexisting Brg and Fp
567 as a function of fo_2 for a given bulk composition. The pyrolite bulk composition employed by Irifune (1994)
568 (Table B.3) is used for this purpose and assumed to contain only Brg, Fp and $CaSiO_3$ perovskite at 25 GPa,
569 i.e. we ignore the fraction of garnet that disappears within the first few GPa of the lower mantle. The Fe^{2+}-
570 Mg distribution coefficient between Brg and Fp, $K_D = (x^{Brg}_{FeSiO_3}/x^{Brg}_{MgSiO_3})/(x^{Fp}_{FeO}/x^{Fp}_{MgO})$, is described by:

571 $$RT\ln K_D = -\Delta G^0(P,T) - W^{Brg}_{FeMg}\left(1 - 2x^{Brg}_{FeSiO_3}\right) + W^{Fp}_{FeMg}\left(1 - 2x^{Fp}_{FeO}\right) \quad (34)$$

572 where ΔG^0 =(22300 + 400*P* + 4.0*T*) J/mol, W^{Brg}_{FeMg} = 4900 J/mol, W^{Fp}_{FeMg}= (11000 + 110*P*) J/mol and

pressure (*P*) is in GPa and temperature (*T*) is in K (Nakajima et al., 2012). A mass balance is constructed to determine the mineral compositions and proportions corresponding to the bulk composition with the Fe^{2+} and Fe^{3+} contents for Brg and Fp calculated from the model. An initial refinement for a three-phase assemblage indicates that the Brg Al content can be fixed at 0.10 atoms pfu. Small amounts of Al in Fp and $CaSiO_3$ perovskite (Irifune, 1994) are neglected as are the concentrations of Cr, Na and Ti.

In previous experimental studies the apparent Fe-Mg distribution coefficient, K_D (app), i.e. where all Fe is assumed to be Fe^{2+}, between Brg and Fp is often reported (Irifune et al., 2010). Whether explicitly stated or not, K_D (app) is quite often employed because the $Fe^{3+}/\sum Fe$ ratios are rarely measured or used to determine the actual Fe^{2+}-Mg K_D. In Fig. 10 the model is used to calculate the $Fe^{3+}/\sum Fe$ ratio in both Brg and the whole pyrolite rock as well as K_D (app) between Brg and Fp. From experiments performed between 28 and 47.4 GPa, Irifune et al. (2010) reported a decrease in K_D (app) which they attributed to a possible iron spin transition in Fp. In fact as shown in Fig. 10, K_D (app) is a strong function of fo_2 and the entire range in values reported by Irifune et al. (2010), shown by the light blue shaded area in Fig. 10, can be achieved through changes in fo_2 between only IW and IW + 1.5. Such an fo_2 range would be quite consistent with the use of graphite capsules by Irifune et al. (2010) which would impose only a maximum possible fo_2 of approximately 2 log units above IW. As shown in section 4.4 the calculated trends are not expected to change strongly with pressure. There could of course be other reasons why K_D (app) was observed to change with pressure in the experiments, including a spin transition, however the calculations show that such experimental results are unconstrained unless fo_2 is fixed due to the strong variation in the Fe^{3+} content of Brg with fo_2. Variations in fo_2 can easily explain the significant discrepancies between K_D (app) measurements made in different DAC studies performed at deeper lower mantle conditions.

4.3 Metal saturation determination

As shown in Fig. 10, the $Fe^{3+}/\Sigma Fe$ ratio of the pyrolite whole rock is a function of fo_2 and even near IW, the ratio remains over 0.35. Upper mantle rocks have low $Fe^{3+}/\Sigma Fe$ ratios with values generally not exceeding 0.03 (Canil et al., 1994; Woodland et al., 2006). As pointed out by Frost et al. (2004), this implies that if the mantle has a relatively constant bulk oxygen content, then the lower mantle fo_2 would be driven to values where iron-nickel alloy would form. The oxygen released by this reduction satisfies the requirement of Brg for ferric iron at low oxygen fugacities. Ferric iron is therefore produced through the

reaction:

$$3\,\mathrm{FeO} = \mathrm{Fe_2O_3} + \mathrm{Fe} \qquad (35)$$
Fp Brg alloy

NiO in Brg and Fp would also reduce to form Fe-Ni alloy and provide oxygen to form ferric iron in Brg. Using a pyrolite bulk composition with an initially defined bulk $Fe^{3+}/\Sigma Fe$ ratio, the proportion of iron-nickel metal that would precipitate to provide sufficient ferric iron in Brg for the implied fo_2 can be calculated. This calculation uses the model described in section 4.1.3 combined with a pyrolite composition mass balance and a thermodynamic description for the reduction of NiO to Fe-Ni metal. In this calculation the fo_2 is fixed by the equilibria:

$$2\,\mathrm{Fe} + \mathrm{O_2} = 2\,\mathrm{FeO} \qquad (36)$$
alloy Fp

and

$$2\,\mathrm{Ni} + \mathrm{O_2} = 2\,\mathrm{NiO} \qquad (37)$$
alloy Fp

where the fo_2 for equilibrium (36) is determined from:

$$\log f_{\mathrm{O_2}} = \frac{\Delta G^0_{(36)}}{\mathrm{R}T\ln(10)} + 2\log\frac{x^{\mathrm{Fp}}_{\mathrm{FeO}}}{x^{\mathrm{alloy}}_{\mathrm{Fe}}} + 2\log\frac{\gamma^{\mathrm{Fp}}_{\mathrm{FeO}}}{\gamma^{\mathrm{alloy}}_{\mathrm{Fe}}} \qquad (38)$$

and a similar equation for equilibrium (37). ΔG^0 for both equilibria can be determined using the equations of Campbell et al. (2009). $\gamma^{\mathrm{Fp}}_{\mathrm{FeO}}$, the activity coefficient of FeO in Fp and $\gamma^{\mathrm{Fp}}_{\mathrm{NiO}}$ are determined using a ternary MgO-FeO-NiO symmetric Margules equation with the terms given in Table B.4. In order to obtain Ni partition coefficients between Fp and Fe-Ni alloy that are in agreement with the existing experimental data (Urakawa, 1991) ideal mixing in the Fe-Ni alloy had to be assumed. The alloy composition and the proportion of NiO in Fp are refined within the constraints of a mass balance such that both equilibria yield the same fo_2, but the total amount of alloy produced is controlled by the Brg Fe^{3+} and is calculated using equilibrium (35). The FeO concentration of Fp is controlled by equilibrium (36) and the Brg FeO content is constrained by the conditions of equilibrium for equilibria (26-28), which in turn depends on the fo_2 and the total Fe and Al in the bulk composition. A non-linear least-squares minimization routine is used to vary the proportions and compositions of the four phases – Brg, Fp, $CaSiO_3$ perovskite and Fe-Ni alloy, while maintaining mass balance and ensuring that the Gibbs energy of each of the described equilibria is equal

to zero. This also requires that the site occupancies of trivalent cations in Brg are also refined simultaneously.

The calculations show that even a high initial bulk $Fe^{3+}/\sum Fe$ ratio of 0.26, i.e., before Brg and metal formation, would still impose an fo_2 low enough for Fe metal precipitation at 25 GPa and 1973 K. As can be seen in Fig. 11, when the initial bulk rock $Fe^{3+}/\sum Fe$ ratio decreases from 0.26 to 0, the fo_2 buffered by coexisting Fe-Ni alloy and Fp only decreases slightly from IW - 0.71 to IW - 0.87. Moreover, the resulting bulk rock $Fe^{3+}/\sum Fe$ ratio after the formation of Fe-Ni alloy is 0.28 even for an initial bulk rock $Fe^{3+}/\sum Fe$ ratio before Brg formation of zero. Table B.3 shows the resulting calculated compositions of lower mantle phases for a pyrolite bulk composition with an initial bulk $Fe^{3+}/\Sigma Fe$ ratio of 0.03 i.e., similar to the value proposed for the upper mantle. The oxygen fugacity is IW - 0.86, which results in the formation of 0.67 wt. % Fe-Ni alloy containing approximately 23 wt. % Ni. The resulting $Fe^{3+}/\Sigma Fe$ ratio of Brg is 0.50 and the bulk pyrolite has a ratio of 0.28. Note that the iron content of Brg is lower than that reported in the experiments of Irifune (1994) and Irifune et al. (2010) because the fo_2 of these previous studies must have been higher, resulting in higher Brg $Fe^{3+}/\Sigma Fe$ ratios (Table B.3). Fig. 11 shows that similar calculations performed for a harzburgite composition (Irifune and Ringwood, 1987) result in lower amounts of metal precipitation due to the lower Al content in Brg.

4.4 Extrapolation to higher pressures

The volumes of Brg components used in the model described in section 4.1.3 can be determined using ambient pressure X-ray diffraction measurements of Brg volumes as a function of composition (Huang (2020). This allows the pressure dependencies of the equilibria employed in the model to be estimated. For equilibrium (28) for example the pressure dependence can be determined using the equation:

$$\Delta G^0_{(28)} + \int_{25}^{P} \Delta V^0 \mathrm{d}P = -\mathrm{R}T\ln \frac{\left(a^{\mathrm{Brg}}_{\mathrm{FeAlO_3}}\right)^2}{(a^{\mathrm{Fp}}_{\mathrm{FeO}})^2\, a^{\mathrm{Brg}}_{\mathrm{AlAlO_3}} \left(f_{\mathrm{O_2}}\right)^{1/2}} \qquad (39)$$

Similar equations can then be written for equilibrium (26) and (27). Volumes and equation of state data used to calculate the integrals are given in Table B.5. The formalism of modified Tait equation of state from Holland and Powell (2011) is employed. Two different assumptions concerning the equation of state terms for the Brg components are assumed, one where they are considered to be the same as $MgSiO_3$ Brg and the other where values for the bulk modulus of each component are estimated, as described in the

supplementary information A.4 and given in Table B.5. This provides some considerations of the likely uncertainties. The uncertainties arising from the equation of state estimates increase with pressure and for this reason the extrapolation is performed over a relatively small pressure range (25-50 GPa) to also exclude the possible effects of electronic spin transitions. In principle, deviations from the model at higher pressures for experiments where oxygen fugacities are well constrained could be used as evidence for the occurrence of a spin transition.

In order to test the reliability of the pressure dependent term in the model, we first use it to extrapolate the Al-Mg-Si-O system model (section 4.1.1) for which a comparison can be made with the high pressure experimental results of Liu et al. (2017). As can be seen from Fig. 12, which is calculated at the maximum in $MgAlO_{2.5}$ content that occurs at approximately 0.1 Al atoms pfu, the proportion of the OV component matches the experimental data very well, although the calculated trend simply arises from the negative change in standard molar volume for equilibrium (15), that has been determined independently using X-ray diffraction measurements (Huang, 2020). The calculation uses different assumptions for the bulk moduli, as previously described, to assess the likely error (Table B.5), however, even when these uncertainties are considered a decreasing trend with pressure is predicted, with the uncertainties mirroring those of the experimental data (Fig. 12).

In Fig. 13 Brg $Fe^{3+}/\Sigma Fe$ ratios are shown as a function of pressure calculated for a pyrolite composition at IW + 1.5 and in equilibrium with Fe-Ni metal. The results of several previous high-pressure studies are also shown with the Brg compositions indicated, when reported. For comparison with the work of Prescher et al. (2014) a composition with approximately half the amount of Al (0.055 atoms pfu) at IW - 0.5 is also calculated. Although the standard volume change for equilibrium (28) is not negative, when combined with the effect of pressure on the absolute fO_2, Brg $Fe^{3+}/\Sigma Fe$ ratios are predicted to increase slightly with pressure. This increase appears to flatten at higher pressures and would ultimately go through a maximum if extrapolated higher, an effect that may well be accentuated at higher pressures by the Fe^{2+} spin transition in Fp (e.g., Lin et al., 2005, 2007) (see Lin et al., 2013 for a review). The solid curves shown in Fig. 13 are calculated assuming that the bulk moduli for all Brg components are identical to the $MgSiO_3$ endmember. The uncertainties derived from the molar volume estimates and from using different bulk modulus assumptions, as discussed above (Table B.5), are also indicated by the shaded areas around each curve in Fig. 13. These uncertainties are smaller than 5 % even at 50 GPa.

Irifune et al. (2010), who studied a pyrolite composition, report two Brg $Fe^{3+}/\Sigma Fe$ ratios for each experiment with a lower value from Mössbauer spectroscopy and the higher value from electron energy loss spectroscopy measurements. Although the uncertainties are large, the values are at least consistent with an fO_2 close to Fe-Ni alloy equilibrium, which would be the minimum possible for this composition. Brg $Fe^{3+}/\Sigma Fe$ ratios reported by Stagno et al. (2011) are quite consistent with the calculations because the fO_2 is higher but the Brg Al content is lower than the pyrolite models.

The laser heated DAC results of Prescher et al. (2014) agree well with the model calculated for the same composition if an fO_2 of IW - 0.5 is assumed. Although Prescher et al. (2014) did not control or measure the fO_2 there is no reason to think it would change between the first two pressures, which are at least consistent with the pressure dependence of the model calculation. The slight decrease of $Fe^{3+}/\sum Fe$ at 40 GPa may even be consistent with the higher temperature (2120 K) employed at this condition. Higher Fe contents (0.21 atoms pfu) in the Brg samples of Kupenko et al. (2015) can also explain the slightly lower Brg $Fe^{3+}/\Sigma Fe$ ratios compared to the results of Prescher et al. (2014).

Shim et al. (2017) performed one of the only studies in the DAC where attempts were made to buffer the fO_2 using the presence of Fe metal. However, Fp was not present in the experiments, which instead contained a SiO_2 polymorph, at least in some samples, which would be stishovite (St) below 50 GPa. Some ideas of the expected pressure effect on the Brg ferric iron content of the assemblage can be obtained by considering the volume change of the equilibrium,

$$\underset{\text{Brg}}{3\ FeSiO_3} + \underset{\text{Brg}}{AlAlO_3} = \underset{\text{Brg}}{2\ FeAlO_3} + \underset{\text{metal}}{Fe} + \underset{\text{St}}{3\ SiO_2} \qquad (40)$$

This has a relatively large positive standard volume change of 1.1–1.7 cm^3/mol at 25 GPa, depending on the bulk modulus assumptions (Table B.5), implying that with pressure Brg should become less ferric iron rich, as is observed in the experiments. Although these results are not relevant to a pyrolite mantle composition, they may show how Brg ferric iron contents vary with pressure in compositions arising from subducted oceanic crust.

The Brg Al and Fe contents were not reported in the study of Andrault et al. (2018), so it is hard to make a comparison with the model calculations. However, given the low Brg $Fe^{3+}/\sum Fe$ ratios one would conclude that the Brg Al contents were also low, which is actually inconsistent with the reported presence of garnet in the lower pressure samples. This comparison with previous experimental studies, therefore, mainly

serves to underline the fact that control of factors such as fO_2, Brg Al and Fe contents and SiO_2 activity are essential if any meaningful and systematic information is to be gained on the evolution of Brg $Fe^{3+}/\Sigma Fe$ ratios with pressure. Without first monitoring these aspects of the experiments it is impossible to attribute any changes in Brg $Fe^{3+}/\Sigma Fe$ ratios to factors such as iron spin transitions.

Fe-Mg exchange coefficients, K_D (app), between Brg and Fp in a pyrolite composition have been calculated at different fO_2 conditions and for a constant Brg $Fe^{3+}/\Sigma Fe$ ratio of 0.69 and are shown in Fig. 14. The calculations are compared with experimental data from Irifune (1994) and Irifune et al. (2010). These experimental data show an initial increase in K_D (app) between 25 and 28 GPa that can be attributed to the transformation of garnet to Brg. This causes an increase in the Brg Al content, which is then coupled to an increase in the Fe^{3+} content of Brg. As stated above, the model calculations assume an assemblage which is already garnet free. The experimental data fall between the curve calculated for an fO_2 of IW + 1.5 and the curve calculated for a constant Brg $Fe^{3+}/\Sigma Fe$ ratio of 0.69, which is close to the upper bounds of the two measurements made by Irifune et al. (2010). From this comparison it appears that the experimental measurements do not conform to either a single fO_2 or a single Brg $Fe^{3+}/\Sigma Fe$ ratio but in fact span a range in fO_2 from approximately IW + 1.5 to IW - 0.6. As explained in section 4.2 the steep drop in K_D (app) above 40 GPa can be easily explained by a change in fO_2 between the experiments. It would be surprising if an Fe^{2+} spin transition in Fp could cause such a dramatic change in K_D (app) as proposed by Irifune et al. (2010) because the effects of the transition would be expected to occur over a much broader pressure interval (e.g., Lin et al., 2007; Mao et al., 2011; Sturhahn et al., 2005; Tsuchiya et al., 2006; Wentzcovitch et al., 2009). The two data points where $Fe^{3+}/\Sigma Fe$ ratios were actually measured by Irifune et al. (2010) and found to be similar, albeit with large uncertainties, are in reasonable agreement with the model in that the K_D (app) is predicted to decrease for a constant $Fe^{3+}/\Sigma Fe$ ratio. This decrease can be mainly attributed to the effect of pressure on the Fe^{2+}-Mg exchange shown by the curve for K_D in Fig. 14.

Fig. 15 shows the effect of pressure on the site occupancies in Brg for a pyrolite composition in equilibrium with Fe-Ni alloy. The Brg B site Al content decreases with pressure in response to the quite sharp decrease in the proportion of OV above ~ 32 GPa (Fig. 15b), which is consistent with previous experimental and theoretical studies in the Al-Mg-Si-O system (Brodholt, 2000; Liu et al., 2017). This in turn is driven by the negative volume changes of equilibria (26) and (27) and causes the proportion of A-site Al to increase. Pressure also increases slightly the Brg $Fe^{3+}/\sum Fe$ ratio, which raises the amount of Fe-Ni metal

743 that needs to precipitate by about 0.003 wt. % between 25 and 40 GPa, after which the increase levels off.
744 The slightly positive volume change of equilibrium (31) results in a very small increase in the amount of
745 Fe^{3+} on the Brg B site which increases from practically zero to 0.0005 atoms pfu between 25 and 50 GPa.
746 This increase is asymptotic, however, and at higher pressures it is quite plausible that more significant
747 concentrations are reached, as previously proposed (Kupenko et al., 2015).

748 **4.5 Implications for deep mantle diamond inclusions**

749 It has been proposed that some diamonds contain inclusions that were originally trapped as Brg in the
750 lower mantle (e.g., Brenker et al., 2002; Hutchison et al., 2001; Kaminsky, 2012; Kaminsky et al., 2001;
751 McCammon et al., 2004c; Stachel et al., 2000; Thomson et al., 2014). It is possible to place constraints on
752 the oxygen fugacities at which these diamonds formed, because although these inclusions may now have
753 back transformed to other minerals, they have preserved the relatively high $Fe^{3+}/\Sigma Fe$ ratios that are typical
754 of Brg. Knowledge of the fo_2 of formation provides information on the type of carbon-bearing agent from
755 which the diamonds were formed. As described in section 3.1 (and supplementary information A.1) if
756 diamonds formed from the reduction of carbonates, as frequently proposed (Brenker et al., 2007), then the
757 fo_2 recorded should have been approximately IW + 2, if this occurred at the top of the lower mantle.
758 McCammon et al. (1997) report $Fe^{3+}/\Sigma Fe$ ratios for two proposed Brg inclusions in diamonds from the
759 São Luiz River, Brazil. Using the model proposed in section 4.1.3 the oxygen fugacities recorded by these
760 inclusions can be determined assuming they formed at conditions compatible with the top of the lower
761 mantle, which has been proposed for at least some of the inclusions (McCammon et al., 2004a). One
762 inclusion (BZ251B) with 0.03 Al and 0.05 Fe atoms pfu has an $Fe^{3+}/\Sigma Fe$ ratio of 0.20 (6). The minimum fo_2
763 for such a composition, where it coexists with Fe-Ni alloy, is near IW - 0.8 and the minimum $Fe^{3+}/\Sigma Fe$ ratio
764 is determined to be 0.32, which is higher than observed but potentially still within the combined
765 uncertainties of the model and measurement. Considering the results of section 3.5, however, the lower
766 $Fe^{3+}/\Sigma Fe$ ratio of the inclusion with respect to the model prediction might actually imply that it formed at
767 slightly higher temperatures than 1973 K. Given this fo_2, however, it is unlikely that the diamond formed
768 from a carbonate bearing assemblage. A second inclusion (BZ210B) with 0.2 Al and 0.07 Fe atoms pfu has
769 an $Fe^{3+}/\Sigma Fe$ ratio of 0.75(3). The fo_2 calculated for this inclusion is IW + 0.7, which also falls below the
770 carbonate stability field (Fig. A.2). One further inclusion (KK-16 b; McCammon et al., 2004a; Stachel et al.,

771 2000) in a diamond from Kankan, Guinea, has an Al content of only 0.01 atoms pfu, which is too low to be
772 interpreted using the Al-bearing model but can be examined using the Al-free model from section 4.1.2.
773 The resulting fO_2 for this inclusion, which contains 0.05 total Fe atoms pfu and has a $Fe^{3+}/\Sigma Fe$ ratio of
774 0.09(25), is IW - 0.5, which is very close to equilibrium with Fe-Ni metal. However, given the large
775 uncertainty in the ferric iron content a value of IW + 3.0 can also be obtained from the upper bound.
776 Interestingly, in the same diamond there is also a Fp crystal with 0.14 Fe atoms pfu. If this inclusion were
777 in equilibrium with the Brg inclusion it would imply a Brg $Fe^{3+}/\Sigma Fe$ ratio closer to 0.25 and an fO_2 of
778 approximately IW + 1.5, which is close to carbonate stability field. This in fact points to another way that
779 the model could be employed to make an estimate of the fO_2 or Brg $Fe^{3+}/\Sigma Fe$ ratio based purely on the total
780 Fe contents measured for the Fp and Brg inclusions. The same diamond, however, also contains an
781 inclusion of $FeCO_3$ siderite, which could not have been in equilibrium with the Brg inclusion because as
782 shown in Table 3 equilibrium carbonates should have Fe/(Fe+Mg) ratios of approximately 0.01-0.03.

783 **5. Summary**

784 Experiments performed at 25 GPa and 1973 K–2373 K allow the relationship between fO_2 and Brg
785 $Fe^{3+}/\Sigma Fe$ ratio to be quantitatively described in terms of the Brg Al and total Fe contents in the presence of
786 Fp. Al-free data reveal a steep relationship between fO_2 and the Brg $Fe^{3+}/\Sigma Fe$ ratio. This relationship
787 becomes less steep with increasing Brg Al content, which also raises the Brg $Fe^{3+}/\Sigma Fe$ ratio at a constant
788 fO_2. There is a modest decrease in $Fe^{3+}/\Sigma Fe$ ratio with total Brg Fe content. Experiments from this and
789 previous studies performed at higher temperatures indicate that the Brg $Fe^{3+}/\Sigma Fe$ ratio decreases with
790 increasing temperature for the same fO_2 and composition.

791 In order to develop a thermodynamic model to describe this behavior we found it necessary to first
792 understand the speciation of Al, Fe^{3+} and OV in the Al-Mg-Si-O and Fe-Mg-Si-O sub-systems. For the Al-Mg-
793 Si-O system the variation in the OV proportion found in previous experiments coexisting with MgO could
794 be fitted using equilibrium (15) that employs $MgSi_{7/8}Al_{1/8}O_{15/16}O_2$ as the OV component, i.e., an
795 endmember much closer to the actual composition found to contain the most OV. The resulting model has
796 only two adjustable parameters, the ΔG^0 for equilibrium (15) and a parameter describing non-ideal
797 interaction between Si and Al on the Brg B-site. This model can be extended to higher pressures using
798 component molar volumes determined from X-ray diffraction data at ambient conditions. This model

reproduces the decrease in OV speciation with pressure, found in a recent experimental study (Liu et al., 2017) very well, giving confidence to the methodology.

To fit the experiments in the Fe-Mg-Si-O system a similar OV component equilibrium, (20), is employed and a further equilibrium, (24), is required to determine the fO_2 dependence. The maximum proportion of OV is found to be approximately half that in the Al-Mg-Si-O system and the resulting uncertainties in their proportion are very high. In the fitting procedure site occupancies for Fe^{3+} are left as adjustable parameters as the experimental data are not sufficiently accurate to provide constraints. The resulting model is in reasonable agreement with the experimental data but does not reproduce the curvature in the fO_2-Brg $Fe^{3+}/\Sigma Fe$ relationship particularly well, even when activity-composition relations are included. To significantly improve this fit, however, would require a higher level of accuracy in OV determination and more data coverage to justify more complexity in the underlying model. One possibility would be to obtain data at higher temperatures where the proportion of OV may be higher (Liu et al., 2019a) and the trends can be obtained more accurately.

Experiments in the Fe-Al-Mg-Si-O system are fitted using three equilibria (26–28) to describe the speciation of Brg components plus one to describe the Fe^{2+}-Mg exchange between Brg and Fp. Aside from Mg-Fe^{2+}, mixing in Brg is assumed to be ideal and trivalent cation site occupancies are also refined in the model. The resulting model fits the experimental data and the proposed site occupancies very well, especially considering that there are only three ΔG^0 fitting parameters. The results show that the apparent Fe-Mg distribution coefficient K_D (app) between Brg and Fp (i.e., that assumes all Fe is Fe^{2+}) is a strong function of fO_2. Changes in K_D (app) reported in high pressure experiments (e.g. Irifune et al., 2010) can easily be explained by relatively small changes in the experimental fO_2, which is rarely buffered, rather than changes in the iron spin state.

For a pyrolite composition with an initial $Fe^{3+}/\Sigma Fe$ ratio of 0.03 before Brg formation, as in the upper mantle, the fO_2 at the top of the lower mantle would be IW - 0.86, which would force the formation of 0.7 wt. % Fe-Ni alloy containing approximately 23 wt. % Ni. The resulting $Fe^{3+}/\Sigma Fe$ ratio of Brg is 0.5 and the bulk pyrolite has a $Fe^{3+}/\Sigma Fe$ ratio of 0.28. Using partial molar volumes determined for the different Brg trivalent cation components and equation of state estimates, mineral compositions within a pyrolite bulk composition can be calculated up to 50 GPa. The Brg $Fe^{3+}/\Sigma Fe$ ratio either in equilibrium with Fe-Ni metal or at a fixed fO_2 is predicted to rise initially but flattens by 50 GPa. Some agreements can be found with the

results of some previous laser heated DAC experiments if assumptions are made concerning the fO_2 at which they were performed. It is important to emphasize, however, that the Brg $Fe^{3+}/\Sigma Fe$ ratio and the exchange of total Fe and Mg with Fp are strongly dependent on fO_2, in addition to the Brg Al and total Fe contents. The pressure dependence of the Brg $Fe^{3+}/\Sigma Fe$ ratio is most likely also dependent on the nature of coexisting phases. These factors need to be constrained before further effects such as those that might result from Fe spin transitions can be explored.

The OV content in Fe and Al-bearing Brg in a pyrolite composition in equilibrium with Fe-Ni metal, is predicted to decrease continuously from 25 to 40 GPa, reaching almost zero at ~ 40 GPa. This decrease may influence transport properties in the top portion of the lower mantle. Although there is a clear preference of Fe^{3+} for the Brg A-site, when $Al \approx Fe^{3+}$, with increasing pressure a small increase is predicted in the B-site Fe^{3+} occupancy, which may become more significant above 50 GPa.

The thermodynamic models can also be used to investigate the fO_2 recorded by inclusions in diamonds that are proposed to have formed as Brg in the lower mantle, although currently there are very few samples for which $Fe^{3+}/\Sigma Fe$ measurements exist. Two proposed Al-bearing Brg inclusions from the São Luiz River, Brazil reveal oxygen fugacities that are within the range IW $\pm$ 1, which would seem to preclude their formation directly from carbonates derived from subducting slabs. The uncertainty in the $Fe^{3+}/\Sigma Fe$ ratio from one inclusion from Kankan, Guinea, on the other hand, translates to an fO_2 range that potentially overlaps with the pure carbonate stability field. Such considerations potentially combined with information on the diamond ^{13}C content or inclusion trace element content, may well lead to a better understanding of deep diamond formation.

ACKNOWLEDGEMENTS

We would like to thank H. Fischer for the machining of multi-anvil assembly parts, R. Njul for sample preparation and D. Krauße and A. Potzel for assistance with EPMA analysis. We are also very grateful for the constructive comments of two anonymous reviewers and the associate editor. This work was supported by DFG grant FR1555/11. The Titan G2 TEM and Scios FIB at BGI were financed by a DFG grant No. INST 91/315-1 FUGG and INST 91/251-1 FUGG, respectively.

References:

Andrault D., Bolfan-Casanova, N., Bouhifd, M.A., Guignot, N. and Kawamoto, T. (2007) The role of Al-defects on the equation of state of Al–(Mg,Fe)SiO_3 perovskite. *Earth Planet. Sci. Lett.* **263**, 167-179.

Andrault D., Bolfan-Casanova, N. and Guignot, N. (2001) Equation of state of lower mantle (Al,Fe)-$MgSiO_3$ perovskite. *Earth Planet. Sci. Lett.* **193**, 501-508.

Andrault D., Muñoz, M., Pesce, G., Cerantola, V., Chumakov, A., Kantor, I., Pascarelli, S., Rüffer, R. and Hennet, L. (2018) Large oxygen excess in the primitive mantle could be the source of the Great Oxygenation Event. *Geochem. Perspect. Lett.*, 5-10.

Andrault D., Neuville, D.R., Flank, A.-M. and Wang, Y. (1998) Cation sites in Al-rich $MgSiO_3$ perovskites. *Am. Mineral.* **83**, 1045-1053.

Armstrong K., Siersch, N.C., Boffa-Ballaran, T., Frost, D.J., Yu, T. and Wang, Y. (2020) Equations of state, phase relations, and oxygen fugacity of the Ru-RuO_2 buffer at high pressures and temperatures. *Am. Mineral.* **105**, 333-343.

Auzende A.L., Badro, J., Ryerson, F.J., Weber, P.K., Fallon, S.J., Addad, A., Siebert, J. and Fiquet, G. (2008) Element partitioning between magnesium silicate perovskite and ferropericlase: New insights into bulk lower-mantle geochemistry. *Earth Planet. Sci. Lett.* **269**, 164-174.

Bina C.R. and Helffrich, G. (2014) Geophysical Constraints on Mantle Composition, in: Carlson, R.W. (Ed.), The Mantle and Core: Treatise on Geochemistry, Vol. 3. Elsevier–Pergamon, Oxford, pp. 41-65.

Boujibar A., Bolfan-Casanova, N., Andrault, D., Bouhifd, M.A. and Trcera, N. (2016) Incorporation of Fe^{2+} and Fe^{3+} in bridgmanite during magma ocean crystallization. *Am. Mineral.* **101**, 1560-1570.

Brenker F.E., Stachel, T. and Harris, J.W. (2002) Exhumation of lower mantle inclusions in diamond: ATEM investigation of retrograde phase transitions, reactions and exsolution. *Earth Planet. Sci. Lett.* **198**, 1-9.

Brenker F.E., Vollmer, C., Vincze, L., Vekemans, B., Szymanski, A., Janssens, K., Szaloki, I., Nasdala, L., Joswig, W. and Kaminsky, F. (2007) Carbonates from the lower part of transition zone or even the lower mantle. *Earth Planet. Sci. Lett.* **260**, 1-9.

Brodholt J.P. (2000) Pressure-induced changes in the compression mechanism of aluminous perovskite in the Earth's mantle. *Nature* **407**, 620-622.

Campbell A.J., Danielson, L., Righter, K., Seagle, C.T., Wang, Y. and Prakapenka, V.B. (2009) High pressure effects on the iron–iron oxide and nickel–nickel oxide oxygen fugacity buffers. *Earth Planet. Sci. Lett.* **286**, 556-564.

Campbell A.J., Danielson, L., Righter, K., Wang, Y., Davidson, G. and Wang, Y. (2006) Oxygen fugacity at high pressure: Equations of state of metal-oxide pairs. *Lunar Planet. Sci. XXXVII.*, Lunar Planet. Inst., Houston. #1977 (abstr.).

Canil D., O'Neill, H.S.C., Pearson, D., Rudnick, R.L., McDonough, W.F. and Carswell, D. (1994) Ferric iron in peridotites and mantle oxidation states. *Earth Planet. Sci. Lett.* **123**, 205-220.

Catalli K., Shim, S.-H., Dera, P., Prakapenka, V.B., Zhao, J., Sturhahn, W., Chow, P., Xiao, Y., Cynn, H. and Evans, W.J. (2011) Effects of the Fe^{3+} spin transition on the properties of aluminous perovskite—New insights for lower-mantle seismic heterogeneities. *Earth Planet. Sci. Lett.* **310**, 293-302.

Catalli K., Shim, S.-H., Prakapenka, V.B., Zhao, J., Sturhahn, W., Chow, P., Xiao, Y., Liu, H., Cynn, H. and Evans, W.J. (2010) Spin state of ferric iron in $MgSiO_3$ perovskite and its effect on elastic properties. *Earth Planet. Sci. Lett.* **289**, 68-75.

Fei H., Liu, Z., McCammon, C. and Katsura, T. (2020) Oxygen vacancy substitution linked to ferric Iron in bridgmanite at 27 GPa. *Geophys. Res. Lett.* **47**.

Fei Y., Virgo, D., Mysen, B., Wang, Y. and Mao, H. (1994) Temperature-dependent electron delocalization in (Mg, Fe)SiO_3 perovskite. *Am. Mineral.* **79**, 826-837.

Frost D.J. (2003) Fe^{2+}-Mg partitioning between garnet, magnesiowüstite, and $(Mg,Fe)_2SiO_4$ phases of the transition zone. *Am. Mineral.* **88**, 387-397.

Frost D.J. and Langenhorst, F. (2002) The effect of Al_2O_3 on Fe–Mg partitioning between magnesiowüstite and magnesium silicate perovskite. *Earth Planet. Sci. Lett.* **199**, 227-241.

Frost D.J., Liebske, C., Langenhorst, F., McCammon, C.A., Trønnes, R.G. and Rubie, D.C. (2004) Experimental evidence for the existence of iron-rich metal in the Earth's lower mantle. *Nature* **428**, 409-412.

Glazyrin K., Boffa Ballaran, T., Frost, D.J., McCammon, C.A., Kantor, A., Merlini, M., Hanfland, M. and Dubrovinsky, L. (2014) Magnesium silicate perovskite and effect of iron oxidation state on its bulk sound velocity at the conditions of the lower mantle. *Earth Planet. Sci. Lett.* **393**, 182-186.

Goncharov A., Struzhkin, V., Montoya, J., Kharlamova, S., Kundargi, R., Siebert, J., Badro, J., Antonangeli, D., Ryerson, F. and Mao, W. (2010) Effect of composition, structure, and spin state on the thermal conductivity of the Earth's lower mantle. *Phys. Earth Planet. Inter.* **180**, 148-153.

Goncharov A.F., Beck, P., Struzhkin, V.V., Haugen, B.D. and Jacobsen, S.D. (2009) Thermal conductivity of lower-mantle minerals. *Phys. Earth Planet. Inter.* **174**, 24-32.

Grüninger H., Liu, Z., Siegel, R., Boffa Ballaran, T., Katsura, T., Senker, J. and Frost, D.J. (2019) Oxygen vacancy ordering in aluminous bridgmanite in the Earth's lower mantle. *Geophys. Res. Lett.* **46**, 8731-8740.

Holland T.J.B. and Powell, R. (2011) An improved and extended internally consistent thermodynamic dataset for phases of petrological interest, involving a new equation of state for solids. *J. Metamorph. Geol.* **29**, 333-383.

Holzapfel C., Rubie, D.C., Frost, D.J. and Langenhorst, F. (2005) Fe-Mg interdiffusion in (Mg, Fe)SiO_3 perovskite and lower mantle reequilibration. *Science* **309**, 1707-1710.

Hsu H., Blaha, P., Cococcioni, M. and Wentzcovitch, R.M. (2011) Spin-state crossover and hyperfine interactions of ferric iron in $MgSiO_3$ perovskite. *Phys. Rev. Lett.* **106**, 118501.

Huang R. (2020) Bridgmanite crystal chemistry and iron content in the Earth's lower mantle. Ph. D. thesis, Universität Bayreuth, https://epub.uni-bayreuth.de/4611/.

Hummer D.R. and Fei, Y. (2012) Synthesis and crystal chemistry of Fe^{3+}-bearing $(Mg,Fe^{3+})(Si,Fe^{3+})O_3$ perovskite. *Am. Mineral.* **97**, 1915-1921.

Hutchison M.T., Hursthouse, M.B. and Light, M.E. (2001) Mineral inclusions in diamonds: associations and chemical distinctions around the 670-km discontinuity. *Contrib. Mineral. Petrol.* **142**, 119-126.

Irifune T. (1994) Absence of an aluminous phase in the upper part of the Earth's lower mantle. *Nature* **370**, 131–133.

Irifune T. and Ringwood, A.E. (1987) Phase transformations in a harzburgite composition to 26 GPa: implications for dynamical behaviour of the subducting slab. *Earth Planet. Sci. Lett.* **86**, 365-376.

Irifune T., Shinmei, T., McCammon, C.A., Miyajima, N., Rubie, D.C. and Frost, D.J. (2010) Iron partitioning and density changes of pyrolite in Earth's lower mantle. *Science* **327**, 193-195.

Jackson J.M., Sturhahn, W., Shen, G., Zhao, J., Hu, M.Y., Errandonea, D., Bass, J.D. and Fei, Y. (2005) A synchrotron Mössbauer spectroscopy study of (Mg,Fe)SiO_3 perovskite up to 120 GPa. *Am. Mineral.* **90**, 199-205.

Kaminsky F. (2012) Mineralogy of the lower mantle: A review of 'super-deep' mineral inclusions in diamond. *Earth Sci. Rev.* **110**, 127-147.

Kaminsky F.V., Ryabchikov, I.D., McCammon, C.A., Longo, M., Abakumov, A.M., Turner, S. and Heidari, H. (2015) Oxidation potential in the Earth's lower mantle as recorded by ferropericlase inclusions in diamond. *Earth Planet. Sci. Lett.* **417**, 49-56.

Kaminsky F.V., Zakharchenko, O.D., Davies, R., Griffin, W.L., Khachatryan-Blinova, G.K. and Shiryaev, A.A. (2001) Superdeep diamonds from the Juina area, Mato Grosso State, Brazil. *Contrib. Mineral. Petrol.* **140**, 734-753.

Keppler H., Dubrovinsky, L.S., Narygina, O. and Kantor, I. (2008) Optical absorption and radiative thermal conductivity of silicate perovskite to 125 gigapascals. *Science* **322**, 1529-1532.

Kessel R., Beckett, J.R. and Stolper, E.M. (2001) Thermodynamic properties of the Pt-Fe system. *Am. Mineral.* **86**, 1003-1014.

Kobayashi Y., Kondo, T., Ohtani, E., Hirao, N., Miyajima, N., Yagi, T., Nagase, T. and Kikegawa, T. (2005) Fe-Mg partitioning between (Mg, Fe)SiO_3 post-perovskite, perovskite, and magnesiowüstite in the Earth's lower mantle. *Geophys. Res. Lett.* **32**, L19301.

Kojitani H., Katsura, T. and Akaogi, M. (2007) Aluminum substitution mechanisms in perovskite-type $MgSiO_3$: an investigation by Rietveld analysis. *Phys. Chem. Miner.* **34**, 257-267.

Kröger F.A. and Vink, H.J. (1956) Relations between the concentrations of imperfections in crystalline solids. *Solid State Phys.* **3**, 307-435.

Kupenko I., McCammon, C.A., Sinmyo, R., Cerantola, V., Potapkin, V., Chumakov, A., Kantor, A., Rüffer, R. and Dubrovinsky, L. (2015) Oxidation state of the lower mantle: In situ observations of the iron electronic configuration in bridgmanite at extreme conditions. *Earth Planet. Sci. Lett.* **423**, 78-86.

Lauterbach S., McCammon, C., Van Aken, P., Langenhorst, F. and Seifert, F. (2000) Mössbauer and ELNES spectroscopy of (Mg,Fe)(Si,Al)O_3 perovskite: a highly oxidised component of the lower mantle. *Contrib. Mineral. Petrol.* **138**, 17-26.

Li J., Sturhahn, W., Jackson, J., Struzhkin, V., Lin, J., Zhao, J., Mao, H. and Shen, G. (2006) Pressure effect on the electronic structure of iron in (Mg,Fe)(Si,Al)O_3 perovskite: a combined synchrotron Mössbauer and X-ray emission spectroscopy study up to 100 GPa. *Phys. Chem. Miner.* **33**, 575-585.

Lin J.-F., Alp, E.E., Mao, Z., Inoue, T., McCammon, C.A., Xiao, Y., Chow, P. and Zhao, J. (2012) Electronic spin states of ferric and ferrous iron in the lower-mantle silicate perovskite. *Am. Mineral.* **97**, 592-597.

Lin J.-F., Mao, Z., Yang, J., Liu, J., Xiao, Y., Chow, P. and Okuchi, T. (2016) High-spin Fe^{2+} and Fe^{3+} in single-crystal aluminous bridgmanite in the lower mantle. *Geophys. Res. Lett.* **43**, 6952-6959.

Lin J.-F., Speziale, S., Mao, Z. and Marquardt, H. (2013) Effects of the electronic spin transitions of iron in lower mantle minerals: implications for deep mantle geophysics and geochemistry. *Rev. Geophys.* **51**, 244-275.

Lin J.-F., Struzhkin, V.V., Jacobsen, S.D., Hu, M.Y., Chow, P., Kung, J., Liu, H.Z., Mao, H.K. and Hemley, R.J. (2005) Spin transition of iron in magnesiowustite in the Earth's lower mantle. *Nature* **436**, 377-380.

Lin J.-F., Vanko, G., Jacobsen, S.D., Iota, V., Struzhkin, V.V., Prakapenka, V.B., Kuznetsov, A. and Yoo, C.S. (2007) Spin transition zone in Earth's lower mantle. *Science* **317**, 1740-1743.

Liu Z., Akaogi, M. and Katsura, T. (2019a) Increase of the oxygen vacancy component in bridgmanite with temperature. *Earth Planet. Sci. Lett.* **505**, 141-151.

Liu Z., Ballaran, T.B., Huang, R., Frost, D.J. and Katsura, T. (2019b) Strong correlation of oxygen vacancies in bridgmanite with Mg/Si ratio. *Earth Planet. Sci. Lett.* **523**, 115697.

Liu Z., Ishii, T. and Katsura, T. (2017) Rapid decrease of $MgAlO_{2.5}$ component in bridgmanite with pressure. *Geochem. Perspect. Lett.*, 12-18.

Manthilake G.M., de Koker, N., Frost, D.J. and McCammon, C.A. (2011) Lattice thermal conductivity of lower mantle minerals and heat flux from Earth's core. *Proc. Natl. Acad. Sci. U.S.A.* **108**, 17901-17904.

Mao H. (1997) Multivariable Dependence of Fe-Mg Partitioning in the lower mantle. *Science* **278**, 2098-2100.

Mao Z., Lin, J.-F., Liu, J. and Prakapenka, V.B. (2011) Thermal equation of state of lower-mantle ferropericlase across the spin crossover. *Geophys. Res. Lett.* **38**, L23308.

Mao Z., Wang, F., Lin, J.-F., Fu, S., Yang, J., Wu, X., Okuchi, T., Tomioka, N., Prakapenka, V.B., Xiao, Y. and Chow, P. (2017) Equation of state and hyperfine parameters of high-spin bridgmanite in the Earth's lower mantle by synchrotron X-ray diffraction and Mössbauer spectroscopy. *Am. Mineral.* **102**, 357-368.

Mattern E., Matas, J., Ricard, Y. and Bass, J. (2005) Lower mantle composition and temperature from mineral physics and thermodynamic modelling. *Geophys. J. Int.* **160**, 973-990.

McCammon C.A. (1997) Perovskite as a possible sink for ferric iron in the lower mantle. *Nature* **387**, 694-696.

McCammon C.A. (1998) The crystal chemistry of ferric iron in $Fe_{0.05}Mg_{0.95}SiO_3$ perovskite as determined by Mössbauer spectroscopy in the temperature range 80–293 K. *Phys. Chem. Miner.* **25**, 292-300.

McCammon C.A., Frost, D., Smyth, J., Laustsen, H., Kawamoto, T., Ross, N. and Van Aken, P. (2004a) Oxidation state of iron in hydrous mantle phases: implications for subduction and mantle oxygen fugacity. *Phys. Earth Planet. Inter.* **143**, 157-169.

McCammon C.A., Glazyrin, K., Kantor, A., Kantor, I., Kupenko, I., Narygina, O., Potapkin, V., Prescher, C., Sinmyo, R., Chumakov, A., Rüffer, R., Sergueev, I., Smirnov, G. and Dubrovinsky, L. (2013) Iron spin state in silicate perovskite at conditions of the Earth's deep interior. *High Press. Res.* **33**, 663-672.

McCammon C.A., Hutchison, M. and Harris, J. (1997) Ferric iron content of mineral inclusions in diamonds from Sao Luiz: a view into the lower mantle. *Science* **278**, 434-436.

McCammon C.A., Lauterbach, S., Seifert, F., Langenhorst, F. and Van Aken, P. (2004b) Iron oxidation state in lower mantle mineral assemblages: I. Empirical relations derived from high-pressure experiments. *Earth Planet. Sci. Lett.* **222**, 435-449.

McCammon C.A., Rubie, D., Ross, C., Seifert, F. and O'Neill, H.S.C. (1992) Mössbauer spectra of $^{57}Fe_{0.05}Mg_{0.95}SiO_3$ perovskite at 80 and 298 K. *Am. Mineral.* **77**, 894-897.

McCammon C.A., Stachel, T. and Harris, J. (2004c) Iron oxidation state in lower mantle mineral assemblages: II. Inclusions in diamonds from Kankan, Guinea. *Earth Planet. Sci. Lett.* **222**, 423-434.

Myhill R., Ojwang, D.O., Ziberna, L., Frost, D.J., Boffa Ballaran, T. and Miyajima, N. (2016) On the *P–T–f*O_2 stability of Fe_4O_5, Fe_5O_6 and Fe_4O_5-rich solid solutions. *Contrib. Mineral. Petrol.* **171**, 51.

Nakajima Y., Frost, D.J. and Rubie, D.C. (2012) Ferrous iron partitioning between magnesium silicate perovskite and ferropericlase and the composition of perovskite in the Earth's lower mantle. *J. Geophys. Res.: Solid Earth* **117**, B08201.

Narygina O.V., Kantor, I.Y., McCammon, C.A. and Dubrovinsky, L. (2010) Electronic state of Fe^{2+} in $(Mg,Fe)(Si,Al)O_3$ perovskite and $(Mg,Fe)SiO_3$ majorite at pressures up to 81 GPa and temperatures up to 800 K. *Phys. Chem. Miner.* **37**, 407-415.

Navrotsky A., Schoenitz, M., Kojitani, H., Xu, H., Zhang, J., Weidner, D.J. and Jeanloz, R. (2003) Aluminum in magnesium silicate perovskite: Formation, structure, and energetics of magnesium-rich defect solid solutions. *J. Geophys. Res.: Solid Earth* **108**, 2330.

Okuda Y., Ohta, K., Sinmyo, R., Hirose, K., Yagi, T. and Ohishi, Y. (2019) Effect of spin transition of iron on the thermal conductivity of (Fe,Al)-bearing bridgmanite. *Earth Planet. Sci. Lett.* **520**, 188-198.

Piet H., Badro, J., Nabiei, F., Dennenwaldt, T., Shim, S.-H., Cantoni, M., Hébert, C. and Gillet, P. (2016) Spin and valence dependence of iron partitioning in Earth's deep mantle. *Proc. Natl. Acad. Sci. U.S.A.* **113**, 11127-11130.

Pownceby M.I. and O'Neill, H.S.C. (1994) Thermodynamic data from redox reactions at high temperatures. IV. Calibration of the Re-ReO_2 oxygen buffer from EMF and NiO + Ni-Pd redox sensor measurements. *Contrib. Mineral. Petrol.* **118**, 130-137.

Prescher C., Langenhorst, F., Dubrovinsky, L.S., Prakapenka, V.B. and Miyajima, N. (2014) The effect of Fe spin crossovers on its partitioning behavior and oxidation state in a pyrolitic Earth's lower mantle system. *Earth Planet. Sci. Lett.* **399**, 86-91.

Prescher C., McCammon, C.A. and Dubrovinsky, L. (2012) MossA: a program for analyzing energy-domain Mössbauer spectra from conventional and synchrotron sources. *J. Appl. Crystallogr.* **45**, 329-331.

Saikia A., Ballaran, T.B. and Frost, D.J. (2009) The effect of Fe and Al substitution on the compressibility of $MgSiO_3$-perovskite determined through single-crystal X-ray diffraction. *Phys. Earth Planet. Inter.* **173**, 153-161.

Sakai T., Ohtani, E., Terasaki, H., Sawada, N., Kobayashi, Y., Miyahara, M., Nishijima, M., Hirao, N., Ohishi, Y. and Kikegawa, T. (2009) Fe-Mg partitioning between perovskite and ferropericlase in the lower mantle. *Am. Mineral.* **94**, 921-925.

Shim S.-H., Grocholski, B., Ye, Y., Alp, E.E., Xu, S., Morgan, D., Meng, Y. and Prakapenka, V.B. (2017) Stability of ferrous-iron-rich bridgmanite under reducing midmantle conditions. *Proc. Natl. Acad. Sci. U.S.A.* **114**, 6468-6473.

Sinmyo R. and Hirose, K. (2013) Iron partitioning in pyrolitic lower mantle. *Phys. Chem. Miner.* **40**, 107-113.

Sinmyo R., Hirose, K., Muto, S., Ohishi, Y. and Yasuhara, A. (2011) The valence state and partitioning of iron in the Earth's lowermost mantle. *J. Geophys. Res.: Solid Earth* **116**, B07205.

Sinmyo R., Hirose, K., Nishio-Hamane, D., Seto, Y., Fujino, K., Sata, N. and Ohishi, Y. (2008) Partitioning of iron between perovskite/postperovskite and ferropericlase in the lower mantle. *J. Geophys. Res.: Solid Earth* **113**, B11204.

Stachel T., Harris, J.W., Brey, G.P. and Joswig, W. (2000) Kankan diamonds (Guinea) II: lower mantle inclusion parageneses. *Contrib. Mineral. Petrol.* **140**, 16-27.

Stagno V. and Frost, D.J. (2010) Carbon speciation in the asthenosphere: Experimental measurements of the redox conditions at which carbonate-bearing melts coexist with graphite or diamond in peridotite assemblages. *Earth Planet. Sci. Lett.* **300**, 72-84.

Stagno V., Tange, Y., Miyajima, N., McCammon, C., Irifune, T. and Frost, D. (2011) The stability of magnesite in the transition zone and the lower mantle as function of oxygen fugacity. *Geophys. Res. Lett.* **38**, L19309.

Sturhahn W., Jackson, J.M. and Lin, J.F. (2005) The spin state of iron in minerals of Earth's lower mantle. *Geophys. Res. Lett.* **32**, L12307.

Thomson A.R., Kohn, S.C., Bulanova, G.P., Smith, C.B., Araujo, D., EIMF and Walter, M.J. (2014) Origin of sub-lithospheric diamonds from the Juina-5 kimberlite (Brazil): constraints from carbon isotopes and inclusion compositions. *Contrib. Mineral. Petrol.* **168**, 1081.

Tsuchiya T., Wentzcovitch, R.M., da Silva, C.R.S. and de Gironcoli, S. (2006) Spin transition in magnesiowustite in Earth's lower mantle. *Phys. Rev. Lett.* **96**, 198501.

Urakawa S. (1991) Partitioning of Ni between magnesiowüstite and metal at high pressure: implications for core-mantle equilibrium. *Earth Planet. Sci. Lett.* **105**, 293-313.

Walter M.J., Kohn, S.C., Araujo, D., Bulanova, G.P., Smith, C.B., Gaillou, E., Wang, J., Steele, A. and Shirey, S.B. (2011) Deep mantle cycling of oceanic crust: evidence from diamonds and their mineral inclusions. *Science* **334**, 54-57.

Walter M.J., Kubo, A., Yoshino, T., Brodholt, J., Koga, K.T. and Ohishi, Y. (2004) Phase relations and equation-of-state of aluminous Mg-silicate perovskite and implications for Earth's lower mantle. *Earth Planet. Sci. Lett.* **222**, 501-516.

Wentzcovitch R.M., Justo, J.F., Wu, Z., da Silva, C.R.S., Yuen, D.A. and Kohlstedt, D. (2009) Anomalous compressibility of ferropericlase throughout the iron spin cross-over. *Proc. Natl. Acad. Sci. U.S.A.* **106**, 8447-8452.

Woodland A.B., Kornprobst, J. and Tabit, A. (2006) Ferric iron in orogenic lherzolite massifs and controls of oxygen fugacity in the upper mantle. *Lithos* **89**, 222-241.

Woodland A.B. and O'Neill, H.S.C. (1997) Thermodynamic data for Fe-bearing phases obtained using noble metal alloys as redox sensors. *Geochim. Cosmochim. Acta* **61**, 4359-4366.

Xu Y., McCammon, C.A. and Poe, B.T. (1998) The effect of alumina on the electrical conductivity of silicate perovskite. *Science* **282**, 922-924.

Figure captions

Fig. 1 Back-scattered electron images of experimental run products obtained using different oxygen buffers: (a) Run H4746: a low oxygen fugacity was obtained using dispersed Fe metal. (b) Run S6921: Hematite was added and reduced in the experiment to form $(Mg,Fe)_2Fe_2O_5$. Magnesite also formed from carbon contaminants. (c) Run S7251: The oxygen fugacity was buffered by coexisting Re and ReO_2. (d) Run S6952: High oxygen fugacity was buffered by the coexistence of Ru and RuO_2. In all the experiments, the buffer materials were well dispersed throughout the sample to minimize the diffusion pathways. Abbreviations: Brg, bridgmanite; Fp, ferropericlase; Mst, magnesite.

Fig. 2 Representative room-temperature Mössbauer spectra of run products: (a) S7122 (Brg + Fp + Fe + carbide); (b) H4755 (Brg + Fp + Fe + carbide); (c) S6952 (Brg + Fp); (d) Hyperfine parameters of Brg from Mössbauer spectra collected at ambient conditions. In (a)–(c), the doublets correspond to Fe^{3+} (yellow) in Brg, Fe^{2+} in Brg (blue), and Fe^{2+} in Fp (light grey) and the magnetic sextets correspond to Fe metal (black) and Fe^0 in carbide (dark grey). In (d), solid red and blue circles indicate the parameters of Fe^{2+} on the A site and Fe^{3+} in Brg obtained from this study, respectively. Open red, pink and blue circles indicate the Brg $^{[A]}Fe^{2+}$, Fe^{n+}, and Fe^{3+} parameters from previous studies of Fei et al. (1994); Jackson et al. (2005); Lauterbach et al. (2000); Li et al. (2006); McCammon (1997, 1998); McCammon et al. (2004b); McCammon et al. (1992) and Narygina et al. (2010). Fe^{n+} absorption represents electron transfer between Fe^{2+} and Fe^{3+} in Brg and cannot be resolved in spectra of this study due to its peak overlapping with Fp. The blue triangle and diamond represent the parameters of Fe^{3+} on the A site and B site in Brg proposed by Hummer and Fei (2012).

Fig. 3 (a) The variation of the Si content of Brg with Al content at 25–27 GPa and 1873–2000 K. The two solid lines are expected trend lines for CC substitution along the $MgSiO_3$-$AlAlO_3$ join and the OV substitution along the $MgSiO_3$-$MgAlO_{2.5}$ join respectively. The orange symbols indicate Brg samples formed from starting compositions with Mg > Si and the green symbols indicate starting bulk composition with Mg $\leqslant$ Si. Data are taken from Grüninger et al. (2019); Kojitani et al. (2007); Liu et al. (2017); Liu et al. (2019a); (2019b) and Navrotsky et al. (2003). (b) Symbols show the mole fractions of the $MgAlO_{2.5}$ and $AlAlO_3$ Brg components as a function of Al content from experiments at 27 GPa and 2000 K that had starting compositions with Mg > Si. Data are from the same sources as in (a). The curves are calculated using different sets of thermodynamic

fitting parameters (see section 4.1.1) as indicated.

Fig. 4 (a) The variation of the Si content of Brg with the Fe^{3+} content at 25–27 GPa and 1923–2073 K. The solid lines indicate the CC $(Mg,Fe)SiO_3$-$Fe^{3+}Fe^{3+}O_3$ join and the OV $(Mg,Fe)SiO_3$-$(Mg,Fe)Fe^{3+}O_{2.5}$ join. The solid orange diamonds and the open orange diamonds indicate data from the current study and from previous studies (Fei et al., 2020; Frost and Langenhorst, 2002; McCammon et al., 2004b) respectively, where Brg coexisted with Fp. The open green diamonds are data from Hummer and Fei (2012) and Lauterbach et al. (2000) where Brg is not in equilibrium with Fp. (b) The mole fraction of $FeFeO_3$ and $(Mg,Fe)FeO_{2.5}$ components in Brg as a function of oxygen fugacity at 25 GPa and 1973 K from this study. Solid lines are calculated from the thermodynamic models described in section 4.1.2.

Fig. 5 (a) The variation of the Si content of Brg with the total trivalent cation content (i.e., $M^{3+} = Al^{3+} + Fe^{3+}$) for Fe and Al-bearing Brg at 25–27 GPa and 1873–2023 K. Two solid lines indicate the expected trend for the charge-coupled (CC) substitution and oxygen vacancy (OV) substitution mechanisms. Solid orange squares and open orange squares indicate Brg from Fp-saturated experiments from this study and from previous studies (Frost and Langenhorst, 2002; Frost et al., 2004; McCammon et al., 2004b) respectively. Open green squares are experiments without Fp (Lauterbach et al., 2000). (b) The amount of Fe^{3+} on the B site versus the difference between Fe^{3+} and Al in Brg. The two solid lines indicate the expected OV $(MgFe)FeO_{2.5}$ and CC $FeFeO_3$ component trends.

Fig. 6 (a) $Fe^{3+}/\Sigma Fe$ ratio and (b) Fe^{3+} content in Fe-bearing and Fe and Al-bearing Brg as a function of fO_2 at P = 25 GPa, T = 1973 K. Three sets of experiments (Red, Green, Blue) were performed with a fixed Fe content of 0.10 atoms pfu and different Al contents of either 0, 0.07 or 0.11 atoms pfu. One set of experiments (Grey) was performed at a lower Fe content of 0.07 atoms pfu with an equal amount of Al. The blue star indicates a Brg sample (S7209) with Al = 0.12 and Fe = 0.12 atoms pfu synthesized at a higher temperature of 2373 K. The three data points marked with arrows in Fig. 6b have a lower Fe content of 0.06 and 0.05 atoms pfu respectively. The solid lines are calculated from the thermodynamic models described in sections 4.1.2 and 4.1.3.

Fig. 7 (a) Brg $Fe^{3+}/\Sigma Fe$ ratio as a function of Al content at a fixed total Fe content of 0.10–0.12 atoms pfu and an fO_2 of IW - 0.6 and IW + 7.5 at 25 GPa and 1973 K. Open squares show Brg compositions from Lauterbach et al. (2000) from samples equilibrated with Fe metal at 26 GPa and 1923–2023 K and with Fe = 0.08–0.11 atoms pfu. (b) Brg $Fe^{3+}/\Sigma Fe$ ratio versus total iron concentration (in atoms pfu) at the conditions indicated. Open blue symbols show results from previous studies performed at 24–26 GPa, 1873–2023 K and Fe metal saturated conditions (Frost et al., 2004; Lauterbach et al., 2000). The open orange symbols show previous results from experiments at 24–25 GPa and higher temperatures of 2173–2573 K performed in graphite capsules (Boujibar et al., 2016; Frost et al., 2004). The solid curves in both (a) and (b) are calculated using the thermodynamic model described in section 4.1.3 at the conditions indicated.

Fig. 8 The $Fe^{2+}/(Fe^{2+}+Mg)$ molar ratios of Brg versus Fp from Fe and Al-bearing experiments conducted at different oxygen fugacities. Symbols indicate our experimental data and the solid line shows the calculated results using the thermodynamic model proposed by Nakajima et al. (2012). The arrow shows the direction to equilibrium for experiments where Fp initially gained extra Fe^{2+} due to oxidation of coexisting iron metal.

Fig. 9 Proportions of trivalent cations and OV in Brg as a function of fO_2 for Brg with the nominal Al and Fe contents indicated in atoms pfu. The symbols indicate experimental results and solid curves indicate the results of the model described in section 4.1.3 at 25 GPa and 1973 K.

Fig. 10 Calculations of K_D (i.e., the Fe^{2+}-Mg Brg-Fp exchange coefficient) and K_D (app), which assumes all Fe is Fe^{2+}, and the $Fe^{3+}/\Sigma Fe$ ratio of both Brg and the whole rock calculated for a pyrolite composition as a function of fO_2. The calculation employs the thermodynamic model described in section 4.1.3 at 25 GPa and 1973 K. The blue shaded region shows the range in K_D (app) reported by Irifune et al. (2010) for a pyrolite composition between 28.7 and 47.4 GPa. While Irifune et al. (2010) suggest that the changes in K_D (app) may result from an Fe^{2+} spin transition in Fp, the results presented here show that changes in the experimental fO_2 between IW and IW + 1.5 can also explain the range of K_D (app). The rectangles indicate conditions where the fO_2 is low enough for Fe-Ni metal precipitation to occur and mark the effective lowest plausible fO_2.

Fig. 11 Calculations for the proportion of Fe-Ni alloy formed, in weight %, for pyrolite and harzburgite bulk compositions as a function of (a) the initial $Fe^{3+}/\Sigma Fe$ ratio of the whole rock before Brg formation and (b) the corresponding fo_2 of the Brg bearing assemblage, at 25 GPa and 1973 K. The fo_2 in the presence of Fe-Ni alloy in the lower mantle only decreases slightly from IW - 0.71 to IW - 0.87 when the initial bulk rock $Fe^{3+}/\sum Fe$ ratio decreases from 0.26 to 0, implying that the fo_2 of the lower mantle will vary very little even if the oxidation state of material entering the lower mantle varies significantly.

Fig. 12 The proportion of the $MgAlO_{2.5}$ Brg component as a function of pressure for Fe-free Brg with an Al content of 0.1 atoms pfu coexisting with periclase at 2000 K. The open circles indicate experimental data in the Al-Mg-Si-O system from Liu et al. (2017). The solid curve shows the results of the Al-Mg-Si-O model assuming that all Brg components have the same bulk modulus as the $MgSiO_3$ Brg end member. The shaded region shows the model uncertainties propagated from the molar volume determinations and from making different assumptions concerning the Brg component bulk moduli, as discussed in the text and given in Table B.5.

Fig. 13 Brg $Fe^{3+}/\Sigma Fe$ ratios calculated as a function of pressure at 1973 K for different compositions and oxygen fugacities, as indicated, and compared with results from previous experimental studies. The red and green solid lines are calculated for a pyrolite composition at a constant fo_2 of IW + 1.5 (red) and in equilibrium with Fe-Ni metal (green). Shaded regions show estimated uncertainties as in Fig. 12. Previous laser-heated diamond anvil cell results from Andrault et al. (2018); Kupenko et al. (2015); Shim et al. (2017); Prescher et al. (2014) and Piet et al. (2016) and multi-anvil experimental results from Irifune et al. (2010) and Stagno et al. (2011) are also shown, with the Brg compositions indicated. The blue solid line is a model calculation for Brg with a similar composition to that reported by Prescher et al. (2014). The upper and lower value from Irifune et al. (2010) are measurements made on the same sample using electron energy loss and Mössbauer spectroscopy respectively.

Fig. 14 Apparent Fe-Mg exchange coefficients K_D (app), which assumed all iron is Fe^{2+}, between Brg and Fp are calculated for different fo_2 conditions and at a constant $Fe^{3+}/\Sigma Fe$ ratio of 0.69 (solid curves). The actual Fe^{2+}-Mg exchange coefficient, K_D, is also plotted (dashed green curve). Shaded regions show estimated

uncertainties as in Fig. 12. Experimental data from Irifune (1994) and Irifune et al. (2010) are shown for comparison, with arrows pointing to data points where the Brg $Fe^{3+}/\Sigma Fe$ ratios were measured and the values obtained with different techniques are indicated.

Fig. 15 Model results for (a) proportions of trivalent cations and (b) OV and Fe^{3+} on the Brg B site as a function of pressure at 1973 K for a pyrolite composition in equilibrium with Fe-Ni alloy. Shaded regions show estimated uncertainties as in Fig. 12.

Table 1 Compositions of pyroxene and glass starting materials.

		MgO	SiO_2	Al_2O_3	Fe_2O_3	Tot.	Mg	Si	Al	Fe	ΣCat.
(A)	F11	34.7	57.2	-	8.0[a]	100	0.89	1.00	-	0.11	2.0
(B)	A7F7	36.6	54.5	3.5	5.5	100	0.93	0.93	0.07	0.07	2.0
(C)	A7F11	35.3	52.7	3.4	8.6[b]	100	0.91	0.91	0.07	0.11	2.0
(D)	A12F12	34.0	50.8	5.9	9.3[b]	100	0.88	0.88	0.12	0.12	2.0
(E)	A25F11	31.8	47.4	12.3	8.5[a]	100	0.82	0.82	0.25	0.11	2.0

Notes: Oxides are reported in wt. %. Cations are reported normalized to two cations. (A)-(D) crystallized to pyroxene during the reducing procedure and (E) was still glass since it was not reduced. [a]Enriched with 20 % ^{57}Fe. [b]Enriched with 100 % ^{57}Fe.

Table 2 Experimental conditions and run products. All experiments were conducted at 25 GPa.

Run No.	Starting composition (wt. %)	Buffer	Capsule	Temp. (°C)	Duration (h)	log f_{O_2} (ΔIW)	$Fe^{3+}/\sum Fe$ Brg	Phases
S7122	(A) + 5 % Fp + 10 % Fe	Fe	Pt-Au	1700	20	-0.71 (25)	0.12(3)	Brg, Fp, Fe, Fe_3C
S7251	(A) + 5 % Fp + 10 % ReO_2	ReO_2	Re	1700	12	4.05 (52)	0.32(5)	Brg, Fp, Re, ReO_2
S7262	(A) + 5 % Fp + 10 % ReO_2	ReO_2	Re	1700	12	4.05 (52)	0.27(7)	Brg, Fp, Re, ReO_2
S7113	(A) + 5 % Fp + 10 % Ru + 10 % RuO_2	Ru-RuO_2	Pt	1700*	4	7.65 (31)	0.66(5)	Brg, Fp, Ru, RuO_2, Mst, CT/CM
S7138-1	(A) + 5 % Fp + 10 % Ru + 10 % RuO_2	Ru-RuO_2	Pt	1700*	12	7.65 (31)	0.69(6)	Brg, Fp, Ru, RuO_2, Mst, CT/CM
S7120	(A) + 5 % Fp + 10 % PtO_2	Pt-PtO_2	Pt	1700	12	8.75 (87)	0.92(4)	Brg, Fp, Pt, Mst
H4737	(B) + 5 % Fp + 15 % Fe	Fe	Pt-Au	1700	24	-0.93 (13)	0.53(6)	Brg, Fp, Fe, Fe_3C
S7132-2	(B) + 3 % Fp + 10 % Fe	Fe	Pt-Au	1700	24	-0.82 (14)	0.53(7)	Brg, Fp, Fe, Fe_3C
S7021	(B) + 5 % Fp + 5 % Ir	Ir	Pt-Au	1700	12	2.30 (82)	0.70(6)	Brg, Fp, Fe-Ir alloy
S7028	(B) + 5 % Fp + 1 % Ru + 9% RuO_2	Ru-RuO_2	Pt	1700	12	7.65 (31)	0.94(5)	Brg, Fp, Ru, RuO_2, Mst
H4755	(C) + 5 % Fp + 15 % Fe	Fe	Pt-Au	1700	24	-0.64 (5)	0.37(5)	Brg, Fp, Fe, Fe_3C
S7132-1	(C) + 3 % Fp + 10 % Fe	Fe	Pt-Au	1700	24	-0.67 (6)	0.37(7)	Brg, Fp, Fe, Fe_3C
S7046	(C) + 5 % Fp + 1 % Ru + 9% RuO_2	Ru-RuO_2	Pt	1700	12	7.65 (31)	0.88(3)	Brg, Fp, Ru, RuO_2, Mst, CT/CM
S7138-2	(C) + 5 % Fp + 5 % Ru + 10% RuO_2	Ru-RuO_2	Pt	1700*	12	7.65 (31)	0.89(3)	Brg, Fp, Ru, RuO_2, Mst, CT/CM
H4746	(D) + 5 % Fp + 15 % Fe	Fe	Pt-Au	1700	24	-0.60 (5)	0.50(7)	Brg, Fp, Fe, Fe_3C, Mj
S7209	(D) + 5 % Fp + 2 % Fe	Fe	Re	2100*	2	-0.89 (5)	0.28(6)	Brg, Fp, Fe
S6920#	(D) + 5 % Fp + 15 % Fe + 5 % Ir	Fe+Ir	Pt-Au	1700	12	-0.14 (11)	0.55(7)	Brg, Fp, Fe-Ir alloy, Fe_3C, Mj
S6907	(D) + 10 % Fp + 5 % Ir	Ir	Pt-Au	1700*	12	2.70 (73)	0.76(13)	Brg, Fp, Mst, Fe-Ir alloy
S6921	(D) + 5 % Fp + 20 % Fe_2O_3	Fe_2O_3	Pt-Au	1700	12	4.90 (66)	0.67(10)	Brg, Fp, $(Mg,Fe)_4O_5$, Mst
S6950-1	(D) + 5 % Fp + 20 % Fe_2O_3 + 5 % Ir	Fe_2O_3	Pt-Au	1700	12	3.95 (34)	0.69(8)	Brg, Fp, $(Mg,Fe)_4O_5$, Mst, Fe-Ir alloy
S6950-2	(D) + 5 % Fp + 20 % Fe_2O_3 + 5 % Pt	Fe_2O_3	Pt-Au	1700	12	3.61 (30)	0.51(5)	Brg, Fp, $(Mg,Fe)_4O_5$, Mst, Fe-Pt alloy
S6952	(D) + 5 % Fp + 1 % Ru + 9 % RuO_2	Ru-RuO_2	Pt	1700	12	7.65 (30)	0.95(3)	Brg, Fp, Ru, RuO_2, Mst
S7214	(E) + 5 % Fp + 3 % Ru + 10 % RuO_2	Ru-RuO_2	Pt	1700	12	7.65 (31)	0.98(2)	Brg, Fp, Mst, CF, Ru, RuO_2

Notes: Brg, bridgmanite; Fp, ferropericlase; Mst, magnesite; Mj, majorite garnet; CF, $(Mg,Fe)_2SiO_4$-$(Mg,Fe)Al_2O_4$ solid solution with the $CaFe_2O_4$ structure; CT/CM, $(Mg,Fe)(Fe,Ru,Si)_2O_4$ phase with $CaTi_2O_4$ or $CaMn_2O_4$ structure. *Temperature estimated from the power curve due to failure of the thermocouple. #One drop of water was also added.

Table 3 Compositions in wt. % of Brg, Fp, magnesite (Mst) and other oxides and cation proportions normalized by number of atoms per formula unit.

Run #	Phase	No.	MgO	SiO_2	FeO	Al_2O_3	RuO_2	Total	Mg	Si	Fe	Al	Ru	ΣCat
S7122	Brg	27	35.3(4)	56.8(4)	6.7(4)	-	-	98.8(5)	0.915(8)	0.988(8)	0.098(5)	-	-	2.00
	Fp	19	57.8(106)	0.2(1)	41.2(104)	-	-	99.1(7)	0.708(88)	0.001(1)	0.290(89)	-	-	1.00
S7251	Brg	29	36.7(4)	57.0(5)	6.3(5)	-	-	100.0(7)	0.935(7)	0.975(7)	0.091(7)	-	-	2.00
	Fp	16	64.5(12)	0.2(3)	35.9(12)	-	-	100.7(7)	0.760(9)	0.002(2)	0.238(9)	-	-	1.00
S7262	Brg	59	36.7(4)	57.7(5)	6.2(5)	-	-	100.6(6)	0.931(6)	0.981(7)	0.088(8)	-	-	2.00
	Fp	34	58.3(12)	0.1(1)	42.1(11)	-	-	100.05(6)	0.711(10)	0.001(1)	0.288(9)	-	-	1.00
S7113	Brg	36	38.1(4)	57.7(5)	4.0(5)	-	-	99.9(6)	0.964(9)	0.979(7)	0.057(7)	-	-	2.00
	Fp	18	90.9(7)	0.2(1)	8.5(4)	-	-	99.5(6)	0.949(2)	0.001(1)	0.050(2)	-	-	1.00
	Mst	4	46.4(6)	1.2(6)	1.0(1)	-	-	48.6(7)	0.971(10)	0.017(9)	0.012(1)	-	-	1.00
	CT/CM	6	15.7(5)	1.1(2)	45.2(12)	-	34.0(35)	96.0(24)	0.921(17)	0.040(6)	1.484(19)	-	0.555(13)	3.00
S7138-1	Brg	41	38.3(4)	58.1(5)	4.0(4)	-	-	100.4(7)	0.963(8)	0.980(8)	0.056(5)	-	-	2.00
	Fp	24	91.7(4)	0.1(2)	7.8(3)	-	-	99.6(5)	0.954(2)	0.001(1)	0.045(2)	-	-	1.00
	Mst	2	46.87(4)	0.05(3)	0.85(4)	-	-	47.77(5)	0.989(0)	0.001(0)	0.010(0)	-	-	1.00
	CT/CM	8	14.5(5)	1.0(6)	46.3(7)	-	32.5(7)	94.2(10)	0.853(25)	0.038(23)	1.530(34)	-	0.579(11)	3.00
S7120	Brg	37	36.8(3)	54.9(5)	7.3(5)	-	-	99.0(5)	0.946(6)	0.949(8)	0.105(8)	-	-	2.00
	Fp	5	86.2(2)	0.1(0)	12.2(2)	-	-	98.5(1)	0.926(1)	0.001(0)	0.074(1)	-	-	1.00
	Mst	30	47.3(4)	0.1(4)	0.7(1)	-	-	48.2(5)	0.991(2)	0.001(1)	0.008(2)	-	-	1.00
H4737	Brg	18	37.0(5)	55.6(5)	4.9(3)	3.8(4)	-	101.3(6)	0.925(11)	0.932(7)	0.069(5)	0.074(8)	-	2.00
	Fp	16	70.1(4)	0.2(2)	30.5(6)	0.3(1)	-	101.1(5)	0.800(4)	0.002(2)	0.195(4)	0.003(0)	-	1.00
S7132-2	Brg	19	36.8(4)	55.8(5)	4.9(2)	3.7(4)	-	101.2(5)	0.921(7)	0.937(9)	0.068(2)	0.073(8)	-	2.00
	Fp	22	64.3(58)	0.3(4)	36.2(57)	0.4(1)	-	101.2(7)	0.754(44)	0.002(3)	0.240(44)	0.004(1)	-	1.00

(continued on next page)

Table 3 (Continued)

Run #	Phase	No.	MgO	SiO_2	FeO	Al_2O_3	RuO_2	Total	Mg	Si	Fe	Al	Ru	ΣCat
S7021	Brg	23	36.9(6)	56.8(6)	4.2(3)	3.5(6)	-	101.4(4)	0.921(13)	0.951(10)	0.059(4)	0.069(11)	-	2.00
	Fp	12	81.8(9)	0.3(4)	18.8(8)	0.2(1)	-	101.1(6)	0.882(5)	0.002(3)	0.113(5)	0.002(1)	-	1.00
S7028	Brg	17	36.8(2)	55.3(6)	5.4(4)	3.3(2)	-	100.9(6)	0.925(6)	0.932(7)	0.076(5)	0.066(4)	-	2.00
	Fp	16	92.5(5)	0.3(4)	6.4(2)	0.1(0)	-	99.3(6)	0.961(1)	0.001(1)	0.037(1)	0.001(0)	-	1.00
	Mst	14	47.6(5)	0.3(4)	0.6(1)	0.0(0)	-	48.5(6)	0.990(3)	0.003(3)	0.007(2)	0.000(0)	-	1.00
H4755	Brg	15	35.7(4)	54.893)	7.0(5)	3.7(4)	-	101.2(4)	0.900(7)	0.928(4)	0.099(7)	0.074(8)	-	2.00
	Fp	17	54.2(8)	0.2(2)	46.5(8)	0.5(1)	-	101.3(4)	0.671(7)	0.001(2)	0.323(7)	0.005(1)	-	1.00
S7132-1	Brg	37	35.0(7)	55.3(5)	7.0(6)	3.9(4)	-	101.2(6)	0.886(14)	0.938(9)	0.099(8)	0.077(8)	-	2.00
	Fp	27	55.8(26)	0.1(1)	45.0(26)	0.3(0)	-	101.3(7)	0.685(22)	0.001(1)	0.311(22)	0.003(0)	-	1.00
S7046	Brg	27	36.0(3)	53.0(4)	6.9(3)	3.4(1)	-	99.2(6)	0.922(6)	0.911(6)	0.099(4)	0.069(2)	-	2.00
	Fp	29	88.9(5)	0.1(1)	9.7(4)	0.1(0)	-	98.8(5)	0.941(3)	0.001(0)	0.057(3)	0.001(0)	-	1.00
	Mst	29	46.9(4)	0.2(2)	1.1(2)	0.0(0)	-	48.2(5)	0.985(5)	0.000(1)	0.013(2)	0.002(3)	-	1.00
S7138-2	Brg	37	35.9(3)	53.7(4)	6.7(4)	3.3(1)	-	99.6(5)	0.918(5)	0.920(6)	0.096(5)	0.067(2)	-	2.00
	Fp	27	90.5(5)	0.1(1)	8.7(3)	0.0(0)	0.8(4)	100.1(7)	0.946(2)	0.000(1)	0.051(2)	0.000(0)	0.003(1)	1.00
	Mst	23	47.7(5)	0.0(1)	0.8(1)	-	-	48.6(5)	0.989(2)	0.001(1)	0.010(1)	-	-	1.00
	CT/CM	23	15.0(3)	0.8(2)	48.0(12)	-	30.2(6)	94.0(10)	0.874(17)	0.030(7)	1.565(24)	-	0.531(13)	3.00
H4746	Brg	23	34.2(6)	52.8(8)	8.2(7)	5.5(5)	-	100.6(8)	0.870(10)	0.902(12)	0.118(10)	0.110(9)	-	2.00
	Fp	23	51.4(19)	0.2(2)	49.1(19)	0.3(0)	-	100.9(6)	0.648(17)	0.001(2)	0.347(17)	0.003(0)	-	1.00
	Mj	18	26.8(5)	46.9(7)	9.1(6)	17.2(9)	-	100.0(7)	2.790(47)	3.273(42)	0.528(39)	1.409(67)	-	8.00
S7209	Brg	38	33.3(4)	52.4(4)	8.3(7)	5.8(2)	-	99.8(7)	0.856(7)	0.904(8)	0.120(10)	0.119(3)	-	2.00
	Fp	24	62.6(10)	0.2(1)	35.8(12)	1.6(1)	-	100.3(6)	0.744(8)	0.002(1)	0.239(9)	0.015(1)	-	1.00
S6920	Brg	15	33.7(5)	53.1(4)	8.4(5)	6.1(4)	-	101.3(5)	0.855(10)	0.903(8)	0.119(7)	0.123(8)	-	2.00
	Fp	17	41.0(4)	0.1(1)	58.3(9)	0.5(1)	-	100.0(10)	0.552(5)	0.001(1)	0.441(5)	0.006(1)	-	1.00

(continued on next page)

Table 3 (Continued)

Run #	Phase	No.	MgO	SiO_2	FeO	Al_2O_3	RuO_2	Total	Mg	Si	Fe	Al	Ru	ΣCat
	Mj	1	25.7	45.09	12.91	17.55	-	101.2	2.668	3.140	0.752	1.440	-	8.00
S6907	Brg	21	34.4(4)	52.2(4)	7.5(4)	5.6(2)	-	99.6(7)	0.882(6)	0.897(7)	0.108(6)	0.113(3)	-	2.00
	Fp	15	81.8(5)	0.12(8)	18.3(5)	0.25(5)	-	100.4(9)	0.886(2)	0.001(1)	0.111(2)	0.002(0)	-	1.00
	Mst	3	46.9(2)	0.6(2)	1.94(2)	-	-	49.4(4)	0.969(3)	0.008(3)	0.023(0)	-	-	1.00
S6921	Brg	34	31.7(5)	49.8(4)	14.8(6)	5.1(1)	-	101.4(4)	0.818(9)	0.863(6)	0.214(9)	0.105(3)	-	2.00
	Fp	12	71.1(4)	0.5(1)	29.5(4)	0.3(0)	-	101.4(5)	0.806(3)	0.004(1)	0.188(3)	0.003(0)	-	1.00
	$(Mg,Fe)_4O_5$	19	22.0(3)	1.7(1)	69.2(8)	1.5(1)	-	94.3(8)	1.394(14)	0.073(4)	2.460(14)	0.073(4)	-	4.00
S6950-1	Brg	16	31.1(4)	49.3(3)	14.5(6)	5.3(1)	-	100.1(9)	0.813(4)	0.865(7)	0.212(7)	0.109(3)	-	2.00
	Fp	11	32.2(4)	0.34(6)	67.7(9)	0.15(4)	-	100.3(11)	0.457(4)	0.003(1)	0.538(4)	0.002(0)	-	1.00
	$(Mg,Fe)_4O_5$	13	9.5(3)	1.6(2)	81.3(7)	1.3(1)	-	93.6(7)	0.664(19)	0.073(8)	3.194(22)	0.069(4)	-	4.00
S6950-2	Brg	18	28.8(5)	50.0(4)	16.6(5)	5.2(1)	-	100.6(9)	0.759(9)	0.886(7)	0.247(8)	0.108(3)	-	2.00
	Fp	7	22.5(3)	0.6(3)	75.7(6)	0.16(4)	-	99.1(5)	0.343(3)	0.007(3)	0.648(6)	0.002(0)	-	1.00
	$(Mg,Fe)_4O_5$	9	8.4(2)	1.9(3)	81.3(11)	1.0(1)	-	92.6(12)	0.599(15)	0.092(15)	3.252(23)	0.057(6)	-	4.00
S6952	Brg	37	34.7(4)	50.9(4)	8.6(3)	5.6(2)	-	99.8(7)	0.889(5)	0.875(5)	0.124(4)	0.113(3)	-	2.00
	Fp	22	91.7(6)	0.2(2)	7.1(3)	0.3(0)	-	99.3(7)	0.955(2)	0.001(1)	0.041(2)	0.002(2)	-	1.00
	Mst	17	46.1(4)	0.2(2)	0.9(2)	0(0)	-	47.3(5)	0.986(4)	0.003(3)	0.011(2)	0.001(1)	-	1.00
S7214	Brg	42	32.3(3)	46.2(4)	8.0(4)	11.2(4)	1.1(2)	98.8(6)	0.840(6)	0.804(7)	0.116(6)	0.231(7)	0.009(2)	2.00
	Fp	35	89.7(7)	0.2(3)	3.8(3)	1.9(1)	4.5(2)	100.2(7)	0.945(3)	0.002(2)	0.023(1)	0.016(1)	0.014(1)	1.00
	CF	19	36.3(4)	16.7(2)	4.4(3)	35.2(3)	6.5(3)	99.1(6)	1.367(7)	0.421(5)	0.092(5)	1.046(8)	0.074(3)	3.00
	Mst	11	46.3(9)	0.5(4)	0.6(2)	0.4(1)	0.4(6)	48.1(9)	0.977(9)	0.006(5)	0.007(2)	0.007(2)	0.003(4)	1.00

Notes: No. indicates the number of points measured for each phase and the numbers in parenthesis are 1 sigma standard deviations. The abbreviations are the same as in Table 2.

Table 4 Cation proportions and site assignments in Brg normalized to two cations per formula unit.

		A site				B site					
	Run	Mg	Fe^{2+}_A	Fe^{3+}_A	Al_A	Si	Al_B	Fe^{3+}_B	OV	$Fe^{3+}/\Sigma Fe$	log fo_2 (ΔIW)
$Fe_{0.10}$	S7122	0.915(8)	0.086(6)	-	-	0.988(8)	-	0.012(8)	0.006	0.12(3)	-0.71(25)
	S7251	0.935(7)	0.061(6)	0.004(9)	-	0.975(7)	-	0.025(7)	0.011	0.32(5)	4.05(52)
	S7262	0.931(6)	0.064(8)	0.005(9)	-	0.981(7)	-	0.019(7)	0.007	0.27(7)	4.05(52)
	S7113	0.964(9)	0.019(4)	0.017(9)	-	0.979(7)	-	0.021(7)	0.002	0.66(5)	7.65(31)
	S7138-1	0.963(8)	0.017(5)	0.019(10)	-	0.980(8)	-	0.020(8)		0.69(9)	7.65(31)
	S7120	0.946(6)	0.008(4)	0.046(12)	-	0.949(8)	-	0.051(8)	0.003	0.92(4)	8.75(87)
$Al_{0.07}Fe_{0.10}$	H4755	0.900(7)	0.063(7)	0.036(6)	0.001(9)	0.928(4)	0.072(4)	-	0.017(6)	0.37(5)	-0.64(5)
	S7132-1	0.886(14)	0.062(9)	0.037(8)	0.015(12)	0.938(9)	0.062(9)	-	0.005(8)	0.37(7)	-0.67(6)
	S7046	0.922(6)	0.012(3)	0.067(8)	-	0.911(6)	0.069(2)	0.021(6)	0.011(5)	0.88(3)	7.65(31)
	S7138-2	0.918(5)	0.010(3)	0.072(8)	-	0.920(6)	0.067(2)	0.013(6)	0.004(5)	0.89(3)	7.65(31)
$Al_{0.12}Fe_{0.12}$	H4746	0.870(10)	0.059(10)	0.059(10)	0.012(15)	0.902(12)	0.098(12)	-	0.014(11)	0.50(7)	-0.60(5)
	S6920	0.855(10)	0.054(9)	0.065(9)	0.025(11)	0.903(8)	0.097(8)	-	0.003(8)	0.55(7)	-0.14(11)
	S6907	0.882(6)	0.026(14)	0.082(15)	0.010(7)	0.897(7)	0.103(7)	-	0.006(9)	0.76(13)	2.70(73)
	S6952	0.889(5)	0.006(3)	0.105(7)	-	0.875(5)	0.113(3)	0.012(6)	0.010(5)	0.95(3)	7.65(31)
$Al_{0.07}Fe_{0.07}$	H4737	0.925(11)	0.033(5)	0.036(5)	0.006(11)	0.932(7)	0.068(7)	-	0.013(7)	0.53(6)	-0.93(13)
	S7132-2	0.921(7)	0.032(5)	0.036(5)	0.011(12)	0.937(9)	0.063(9)	-	0.008(8)	0.53(7)	-0.82(14)
	S7021	0.921(13)	0.018(4)	0.041(5)	0.021(15)	0.951(10)	0.049(10)	-		0.70(6)	2.30(82)
	S7028	0.925(6)	0.004(4)	0.070(10)	-	0.932(7)	0.066(4)	0.002(8)		0.94(5)	7.65(31)
$Al_{0.25}Fe_{0.11}$	S7214	0.844(6)	0.003(3)	0.114(6)	0.040(10)	0.808(7)	0.192(7)	-	0.019(7)	0.98(2)	7.65(31)

Table 5. Thermodynamic parameters for the Al-Mg-Si-O and Fe-Mg-Si-O systems.

Thermodynamic parameters	Value (kJ/mol)
Al-Mg-Si-O system	
$\Delta G^{0}_{(15)}$	-19.5 (15)[a]
$W^{\mathrm{Brg}}_{\mathrm{AlSi,B}}$	−30 (2)
Fe-Mg-Si-O system	
$\Delta G^{0}_{(20)}$	-21 (2)
$\Delta G^{0}_{(24)}$	133 (10)
$W^{\mathrm{Brg}}_{\mathrm{MgFe^{3+},A}}$	11 (5)
$W^{\mathrm{Brg}}_{\mathrm{Fe^{2+}Fe^{3+},A}}$	11 (5)
$W^{\mathrm{Brg}}_{\mathrm{Fe^{3+}Si,B}}$	−28 (2)
$W^{\mathrm{Brg}}_{\mathrm{MgFe^{2+},A}}$	4.9 (76)[b]

[a] at 27 GPa, 2000 K

[b] Taken from Nakajima et al. (2012)

Table 6. Standard Gibbs energy of equilibria in the Fe-Al-Mg-Si-O system (25 GPa, 1973 K).

Eq. No.	Equilibrium	ΔG^0 (kJ/mol)
(26)	$MgSi_{7/8}Al_{1/8}O_{15/16}O_2 = 1/16\ AlAlO_3 + 7/8\ MgSiO_3 + 1/8\ MgO$	6.7
(27)	$MgSi_{7/8}Fe_{1/8}O_{15/16}O_2 = 1/16\ FeFeO_3 + 7/8\ MgSiO_3 + 1/8\ MgO$	-2.17
(28)	$2FeO + AlAlO_3 + 0.5\ O_2 = 2FeAlO_3$	11.87
(31)	$AlAlO_3 + FeFeO_3 = 2FeAlO_3$	-140.3
(32)	$2MgAlO_{2.5} = AlAlO_3 + 2MgO$	-30.8
(33)	$2MgFeO_{2.5} = FeFeO_3 + 2MgO$	-171.1

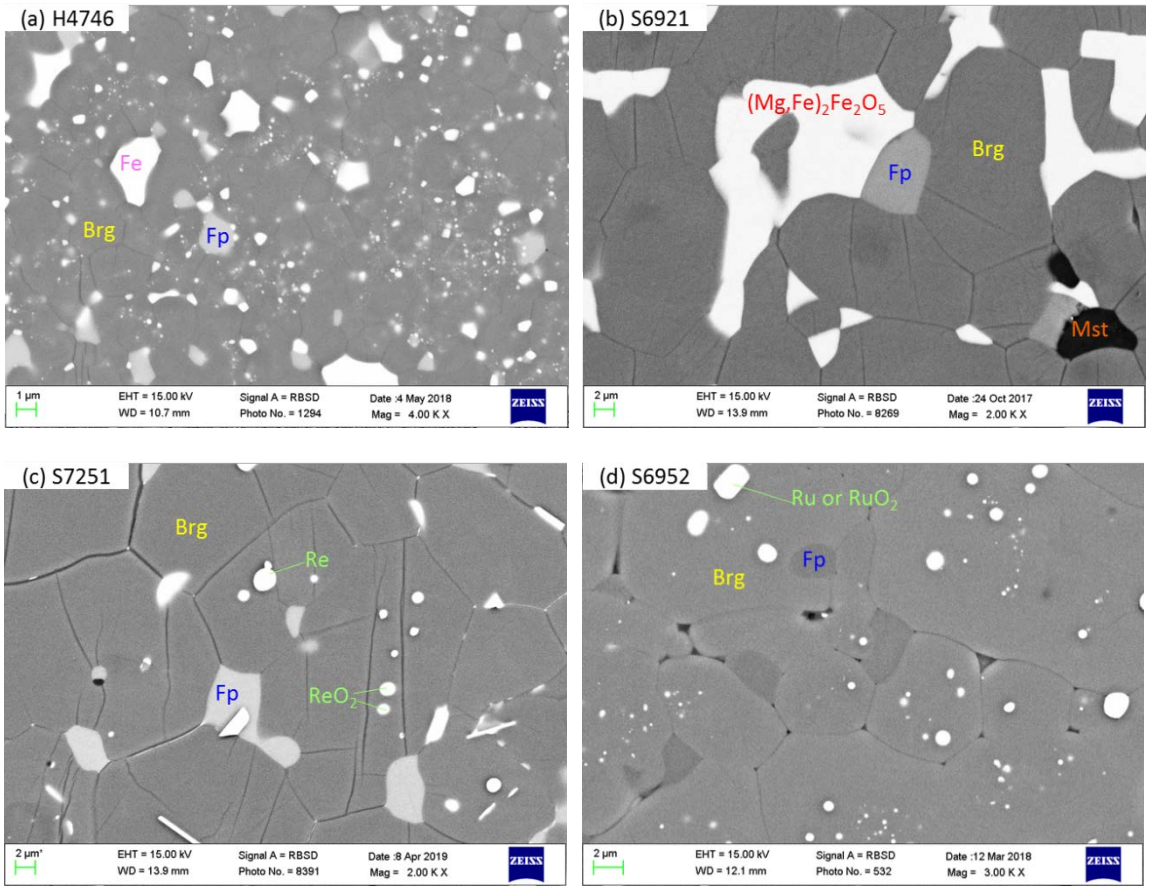

Fig. 1 Back-scattered electron images of experimental run products obtained using different oxygen buffers: (a) Run H4746: a low oxygen fugacity was obtained using Fe metal dispersed throughout the sample. (b) Run S6921: Hematite was added and reduced in the experiment to form $(Mg,Fe)_2Fe_2O_5$. Magnesite also formed from carbon contaminants. (c) Run S7251: The oxygen fugacity was buffered by coexisting Re and ReO_2. (d) Run S6952: High oxygen fugacity was achieved by the coexistence of Ru and RuO_2. In all the experiments, the buffer materials were well dispersed throughout the sample to minimize the diffusion pathways. Abbreviations: Brg, bridgmanite; Fp, ferropericlase; Mst, magnesite.

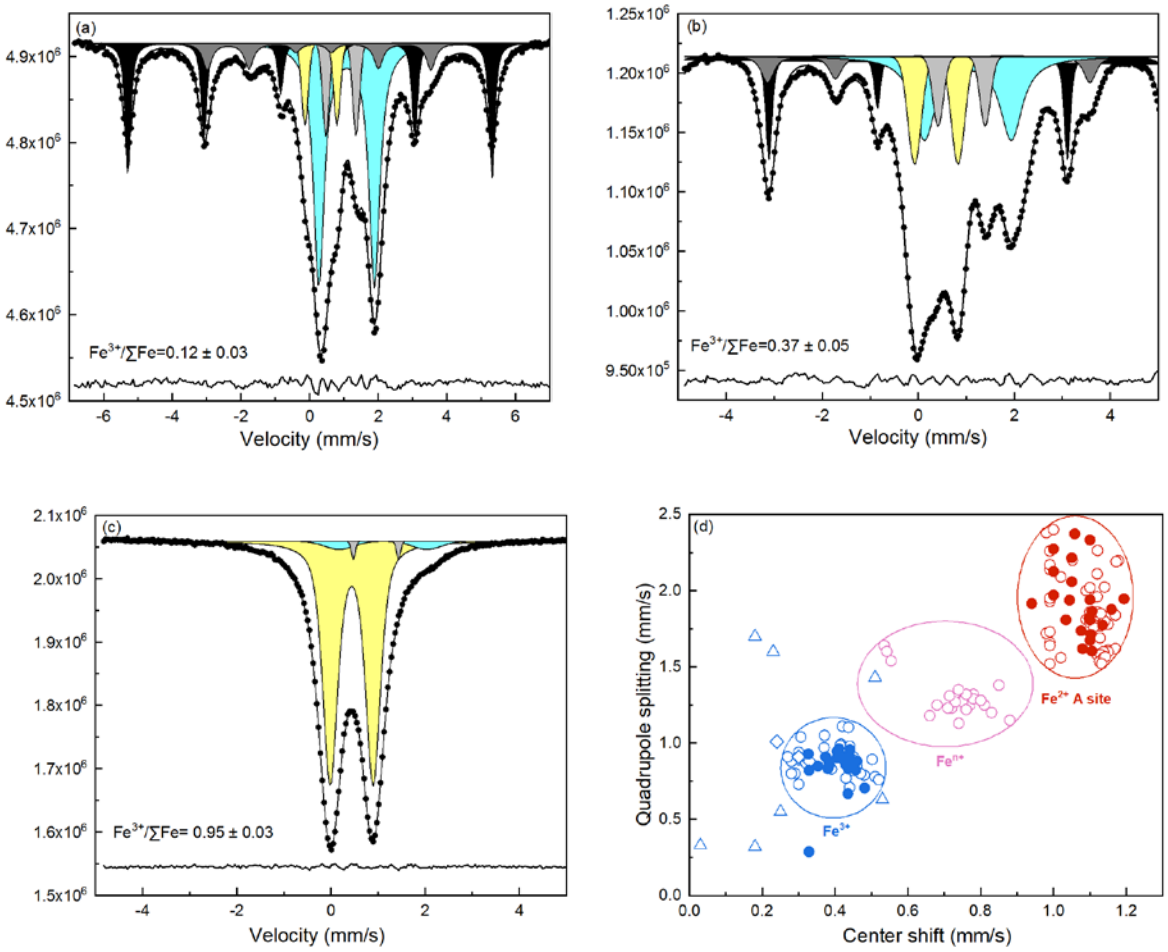

Fig. 2 Representative room temperature Mössbauer spectra of run products: (a) S7122 (Brg + Fp + Fe + carbide); (b) H4755 (Brg + Fp + Fe + carbide); (c) S6952 (Brg + Fp); (d) Hyperfine parameters of Brg from Mössbauer spectra collected at ambient conditions. In (a)-(c), the doublets correspond to Fe^{3+} (yellow) in Brg, Fe^{2+} in Brg (blue), and Fe^{2+} in Fp (light grey) and the magnetic sextets correspond to Fe metal (black) and Fe^{0} in carbide (dark grey). In (d), solid red and blue circles indicate the parameters of Fe^{2+} on the A site and Fe^{3+} in Brg obtained from this study respectively. Open red, pink and blue circles indicate the Brg Fe_A^{2+}, Fe^{n+}, and Fe^{3+} parameters from previous studies of Fei et al. (1994); Jackson et al. (2005); Lauterbach et al. (2000); Li et al. (2006); McCammon (1997, 1998); McCammon et al. (2004); McCammon et al. (1992) and Narygina et al. (2010). Fe^{n+} absorption represents electron transfer between Fe^{2+} and Fe^{3+} in Brg and cannot be resolved in spectra of this study due to its peak overlapping with Fp. The blue triangle and diamond represent the parameters of Fe^{3+} on the A site and B site in Brg proposed by Hummer and Fei (2012).

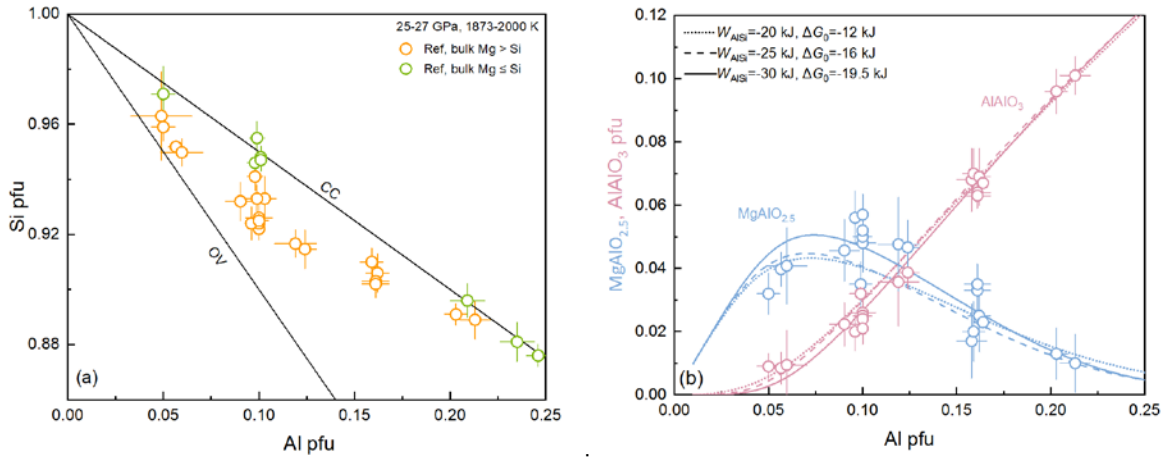

Fig. 3 (a) The variation of the Si content of Brg with Al content at 25-27 GPa and 1873-2000 K. The two solid lines are expected trend lines for CC substitution along the $MgSiO_3$-$AlAlO_3$ join and the OV substitution along the $MgSiO_3$-$MgAlO_{2.5}$ join respectively. The orange symbols indicate Brg samples formed from starting compositions with Mg > Si and the green symbols indicate starting bulk composition with Mg $\leqslant$ Si. Data are taken from Grüninger et al. (2019); Kojitani et al. (2007); Liu et al. (2017); Liu et al. (2019a); (2019b) and Navrotsky et al. (2003). (b) Symbols show the mole fractions of the $MgAlO_{2.5}$ and $AlAlO_3$ Brg components as a function of Al content from experiments at 27 GPa and 2000 K that had starting compositions with Mg > Si. Data are from the same sources as in (a). The curves are calculated using different sets of thermodynamic fitting parameters (see section 4.1.1) as indicated.

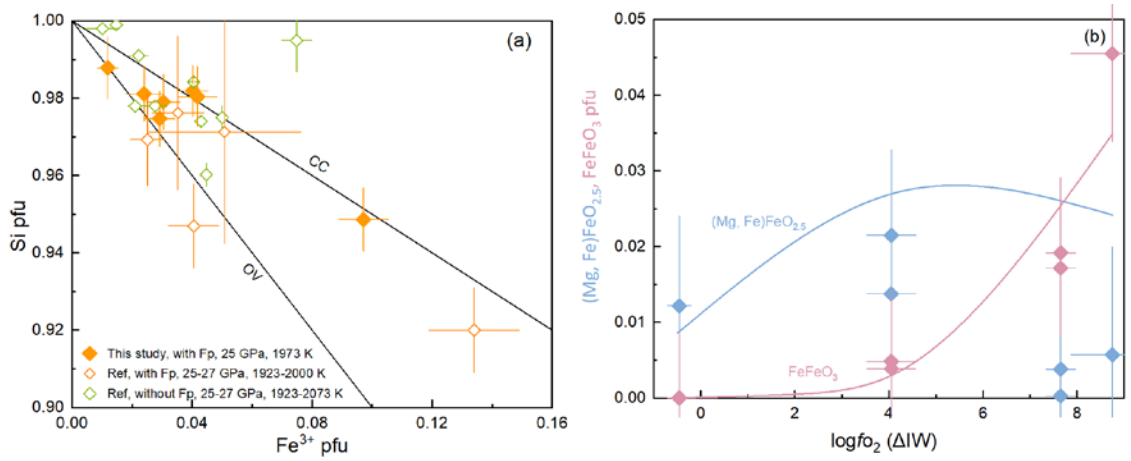

Fig. 4 (a) The variation of the Si content of Brg with the Fe^{3+} content at 25-27 GPa and 1923-2073 K. The solid lines indicate the CC $(Mg,Fe)SiO_3$-$Fe^{3+}Fe^{3+}O_3$ join and the OV $(Mg,Fe)SiO_3$-$(Mg,Fe)Fe^{3+}O_{2.5}$ join. The solid orange diamonds and the open orange diamonds indicate data from the current study and from previous studies (Fei et al., 2020; Frost and Langenhorst, 2002; McCammon et al., 2004) respectively, where Brg coexisted with Fp. The open green diamonds are data from Hummer and Fei (2012) and Lauterbach et al. (2000) where Brg is not in equilibrium with Fp. (b) The mole fraction of $FeFeO_3$ and $(Mg,Fe)FeO_{2.5}$ components in Brg as a function of oxygen fugacity at 25 GPa and 1973 K from this study. Solid lines are calculated from the thermodynamic models described in section 4.1.2.

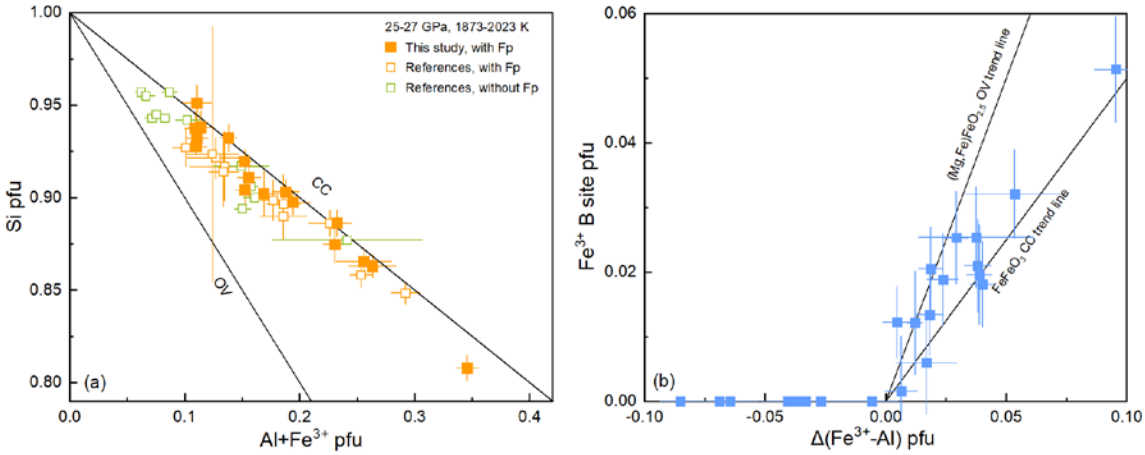

Fig. 5 (a) The variation of the Si content of Brg with the total trivalent cation content (i.e. $M^{3+}=Al^{3+}+Fe^{3+}$) for Fe and Al-bearing Brg at 25-27 GPa and 1873-2023 K. Two solid lines indicate the expected trend for the charge coupled (CC) substitution and oxygen vacancy (OV) substitution mechanisms. Solid orange squares and open orange squares indicate Brg from Fp saturated experiments from this study and from previous studies (Frost and Langenhorst, 2002; Frost et al., 2004; McCammon et al., 2004) respectively. Open green squares are for experiments without Fp (Lauterbach et al., 2000). (b) The amount of Fe^{3+} on the B site versus the difference between Fe^{3+} and Al in Brg. The two solid lines indicate the expected OV $(MgFe)FeO_{2.5}$ and CC $FeFeO_3$ component trends.

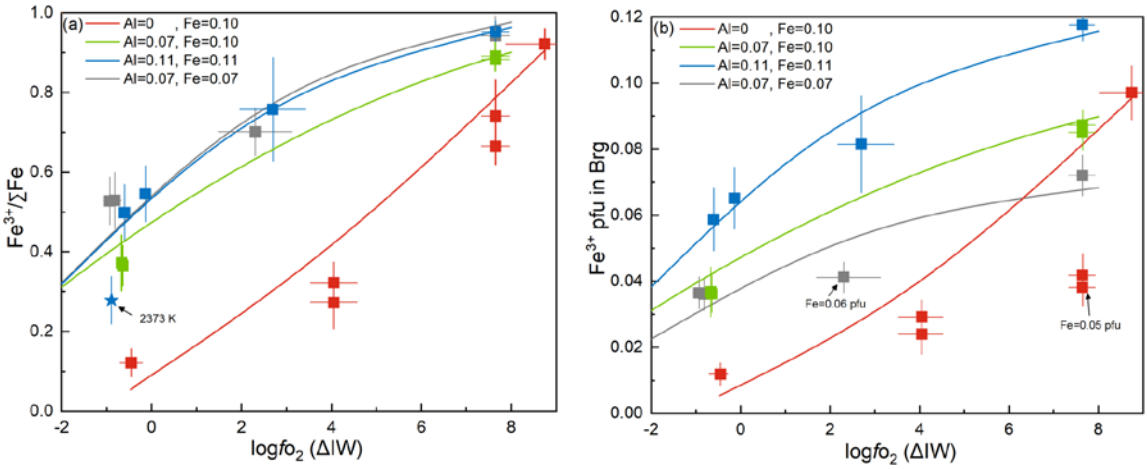

Fig. 6 (a) $Fe^{3+}/\Sigma Fe$ ratio and (b) Fe^{3+} content in Fe-bearing and Fe + Al-bearing Brg as a function of fO_2 at P= 25 GPa, T= 1973 K. Three sets of experiments (Red, Green, Blue) were performed with a fixed Fe content of 0.10 cations pfu and different Al contents of either 0, 0.07 or 0.11 atoms pfu. One set of experiments (Grey) was performed at a lower Fe content of 0.07 pfu with an equal amount of Al. The blue star indicates a Brg sample (S7209) with Al= 0.12 and Fe= 0.12 atoms pfu synthesized at a higher temperature of 2373 K. The three data points marked with arrows in Fig. 6b have a lower Fe content of 0.06 atoms pfu and 0.05 atoms pfu respectively. The solid lines are calculated from the thermodynamic models described in sections 4.1.2 and 4.1.3.

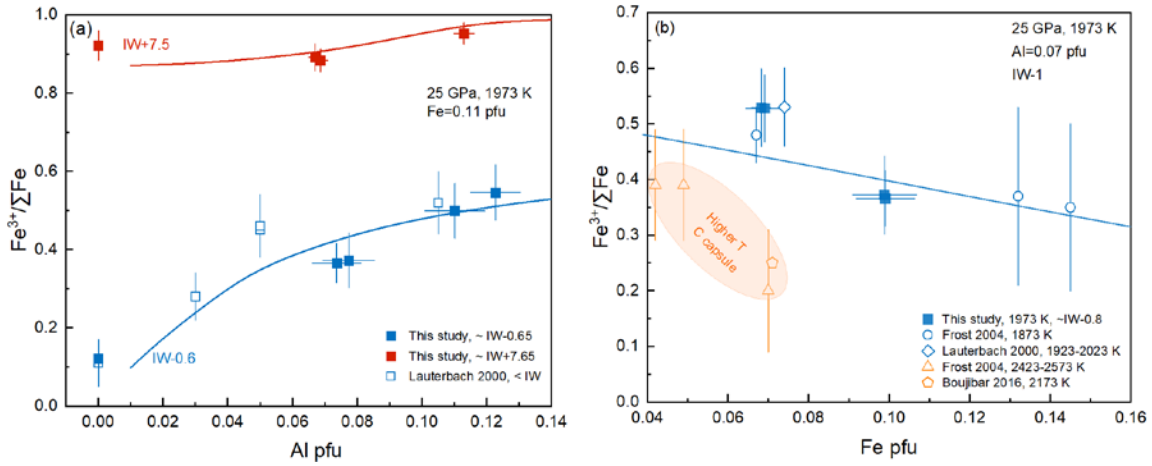

Fig. 7 (a) Brg $Fe^{3+}/\Sigma Fe$ ratio as a function of Al content at a fixed total Fe content of 0.10-0.12 atoms pfu and an fo_2 of IW - 0.6 and IW + 7.5 at 25 GPa and 1973 K. Open squares show Brg compositions from Lauterbach et al. (2000) from samples equilibrated with Fe metal at 26 GPa and 1923-2023 K and with Fe= 0.08-0.11 atoms pfu. (b) Brg $Fe^{3+}/\Sigma Fe$ ratio versus total iron concentration (in cations pfu) at the conditions indicated. Open blue symbols show results from previous studies performed at 24-26 GPa, 1873-2023 K and Fe metal saturated conditions (Frost et al., 2004; Lauterbach et al., 2000). The open orange symbols show previous results from experiments at 24-25 GPa and higher temperatures of 2173-2573 K performed in graphite capsules (Boujibar et al., 2016; Frost et al., 2004). The solid curves in both (a) and (b) are calculated using the thermodynamic model described in section 4.1.3 at the conditions indicated.

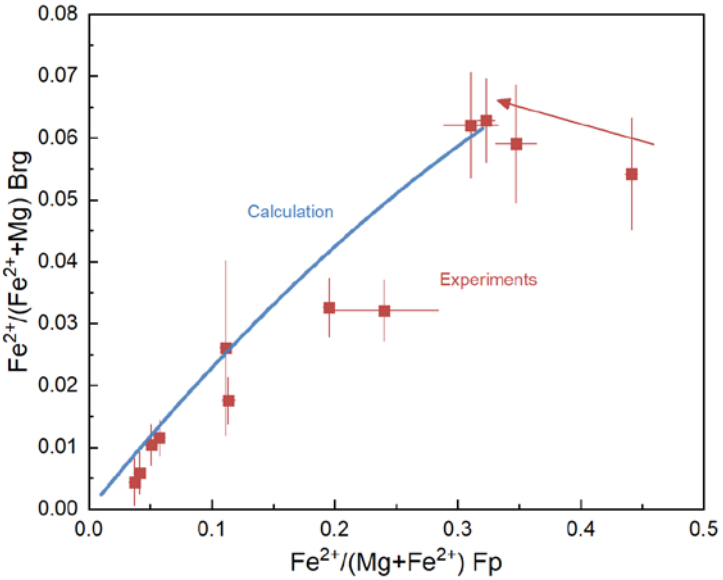

Fig. 8 The $Fe^{2+}/(Fe^{2+}+Mg)$ molar ratios of Brg versus Fp from Fe + Al-bearing experiments conducted at different oxygen fugacities. Symbols indicate our experimental data and the solid line shows the calculated results using the thermodynamic model proposed by Nakajima et al. (2012). The arrow shows the direction to equilibrium for experiments where Fp initially gained extra Fe^{2+} due to oxidation of coexisting iron metal.

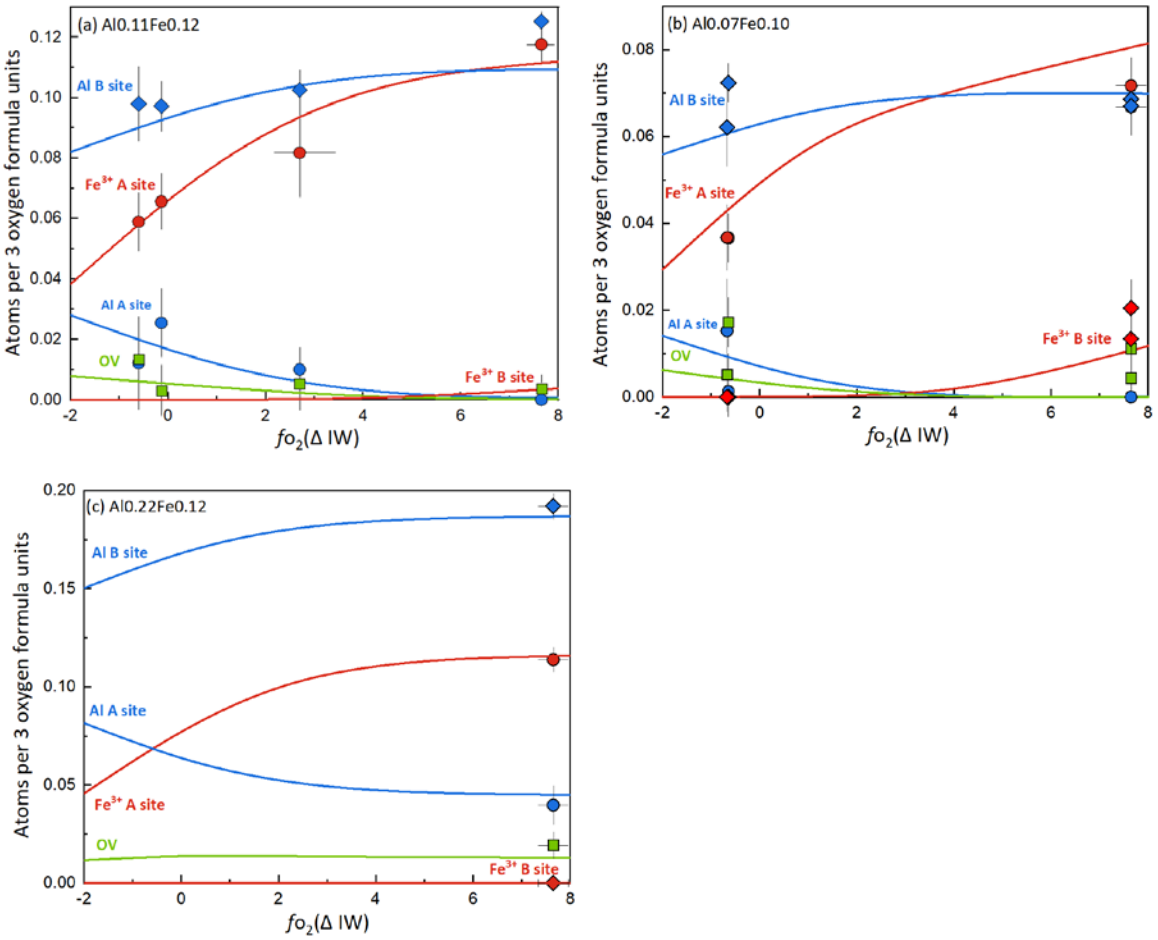

Fig. 9 Proportions of trivalent cations and OV in Brg as a function of fo_2 for Brg with the nominal Al and Fe contents indicated in cations pfu. The symbols indicate experimental results and solid curves indicate the results of the model described in section 4.1.3 at 25 GPa and 1973 K.

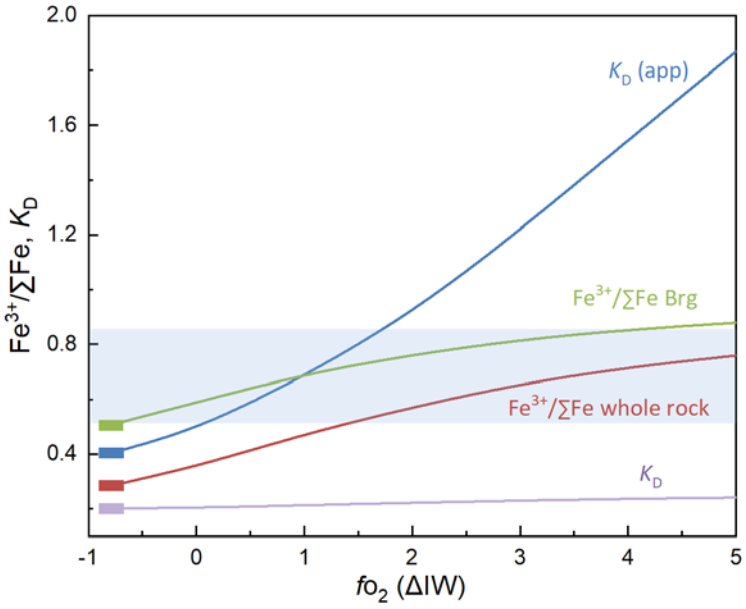

Fig. 10 Calculations of K_D (i.e. the Fe^{2+}-Mg Brg-Fp exchange coefficient) and K_D (app), which assumes all Fe is Fe^{2+}, and the $Fe^{3+}/\Sigma Fe$ ratio of both Brg and the whole rock calculated for a pyrolite composition as a function of fo_2. The calculation employs the thermodynamic model described in section 4.1.3 at 25 GPa and 1973 K. The blue shaded region shows the range in K_D (app) reported by Irifune et al. (2010) for a pyrolite composition between 28.7 and 47.4 GPa. While Irifune et al. (2010) suggest that the changes in K_D (app) may result from an Fe^{2+} spin transition in Fp, the results presented here show that changes in the experimental fo_2 between IW and IW + 1.5 can also explain the range of K_D (app). The rectangles indicate conditions where the fo_2 is low enough for Fe-Ni metal precipitation to occur and mark the effective lowest plausible fo_2.

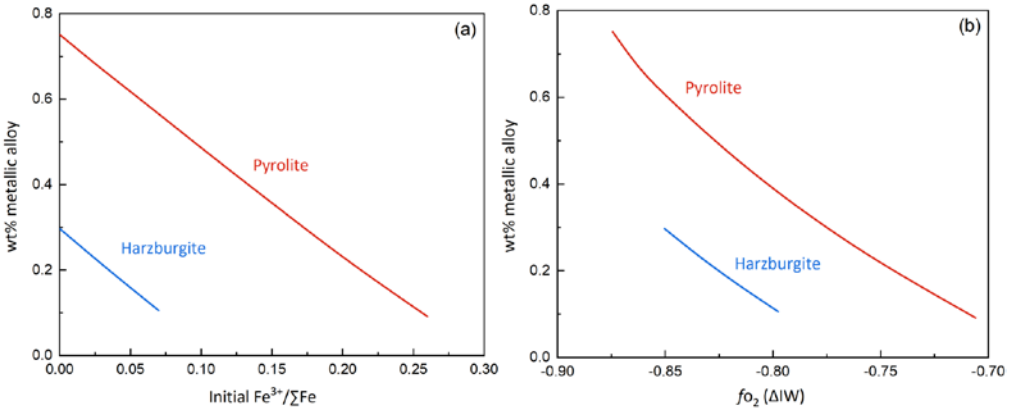

Fig. 11 Calculations for the proportion of Fe-Ni alloy formed, in weight %, for pyrolite and harzburgite bulk compositions as a function of (a) the initial $Fe^{3+}/\Sigma Fe$ ratio of the whole rock before Brg formation and (b) the corresponding fo_2 of the Brg bearing assemblage, at 25 GPa and 1973 K. The fo_2 in the presence of Fe-Ni alloy in the lower mantle only decreases slightly from IW - 0.71 to IW - 0.87 when the initial bulk rock $Fe^{3+}/\sum Fe$ ratio decreases from 0.26 to 0, implying that the fo_2 of the lower mantle will vary very little even if the oxidation state of material entering the lower mantle varies significantly.

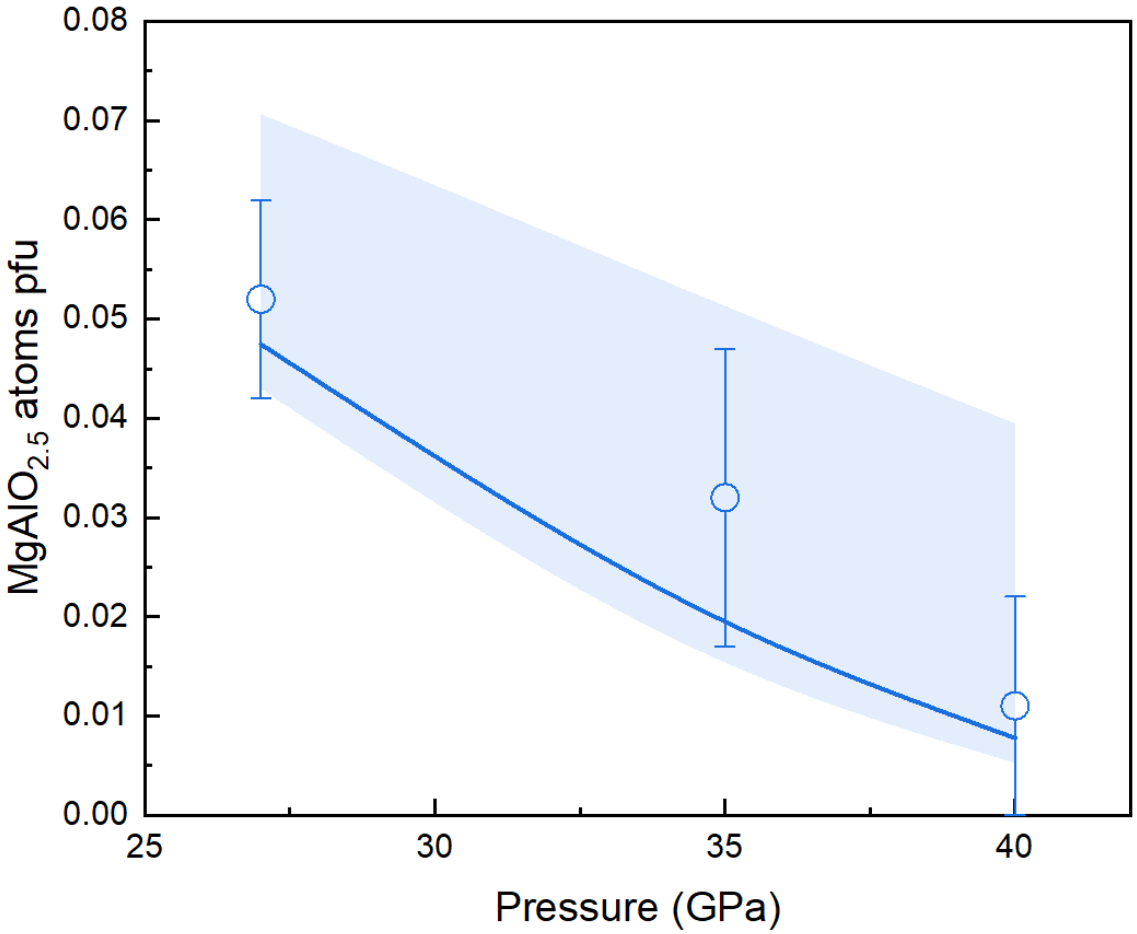

Fig. 12 The proportion of the $MgAlO_{2.5}$ Brg component as a function of pressure for Fe-free Brg with an Al content of 0.1 pfu coexisting with periclase at 2000 K. The open circles indicate experimental data in the Al-Mg-Si-O system from Liu et al. (2017). The solid curve shows the results of the Al-Mg-Si-O model assuming that all Brg components have the same bulk modulus as the $MgSiO_3$ Brg end member. The shaded region shows the model uncertainties propagated from the molar volume determinations and from making different assumptions concerning the Brg component bulk moduli, as discussed in the text and given in Table B.4.

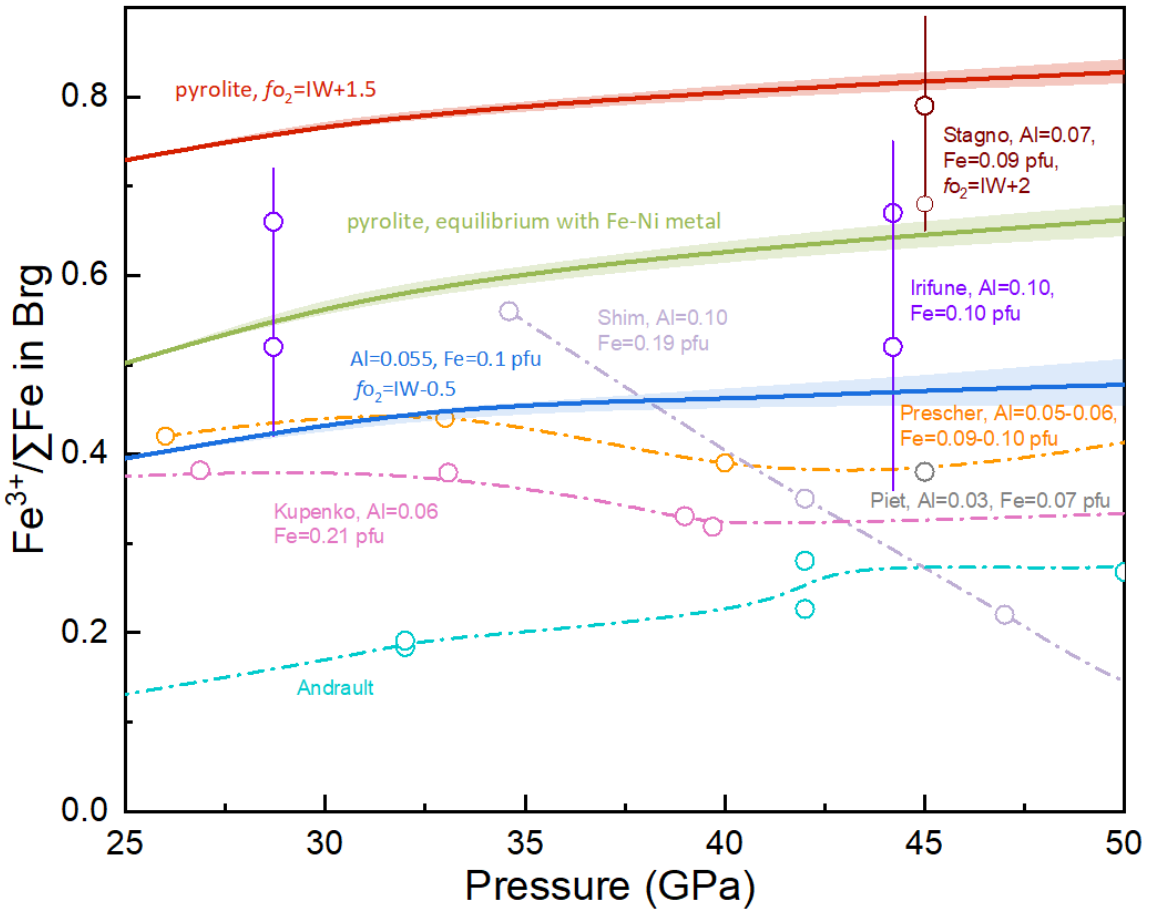

Fig. 13 Brg $Fe^{3+}/\Sigma Fe$ ratios calculated as a function of pressure at 1973 K for different compositions and oxygen fugacities, as indicated, and compared with results from previous experimental studies. The red and green solid lines are calculated for a pyrolite composition at a constant fo_2 of IW + 1.5 (red) and in equilibrium with Fe-Ni metal (green). Shaded regions show estimated uncertainties as in Fig.12. Previous laser-heated diamond anvil cell results from Andrault et al. (2018); Kupenko et al. (2015); Shim et al. (2017); Prescher et al. (2014) and Piet et al. (2016). Multi-anvil experimental results from Irifune et al. (2010) and Stagno et al. (2011) are also shown, with the Brg compositions indicated. The blue solid line is a model calculation for Brg with a similar composition to that reported by Prescher et al. (2014). The upper and lower value from Irifune et al. (2010) are measurements made on the same sample using electron energy loss and Mössbauer spectroscopy respectively.

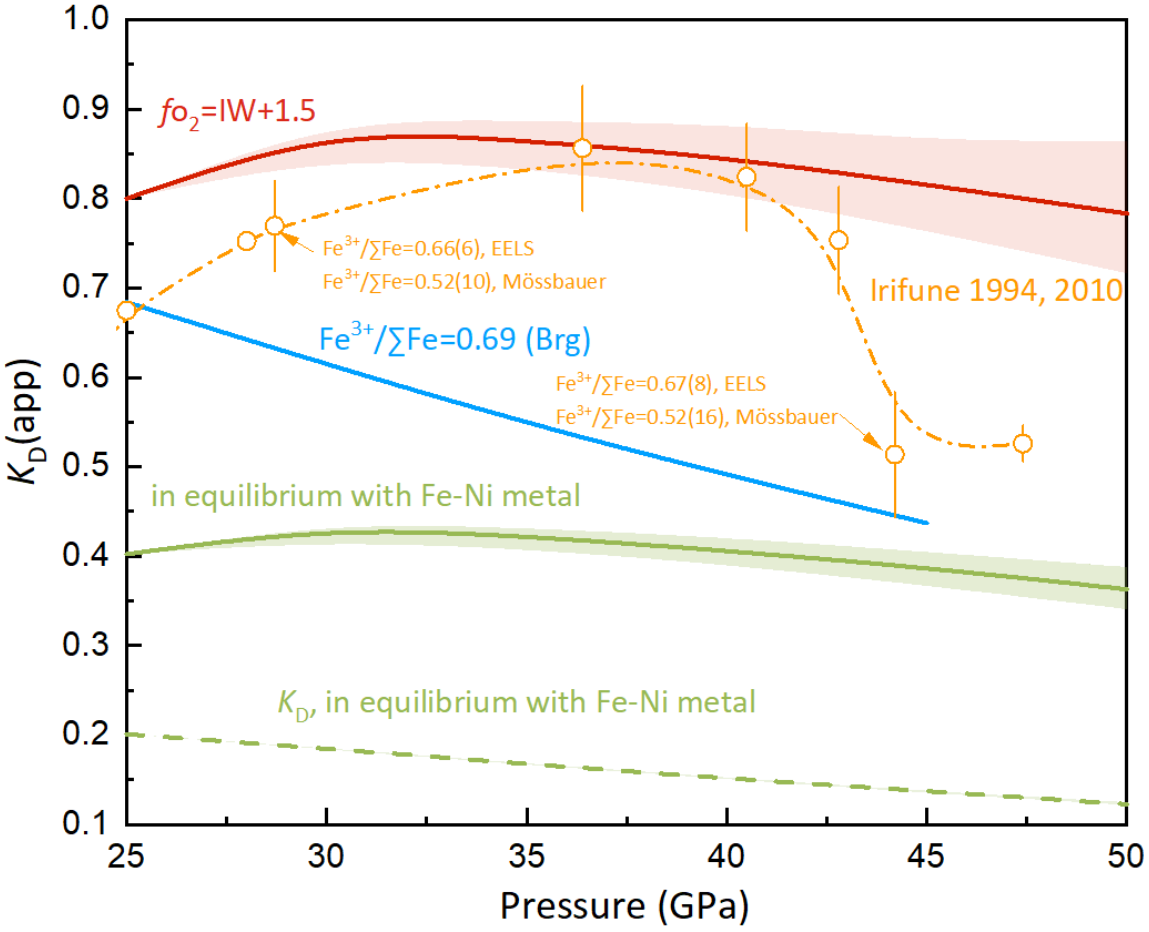

Fig. 14 Apparent Fe-Mg exchange coefficients K_D (app), which assumed all iron is Fe^{2+}, between Brg and Fp are calculated for different fo_2 conditions and at a constant $Fe^{3+}/\Sigma Fe$ ratio of 0.69 (solid curves). The actual Fe^{2+}-Mg exchange coefficient, K_D, is also plotted (dashed green curve). Shaded regions show estimated uncertainties as in Fig. 12. Experimental data from Irifune (1994) and Irifune et al. (2010) are shown for comparison, with arrows pointing to data points where the Brg $Fe^{3+}/\Sigma Fe$ ratios were measured and the values obtained with different techniques are indicated.

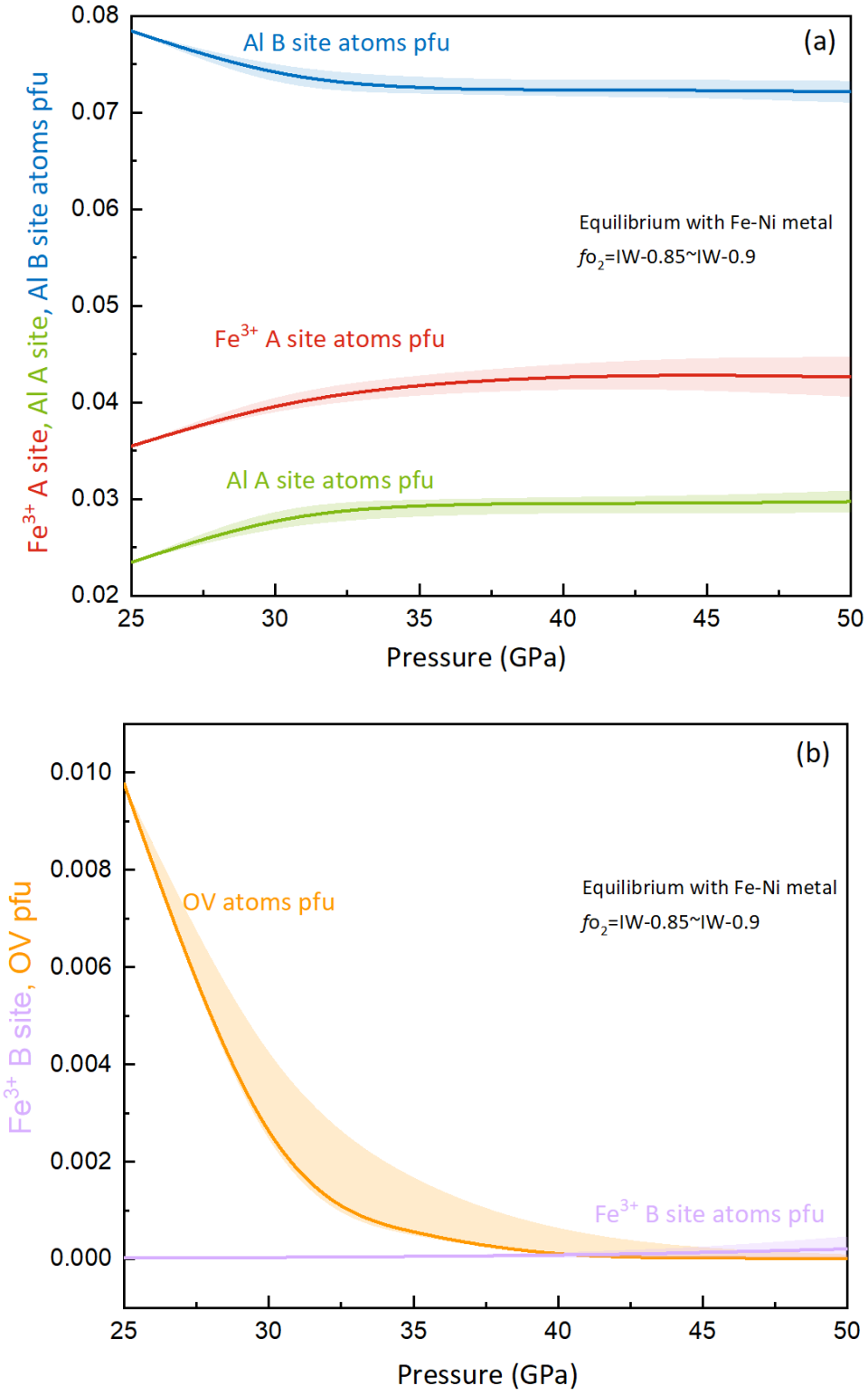

Fig. 15 Model results for (a) proportions of trivalent cations and (b) OV and Fe^{3+} on the Brg B site as a function of pressure at 1973 K for a pyrolite composition in equilibrium with Fe-Ni alloy. Shaded regions show estimated uncertainties as in Fig.12.

Andrault, D., Muñoz, M., Pesce, G., Cerantola, V., Chumakov, A., Kantor, I., Pascarelli, S., Rüffer, R. and Hennet, L. (2018) Large oxygen excess in the primitive mantle could be the source of the Great Oxygenation Event. Geochemical Perspectives Letters, 5-10.

Boujibar, A., Bolfan-Casanova, N., Andrault, D., Bouhifd, M.A. and Trcera, N. (2016) Incorporation of Fe^{2+} and Fe^{3+} in bridgmanite during magma ocean crystallization. American Mineralogist 101, 1560-1570.

Fei, H.Z., Liu, Z.D., McCammon, C. and Katsura, T. (2020) Oxygen Vacancy Substitution Linked to Ferric Iron in Bridgmanite at 27 GPa. Geophysical Research Letters 47.

Fei, Y., Virgo, D., Mysen, B., Wang, Y. and Mao, H. (1994) Temperature-dependent electron delocalization in (Mg, Fe)SiO_3 perovskite. American Mineralogist 79, 826-837.

Frost, D.J. and Langenhorst, F. (2002) The effect of Al_2O_3 on Fe–Mg partitioning between magnesiowüstite and magnesium silicate perovskite. Earth and Planetary Science Letters 199, 227-241.

Frost, D.J., Liebske, C., Langenhorst, F., McCammon, C.A., Trønnes, R.G. and Rubie, D.C. (2004) Experimental evidence for the existence of iron-rich metal in the Earth's lower mantle. Nature 428, 409-412.

Grüninger, H., Liu, Z., Siegel, R., Boffa Ballaran, T., Katsura, T., Senker, J. and Frost, D.J. (2019) Oxygen vacancy ordering in aluminous bridgmanite in the Earth's lower mantle. Geophysical Research Letters 46, 8731-8740.

Hummer, D.R. and Fei, Y. (2012) Synthesis and crystal chemistry of Fe^{3+}-bearing (Mg,Fe^{3+})(Si,Fe^{3+})O_3 perovskite. American Mineralogist 97, 1915-1921.

Irifune, T., Shinmei, T., McCammon, C.A., Miyajima, N., Rubie, D.C. and Frost, D.J. (2010) Iron partitioning and density changes of pyrolite in Earth's lower mantle. Science 327, 193-195.

Jackson, J.M., Sturhahn, W., Shen, G., Zhao, J., Hu, M.Y., Errandonea, D., Bass, J.D. and Fei, Y. (2005) A synchrotron Mössbauer spectroscopy study of (Mg,Fe)SiO_3 perovskite up to 120 GPa. American Mineralogist 90, 199-205.

Kojitani, H., Katsura, T. and Akaogi, M. (2007) Aluminum substitution mechanisms in perovskite-type $MgSiO_3$: an investigation by Rietveld analysis. Physics and Chemistry of Minerals 34, 257-267.

Kupenko, I., McCammon, C.A., Sinmyo, R., Cerantola, V., Potapkin, V., Chumakov, A., Kantor, A., Rüffer, R. and Dubrovinsky, L. (2015) Oxidation state of the lower mantle: In situ observations of the iron electronic configuration in bridgmanite at extreme conditions. Earth and Planetary Science Letters 423, 78-86.

Kupenko, I., McCammon, C.A., Sinmyo, R., Prescher, C., Chumakov, A., Kantor, A., Rüffer, R. and Dubrovinsky, L. (2014) Electronic spin state of Fe, Al-containing $MgSiO_3$ perovskite at lower mantle conditions. Lithos 189, 167-172.

Lauterbach, S., McCammon, C., Van Aken, P., Langenhorst, F. and Seifert, F. (2000) Mössbauer and ELNES spectroscopy of (Mg,Fe)(Si,Al)O_3 perovskite: a highly oxidised component of the lower mantle. Contributions to Mineralogy and Petrology 138, 17-26.

Li, J., Sturhahn, W., Jackson, J., Struzhkin, V., Lin, J., Zhao, J., Mao, H. and Shen, G. (2006) Pressure effect on the electronic structure of iron in (Mg,Fe)(Si,Al)O_3 perovskite: a combined synchrotron Mössbauer and X-ray emission spectroscopy study up to 100 GPa. Physics and Chemistry of Minerals 33, 575-585.

Liu, Z., Akaogi, M. and Katsura, T. (2019a) Increase of the oxygen vacancy component in bridgmanite with temperature. Earth and Planetary Science Letters 505, 141-151.

Liu, Z., Ballaran, T.B., Huang, R., Frost, D.J. and Katsura, T. (2019b) Strong correlation of oxygen vacancies in bridgmanite with Mg/Si ratio. Earth and Planetary Science Letters 523, 115697.

Liu, Z., Ishii, T. and Katsura, T. (2017) Rapid decrease of $MgAlO_{2.5}$ component in bridgmanite with pressure. Geochemical Perspectives Letters, 12-18.

McCammon, C.A. (1997) Perovskite as a possible sink for ferric iron in the lower mantle. Nature 387, 694-696.

McCammon, C.A. (1998) The crystal chemistry of ferric iron in $Fe_{0.05}Mg_{0.95}SiO_3$ perovskite as determined by Mössbauer spectroscopy in the temperature range 80–293 K. Physics and Chemistry of Minerals 25, 292-300.

McCammon, C.A., Lauterbach, S., Seifert, F., Langenhorst, F. and Van Aken, P. (2004) Iron oxidation state in lower mantle mineral assemblages: I. Empirical relations derived from high-pressure experiments. Earth and Planetary Science Letters 222, 435-449.

McCammon, C.A., Rubie, D., Ross, C., Seifert, F. and O'Neill, H.S.C. (1992) Mössbauer spectra of $^{57}Fe_{0.05}Mg_{0.95}SiO_3$ perovskite at 80 and 298 K. American Mineralogist 77, 894-897.

Nakajima, Y., Frost, D.J. and Rubie, D.C. (2012) Ferrous iron partitioning between magnesium silicate perovskite and ferropericlase and the composition of perovskite in the Earth's lower mantle. Journal of Geophysical Research: Solid Earth 117, B08201.

Narygina, O.V., Kantor, I.Y., McCammon, C.A. and Dubrovinsky, L. (2010) Electronic state of Fe^{2+} in $(Mg,Fe)(Si,Al)O_3$ perovskite and $(Mg,Fe)SiO_3$ majorite at pressures up to 81 GPa and temperatures up to 800 K. Physics and Chemistry of Minerals 37, 407-415.

Navrotsky, A., Schoenitz, M., Kojitani, H., Xu, H., Zhang, J., Weidner, D.J. and Jeanloz, R. (2003) Aluminum in magnesium silicate perovskite: Formation, structure, and energetics of magnesium-rich defect solid solutions. Journal of Geophysical Research: Solid Earth 108, 2330.

Piet, H., Badro, J., Nabiei, F., Dennenwaldt, T., Shim, S.-H., Cantoni, M., Hébert, C. and Gillet, P. (2016) Spin and valence dependence of iron partitioning in Earth’s deep mantle. Proceedings of the National Academy of Sciences 113, 11127-11130.

Prescher, C., Langenhorst, F., Dubrovinsky, L.S., Prakapenka, V.B. and Miyajima, N. (2014) The effect of Fe spin crossovers on its partitioning behavior and oxidation state in a pyrolitic Earth's lower mantle system. Earth and Planetary Science Letters 399, 86-91.

Shim, S.-H., Grocholski, B., Ye, Y., Alp, E.E., Xu, S., Morgan, D., Meng, Y. and Prakapenka, V.B. (2017) Stability of ferrous-iron-rich bridgmanite under reducing midmantle conditions. Proceedings of the National Academy of Sciences 114, 6468-6473.

Stagno, V., Tange, Y., Miyajima, N., McCammon, C., Irifune, T. and Frost, D. (2011) The stability of magnesite in the transition zone and the lower mantle as function of oxygen fugacity. Geophysical Research Letters 38, L19309.

Appendix A: **The composition and redox state of bridgmanite in the lower mantle as a function of oxygen fugacity**

Rong Huang[a,*], Tiziana Boffa Ballaran[a], Catherine McCammon[a], Nobuyoshi Miyajima[a], David Dolejš[b], Daniel J. Frost[a]

[a] Bayerisches Geoinstitut, Universität Bayreuth, D-95440 Bayreuth, Germany

[b] Institut für Geo- und Umweltnaturwissenschaften, Universität Freiburg, D-79104 Freiburg i.Br., Germany

A.1 Speciation of carbon at different oxygen fugacities

Fig. A.2 summarizes $Fe^{3+}/\Sigma Fe$ ratios measured for Brg as a function of the fO_2 of the synthesis experiments (Table 2). As discussed in section 3.5 the Brg $Fe^{3+}/\Sigma Fe$ ratios vary at a fixed fO_2 due to the different amounts of Al or bulk Fe present in the samples. As mentioned in section 3.1 small amounts of carbon appear to have also been present in some of the experiments as a contaminant (Table 2). As the oxygen fugacities are well constrained in the experiments, information on the speciation of carbon as a function of fO_2 can be obtained and, in particular, limits can be placed on the extent of the $MgCO_3$ stability field with respect to fO_2. As indicated in Table 2 and shown in Fig. A.2, at oxygen fugacities of ≤ IW, carbon is observed to be present in the experiments as carbide or diamond. At oxygen fugacities > IW + 2.7 (monitored by Ir as the sliding redox sensor), however, carbon is present as $(Mg,Fe)CO_3$ carbonate. This means that the equilibrium:

$$\underset{\text{Magnesite}}{(\mathrm{Mg,Fe})\mathrm{CO_3}} = \underset{\text{Fp}}{(\mathrm{Mg,Fe})\mathrm{O}} + \underset{\text{diamond}}{\mathrm{C}} + \mathrm{O_2} \qquad (\mathrm{A.1})$$

is bracketed by the experiments between oxygen fugacity of IW and IW + 2.7. Stagno et al. (2011) determined the fO_2 of this equilibrium at approximately 25 GPa between 1773–1973 K to be at IW + 2.46, as shown in Fig. A.2, which is in very good agreement with the current results. Using the Holland and Powell (2011) data base, the calculated fO_2 for this equilibrium is IW + 4.0, which is significantly higher than both experimental determinations. This may arise from uncertainties in the equation of state of $MgCO_3$ and likely means that the derivative of the bulk modulus with respect to pressure, *K'*, is less than the value of 4 proposed in the database.

A.2 Activity coefficients of Brg components in Al-Mg-Si-O system

Binary symmetric models describing the non-ideality of mixing:

$$\mathrm{R}T\ln\gamma^{\mathrm{Brg}}_{\mathrm{MgSiO_3}} = W^{\mathrm{Brg}}_{\mathrm{MgAl,A}}\left(1-x_{\mathrm{Mg,A}}\right)^2 + W^{\mathrm{Brg}}_{\mathrm{AlSi,B}}\left(1-x_{\mathrm{Si,B}}\right)^2 + W^{\mathrm{Brg}}_{\mathrm{OV,O1}}\left(1-x_{\mathrm{O,O1}}\right)^2 \qquad (\mathrm{A.2})$$

$$\mathrm{R}T\ln\gamma^{\mathrm{Brg}}_{\mathrm{AlAlO_3}} = W^{\mathrm{Brg}}_{\mathrm{MgAl,A}}\left(1-x_{\mathrm{Al,A}}\right)^2 + W^{\mathrm{Brg}}_{\mathrm{AlSi,B}}\left(1-x_{\mathrm{Al,B}}\right)^2 + W^{\mathrm{Brg}}_{\mathrm{OV,O1}}\left(1-x_{\mathrm{O,O1}}\right)^2 \qquad (\mathrm{A.3})$$

Combined expression for equation (16):

$$\Delta G^{0}_{(15)} = -\mathrm{R}T\ln\frac{\left(x^{\mathrm{Brg}}_{\mathrm{AlAlO_3}}\right)^{1/16}\left(x^{\mathrm{Brg}}_{\mathrm{MgSiO_3}}\right)^{7/8}}{x^{\mathrm{Brg}}_{\mathrm{MgSi_{7/8}Al_{1/8}O_{15/16}O_2}}} - 1/16[W^{\mathrm{Brg}}_{\mathrm{MgAl,A}}\left(1-x_{\mathrm{Al,A}}\right)^2 + W^{\mathrm{Brg}}_{\mathrm{AlSi,B}}\left(1-x_{\mathrm{Al,B}}\right)^2 + W^{\mathrm{Brg}}_{\mathrm{OV,O1}}\left(1-x_{\mathrm{O,O1}}\right)^2] - 7/8[W^{\mathrm{Brg}}_{\mathrm{MgAl,A}}\left(1-x_{\mathrm{Mg,A}}\right)^2 + W^{\mathrm{Brg}}_{\mathrm{AlSi,B}}\left(1-x_{\mathrm{Si,B}}\right)^2 + W^{\mathrm{Brg}}_{\mathrm{OV,O1}}\left(1-x_{\mathrm{O,O1}}\right)^2] + W^{\mathrm{Brg}}_{\mathrm{MgAl,A}}\left(1-x_{\mathrm{Mg,A}}\right)^2 + W^{\mathrm{Brg}}_{\mathrm{AlSi,B}}\left(1-x_{\mathrm{Al,B}}\right)^2 + W^{\mathrm{Brg}}_{\mathrm{OV,O1}}\left(1-x_{\mathrm{V,O1}}\right)^2 \quad (\mathrm{A}.4)$$

A.3 Activity coefficients of Brg components in Fe-Mg-Si-O system

Ternary symmetric models used to describe the activity coefficients of Brg components in the Fe-Mg-Si-O system:

$$\mathrm{R}T\ln\gamma^{\mathrm{Brg}}_{\mathrm{MgSiO_3}} = W^{\mathrm{Brg}}_{\mathrm{MgFe^{3+},A}}\left(1-x_{\mathrm{Mg,A}}\right)^2 + W^{\mathrm{Brg}}_{\mathrm{Fe^{3+}Si,B}}\left(1-x_{\mathrm{Si,B}}\right)^2 + W^{\mathrm{Brg}}_{\mathrm{OV,O1}}\left(1-x_{\mathrm{O,O1}}\right)^2 \quad (\mathrm{A}.5)$$

$$\mathrm{R}T\ln\gamma^{\mathrm{Brg}}_{\mathrm{FeFeO_3}} = \left(x_{\mathrm{Mg,A}}\right)^2 W^{\mathrm{Brg}}_{\mathrm{MgFe^{3+},A}} + \left(x_{\mathrm{Fe^{2+},A}}\right)^2 W^{\mathrm{Brg}}_{\mathrm{Fe^{2+}Fe^{3+},A}} + x_{\mathrm{Mg,A}}x_{\mathrm{Fe^{2+},A}}\left(W^{\mathrm{Brg}}_{\mathrm{MgFe^{3+},A}} + W^{\mathrm{Brg}}_{\mathrm{Fe^{2+}Fe^{3+},A}} - W^{\mathrm{Brg}}_{\mathrm{MgFe^{2+},A}}\right) + x_{\mathrm{Mg,A}}x_{\mathrm{Fe^{2+},A}}\left(1-2x_{\mathrm{Fe^{3+},A}}\right)\left(W^{\mathrm{Brg}}_{\mathrm{MgFe^{3+},A}} + W^{\mathrm{Brg}}_{\mathrm{Fe^{2+}Fe^{3+},A}} + W^{\mathrm{Brg}}_{\mathrm{MgFe^{2+},A}}\right) + W^{\mathrm{Brg}}_{\mathrm{Fe^{3+}Si,B}}\left(1-x_{\mathrm{Fe^{3+},B}}\right)^2 + W^{\mathrm{Brg}}_{\mathrm{OV,O1}}\left(1-x_{\mathrm{O,O1}}\right)^2 \quad (\mathrm{A}.6)$$

$$\mathrm{R}T\ln\gamma^{\mathrm{Brg}}_{\mathrm{MgSi_{7/8}Fe_{1/8}V_{1/8}O_{7/8}O_2}} = W^{\mathrm{Brg}}_{\mathrm{MgFe^{3+},A}}\left(1-x_{\mathrm{Mg,A}}\right)^2 + W^{\mathrm{Brg}}_{\mathrm{Fe^{3+}Si,B}}\left(1-x_{\mathrm{Fe^{3+},B}}\right)^2 + W^{\mathrm{Brg}}_{\mathrm{OV,O1}}\left(1-x_{\mathrm{V,O1}}\right)^2 \quad (\mathrm{A}.7)$$

$$\mathrm{R}T\ln\gamma^{\mathrm{Fp}}_{\mathrm{MgO}} = \left(1-x^{\mathrm{Fp}}_{\mathrm{Mg}}\right)^2 \times W^{\mathrm{Fp}}_{\mathrm{MgFe^{2+}}} \quad (\mathrm{A}.8)$$

where $W^{\mathrm{Brg}}_{\mathrm{MgFe^{3+},A}}$, $W^{\mathrm{Brg}}_{\mathrm{MgFe^{2+},A}}$, $W^{\mathrm{Brg}}_{\mathrm{Fe^{2+}Fe^{3+},A}}$, and $W^{\mathrm{Brg}}_{\mathrm{Fe^{3+}Si,B}}$ are Margules interaction parameters that describe non-ideal mixing between Mg^{2+}-Fe^{3+}, Mg^{2+}-Fe^{2+} and Fe^{2+}-Fe^{3+}on the A site, Si^{4+}-Fe^{3+} on the B site and the O-vacancy on the O1 site in Brg. $W^{\mathrm{Fp}}_{\mathrm{MgFe^{2+}}} = 14\ \mathrm{kJ/mol}$ taken from Frost (2003) describes the interaction energy between Mg^{2+}-Fe^{2+} in Fp. By using these symmetric interaction parameters, equation (21) becomes:

$$\Delta G^{0}_{(20)} = -\mathrm{R}T\ln\frac{\left(x^{\mathrm{Brg}}_{\mathrm{FeFeO_3}}\right)^{1/16}\left(x^{\mathrm{Brg}}_{\mathrm{MgSiO_3}}\right)^{7/8}\left(x^{\mathrm{Fp}}_{\mathrm{MgO}}\right)^{1/8}}{x^{\mathrm{Brg}}_{\mathrm{MgSi_{7/8}Fe_{1/8}O_{15/16}O_2}}}$$
$$-\frac{1}{16}\Big[\left(x_{\mathrm{Mg,A}}\right)^2 W^{\mathrm{Brg}}_{\mathrm{MgFe^{3+},A}} + \left(x_{\mathrm{Fe^{2+},A}}\right)^2 W^{\mathrm{Brg}}_{\mathrm{Fe^{2+}Fe^{3+},A}}$$
$$+ x_{\mathrm{Mg,A}}x_{\mathrm{Fe^{2+},A}}\left(W^{\mathrm{Brg}}_{\mathrm{MgFe^{3+},A}} + W^{\mathrm{Brg}}_{\mathrm{Fe^{2+}Fe^{3+},A}} - W^{\mathrm{Brg}}_{\mathrm{MgFe^{2+},A}}\right)$$
$$+ x_{\mathrm{Mg,A}}x_{\mathrm{Fe^{2+},A}}\left(1-2x_{\mathrm{Fe^{3+},A}}\right)\left(W^{\mathrm{Brg}}_{\mathrm{MgFe^{3+},A}} + W^{\mathrm{Brg}}_{\mathrm{Fe^{2+}Fe^{3+},A}} + W^{\mathrm{Brg}}_{\mathrm{MgFe^{2+},A}}\right)$$
$$+ W^{\mathrm{Brg}}_{\mathrm{Fe^{3+}Si,B}}\left(1-x_{\mathrm{Fe^{3+},B}}\right)^2 + W^{\mathrm{Brg}}_{\mathrm{OV,O1}}\left(1-x_{\mathrm{O,O1}}\right)^2\Big]$$
$$-\frac{7}{8}\Big[W^{\mathrm{Brg}}_{\mathrm{MgFe^{2+},A}}\left(1-x_{\mathrm{Mg,A}}\right)^2 + W^{\mathrm{Brg}}_{\mathrm{Fe^{3+}Si,B}}\left(1-x_{\mathrm{Si,B}}\right)^2 + W^{\mathrm{Brg}}_{\mathrm{OV,O1}}\left(1-x_{\mathrm{O,O1}}\right)^2\Big]$$
$$-\frac{1}{8}\Big[\left(1-x^{\mathrm{Fp}}_{\mathrm{Mg}}\right)^2 \times W^{\mathrm{Fp}}_{\mathrm{MgFe^{2+}}}\Big] + W^{\mathrm{Brg}}_{\mathrm{MgFe^{3+},A}}\left(1-x_{\mathrm{Mg,A}}\right)^2 + W^{\mathrm{Brg}}_{\mathrm{Fe^{3+}Si,B}}\left(1-x_{\mathrm{Fe^{3+},B}}\right)^2$$
$$+ W^{\mathrm{Brg}}_{\mathrm{OV,O1}}\left(1-x_{\mathrm{V,O1}}\right)^2 \qquad (\mathrm{A.9})$$

A.4 Estimation of bulk modulus of different Brg endmembers

The bulk modulus of $MgSiO_3$ Brg is taken from the study of Boffa Ballaran et al. (2012). The bulk moduli of the $FeAlO_3$, $AlAlO_3$, $MgAlO_{2.5}$ and $FeFeO_3$ Brg endmembers were estimated from the results of studies (Boffa Ballaran et al., 2012; Brodholt, 2000; Catalli et al., 2010) that determined bulk moduli of Brg containing significant proportions of these substitutions, according to the equation:

$$K = \frac{V}{\sum_{i=1}^{N}\frac{x_i V_i}{K_i}} \qquad (\mathrm{A.10})$$

where x_i is the mole fraction of component i in the solid solution, K_i and V_i are the bulk modulus and molar volume of pure i, K and V are the bulk modulus and volume of the solid solution. Bulk moduli results from Brodholt (2000) were normalized with a factor that allowed the value for $MgSiO_3$ Brg reported in the same study to be brought into agreement with the value reported by Boffa Ballaran et al. (2012). This accounts for the underestimation of the bulk modulus encountered in generalized gradient approximation (GGA) calculations. The bulk modulus of $MgFeO_{2.5}$ was assumed to be the same as $MgAlO_{2.5}$. The molar volumes of different endmembers (V_i) are taken from Huang (2020) (Table B.5) and the bulk moduli obtained for the different Brg components are reported in Table B.5.

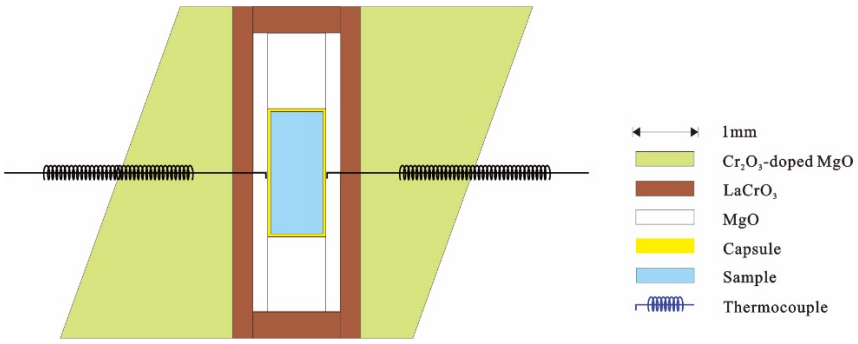

Fig. A.1 Schematic cross-section of the 7/3 pressure assembly used in the multi-anvil experiments.

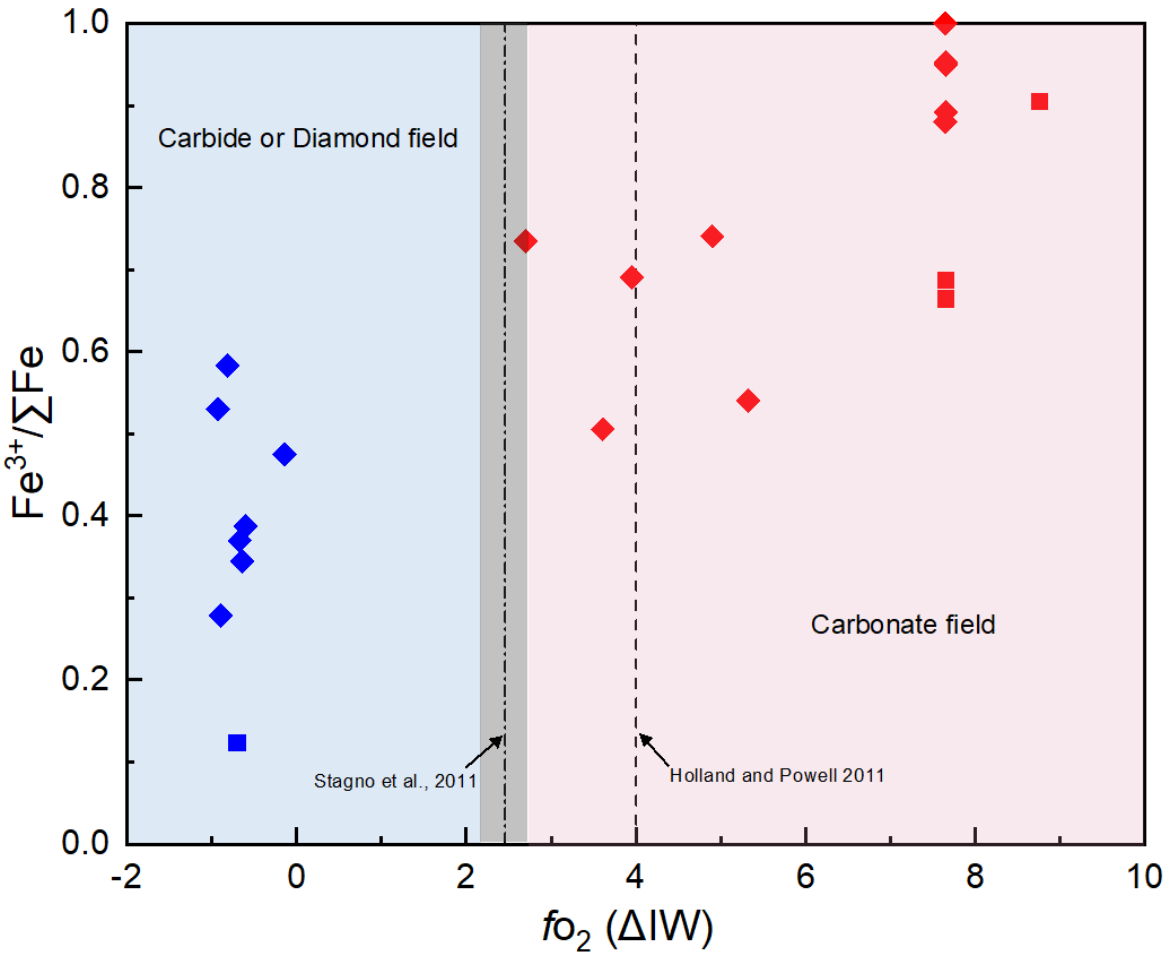

Fig. A.2 The Brg $Fe^{3+}/\Sigma Fe$ ratios obtained in this study are shown as a function of oxygen fugacity. The blue and red symbols indicate experiments where carbon existed as carbide/diamond or carbonate, respectively. The diamonds indicate Al-bearing samples and squares indicate Al-free samples. The dash-dotted line shows the oxygen fugacity at which diamond and carbonate coexist as determined by Stagno et al. (2011) at 25 GPa and 1773-1973 K and the grey shaded area shows the uncertainty. The dashed line shows the fo_2 of the same equilibrium determined with the database of Holland and Powell (2011).

Boffa Ballaran T., Kurnosov, A., Glazyrin, K., Frost, D.J., Merlini, M., Hanfland, M. and Caracas, R. (2012) Effect of chemistry on the compressibility of silicate perovskite in the lower mantle. *Earth Planet. Sci. Lett.* **333-334**, 181-190.

Brodholt J.P. (2000) Pressure-induced changes in the compression mechanism of aluminous perovskite in the Earth's mantle. *Nature* **407**, 620-622.

Catalli K., Shim, S.-H., Prakapenka, V.B., Zhao, J., Sturhahn, W., Chow, P., Xiao, Y., Liu, H., Cynn, H. and Evans, W.J. (2010) Spin state of ferric iron in $MgSiO_3$ perovskite and its effect on elastic properties. *Earth Planet. Sci. Lett.* **289**, 68-75.

Frost D.J. (2003) Fe^{2+}-Mg partitioning between garnet, magnesiowüstite, and $(Mg,Fe)_2SiO_4$ phases of the transition zone. *Am. Mineral.* **88**, 387-397.

Holland T.J.B. and Powell, R. (2011) An improved and extended internally consistent thermodynamic dataset for phases of petrological interest, involving a new equation of state for solids. *J. Metamorph. Geol.* **29**, 333-383.

Huang R. (2020) Bridgmanite crystal chemistry and iron content in the Earth's lower mantle. Ph. D. thesis, Universität Bayreuth, https://epub.uni-bayreuth.de/4611/.

Stagno V., Tange, Y., Miyajima, N., McCammon, C., Irifune, T. and Frost, D. (2011) The stability of magnesite in the transition zone and the lower mantle as function of oxygen fugacity. *Geophys. Res. Lett.* **38**, L19309.